UNIVERSITY OF CAMBRIDGE

CAVENDISH LABORATORY

$FeSb_2$: a riddle, inside an insulator, wrapped in a metal

Electric and magnetic properties of the unconventional insulator iron diantimonide

ALEXANDER GEOFFREY EATON

ST CATHARINE'S COLLEGE

SUBMITTED SEPTEMBER 2022

This dissertation is submitted for the degree of Doctor of Philosophy

Declaration

This dissertation is the result of my own work and includes nothing that is the outcome of work done in collaboration except as declared in the preface and specified in the text. It is not substantially the same as any work that has already been submitted before for any degree or other qualification except as declared in the preface and specified in the text. This dissertation does not exceed the word limit of 60,000 prescribed by the Degree Committee for the Faculty of Physics and Chemistry.

The research projects described in this thesis were undertaken with the supervision of S. E. Sebastian. Several of the research projects presented in this thesis were the work of collaboration. All measurements on $FeSb_2$ samples presented in this thesis were performed on samples grown by K.-J. Xu of the Shen group, Stanford University. All measurements on SmB_6 samples presented in this thesis were performed on samples grown by M. Ciomaga Hatnean of the Balakrishnan group, University of Warwick. Heat capacity measurements were performed in collaboration with S. Yamashita of Osaka University. Energy dispersive x-ray diffraction was performed in collaboration with S. M. Fairclough of the Department of Materials Science, University of Cambridge. Raman spectroscopy was performed in collaboration with R. T. Phillips, Cavendish Laboratory, University of Cambridge. Extraction magnetometry was performed in collaboration with A. Miyake, Institute of Solid State Physics, University of Tokyo. Metamagnetic modelling was performed in collaboration with colleagues G. G. Lonzarich and G. F. L. Rodway-Gant. Band structure and DFT+U calculations were performed by M. D. Johannes of the Naval Research Laboratory, Washington, D.C., USA.

Sample preparation and characterisation was performed by myself and H. Liu, with some additional assistance from A. J. Hickey. All data presented in this thesis in applied magnetic fields of strengths $\leq$ 14 T were taken by myself in Cambridge. All data presented in this thesis at magnetic field strengths $>$ 14 T were collected at high magnetic field facilities, as part of a group endeavour. Experiments at high magnetic field facilities,

for which the data are presented in this thesis, were led primarily by myself, with technical assistance provided by the local user support staff. Analysis on the high-field data presented in this thesis was performed primarily by myself, with some performed jointly with H. Liu, and some with additional assistance from A. J. Hickey and N.J.M. Popiel. Data in applied fields ≤ 14 T were analysed by myself, with some assistance from N. J. M. Popiel. In several places, where applicable, these contributions are also acknowledged in the text.

A manuscript detailing the discovery of insulating quantum oscillations in $FeSb_2$, for which the results are presented in chapter 5, is currently undergoing peer review. The measurements indicative of the formation of a metallic surface state on $FeSb_2$, which are presented in chapter 6, are currently being prepared into manuscript form. At time of writing, the exotic *I-V* characteristics of $FeSb_2$ discussed in chapter 7 are still the subject of ongoing investigation.

A number of figures presented in this thesis have been made with valuable input from colleagues H. Liu (Figs. 4.1, 4.3, 5.3, 5.13, 5.14, & 5.15), A. J. Hickey (4.1, 4.3, 5.13, 7.3, & 7.8), N. J. M. Popiel (Figs. 5.7, 5.8, 6.4, 7.7, A.6, & A.7), and G. L. F. Rodway-Gant (5.17).

A. G. Eaton

September 2022

Acknowledgements

There is a large number of people to whom I am profusely grateful and appreciative for their help, advice, and support over the past four years. Firstly, I would like to thank Suchitra Sebastian, for affording me this fantastic opportunity. The work of this thesis would not have been possible without the support of other members of the QM group, and in particular my peers in Sebastian group. My deepest gratitude extends to: Alex Hickey, for astute realism at all times; to Indy Liu, for perpetual chirpiness (even at 4am); to Nicholas Popiel, for endless theoretical pondering and good vibes; to Máté Hartstein, for showing me the ropes (and the hops); to Sofia Taylor-Coronel, for always being so lovely; to Alex Davies, for teaching me many valuable lessons (on chemistry and life); and to Patricia Lebre Alireza, for showing me what magnet time was *really* like.

Special thanks to Matt, Gilles, Tony, Jess, Michael, Kalai, Cheng, Jiasheng, Malte, Siân, Montu, Gil, Christian, Oliver, Theo, Max, Nicola, Liam, Keiron, Jordan, David, and all our summer students for being there throughout various periods of this journey. Thank you Mijaíl, for accompanying me through the final stages of this adventure, and helping prepare me for what lies beyond. I am especially grateful to Alix McCollam, in Nijmegen, and Dave Graf, in Tallahassee, for their expertise, guidance, and kindness during challenging magnet times. I am indebted to EPSRC and St Catharine's College for their generous financial support.

Finally, I would like to thank my parents – both for setting me on this journey, and then encouraging me all the way.

Abstract

The distinction between metals and insulators forms a fundamental tenet of condensed matter physics. Over the past decade or so, the explosion of interest in topological insulators – materials that host a metallic surface state atop their insulating bulks – has demonstrated how the contrasting properties of insulators and metals can be synergistically combined. In contrast, recent observations of Fermi surface signatures – conventionally presumed to be characteristic of a (metallic) Fermi liquid – from within a new class of unconventional insulators has profoundly called into question our conventional understanding of this fundamental tenet.

This dissertation focusses on experimental studies of the strongly correlated insulator iron diantimonide ($FeSb_2$). It is found that $FeSb_2$ exhibits anomalous behaviour in both its magnetic and electrical properties. Under the application of high magnetic fields, quantum oscillations in the magnetisation are observed, with an inverse-field periodicity indicating the presence of Landau quantisation. Remarkably, these are shown to emanate from the insulating bulk of the material – in sharp contrast to our conventional interpretation of Landau's Fermi liquid model.

These findings are discussed in the context of previously discovered unconventional insulators. Notably, unlike other unconventional insulators reported to date, the unconventional quantum oscillatory profile in $FeSb_2$ is found to be closely related to changes in the bulk magnetisation of the material. At low fields, a marked enhancement in the growth of the magnetic torque signal is accompanied by a likewise enhancement in both the quantum oscillatory amplitude and frequency. Then, at the highest fields, a sharp

metamagnetic transition abruptly quenches the insulating quantum oscillations – in marked contrast to numerous tunnelling and magnetic-breakdown posited models of unconventional insulating behaviour. These findings point strongly to a magnetic origin being responsible for the manifestation of this paradoxical phenomenon.

Additionally, a suite of electrical transport measurements is presented, demonstrating the presence of surface-dominated conduction at low temperatures, corroborating previous reports from angle resolved photoemission spectroscopy studies. Notable comparisons with the putative topological Kondo insulator samarium hexaboride (SmB_6) are discussed, including signatures of non-Ohmic electrical transport. Evidence indicative of metallic surface states on SmB_6 has been reported from multiple sources. Several of these measurements are repeated here on $FeSb_2$, and excellent correspondence between the features of both materials is observed. Therefore, the mechanism driving surface-dominated conduction in $FeSb_2$ is very likely to be the same as that in SmB_6.

Contents

1

Introduction

> *"Begin at the beginning," the King said, gravely, "and go on till you come to an end; then stop."*
>
> – Lewis Carroll, *Alice in Wonderland*

Throughout the history of science, exploration-based research has led to numerous experimental breakthroughs, from the discovery of penicillin by Alexander Fleming [1] to Rutherford's stunning demonstration of the nuclear character of atoms [2]. Within the field of condensed matter physics, the development of an intimate synergy between rare bursts of discovery-driven advancements, in combination with subsequent theory-led incremental experimental progress, has proven invaluable in furthering our understanding of solid state systems. For example, the discovery of high-T_c superconductors [3] falls squarely in the first category, with the theoretical prediction [4–6] and subsequent experimental realisation [7, 8] of topological quantum matter being an archetypical example of the latter.

Performing exploration-led research is challenging. While the potential reward of discovery is high, the likelihood of failure is likewise. Thus, to probe most effectively into the unknown, one should seek firm initial guidance of which avenues may be the most

fruitful to investigate.

Turning to the context of quantum matter, the overarching success of the band theory of solids constitutes one of the finest achievements in 20^{th} century science. Based on a periodic plane wave premise [9], band theory successfully describes a myriad of physical properties one encounters in everyday life – from why silver is shiny to why glass is transparent. However, there are a number of materials classes wherein this celebrated theory fails to accurately capture the majority of behaviour observed, owing to the presence of strong electron-electron correlation effects giving rise to emergent new phenomena beyond the simple band picture. It is within these such systems that exploratory research endeavours have proved extremely productive over recent decades – often through exposing such materials to extreme physical conditions.

Across experimental physics, the ability to raise the energy frontier to new technological heights has often proved invaluable in effecting novel advancements. Examples from high energy physics include searching for theoretically postulated phenomena, such as the Higgs boson [10–12], along with other purely serendipitous findings: take for example the discovery of the kaon [13], which indicated the existence of a new, 'strange' quark. In condensed matter physics, the attainment of ultra low temperatures and intense magnetic fields likewise enhances the ability of the experimentalist to explore new ground, by pushing materials into extreme conditions beyond those previously investigated. It is these such studies – to low temperatures < 2 K and high magnetic fields up to 70 T – that form the focus of this dissertation.

1.1 When is an insulator not an insulator?

The distinction between metals and insulators constitutes one of the fundamental tenets of condensed matter physics. When electrons are subjected to a periodic potential – such as in a crystalline solid – gaps form in their dispersion relation, at each Brillouin zone boundary. The allowed electronic energy states thereby coalesce into bands, with forbid-

den gaps separating each band of allowed energy levels from the next. If we were to consider a given material in the $T \rightarrow 0$ K limit, then the identification of the highest occupied energy level (termed the Fermi energy, E_{F}) instantly identifies the material as being either metallic or insulating in character.

For the case of E_{F} lying within a band, then a small amount of energy is easily capable of exciting quasiparticles into the nearby energy states just above E_{F}; hence, the material is a metal. This property of metals – namely the accessibility to numerous higher energy states in close proximity to E_{F} – gives rise to their excellent electrical and thermal conductivities. The locus of points (in momentum space) at E_{F} (i.e. separating the filled from unfilled states) is defined as the Fermi surface [14, 15].

Conversely, for the case of E_{F} being located between two bands, this implies that a much larger quantity of energy is required to excite a quasiparticle into the next available energy level – hence insulators are very poor conductors, and do not possess a Fermi surface. (In the case of being subjected to a very large electric field – say, during a lightning strike – many insulators actually start to melt before this gap between allowed energy bands is overcome.)

There are some notable cases where strong correlation effects break this model – for example, in the case of the Mott insulator [16, 17]. There are yet others where both metallic and insulating behaviours are exhibited within a single system; for example, topological insulators have an insulating bulk, but an atomically thin metallic surface layer [7]. Even more exotic is the recent observation of magnetic quantum oscillations – a hallmark of metallic behaviour [18] – being hosted within the bulk of electrically insulating phases of matter [19–25].

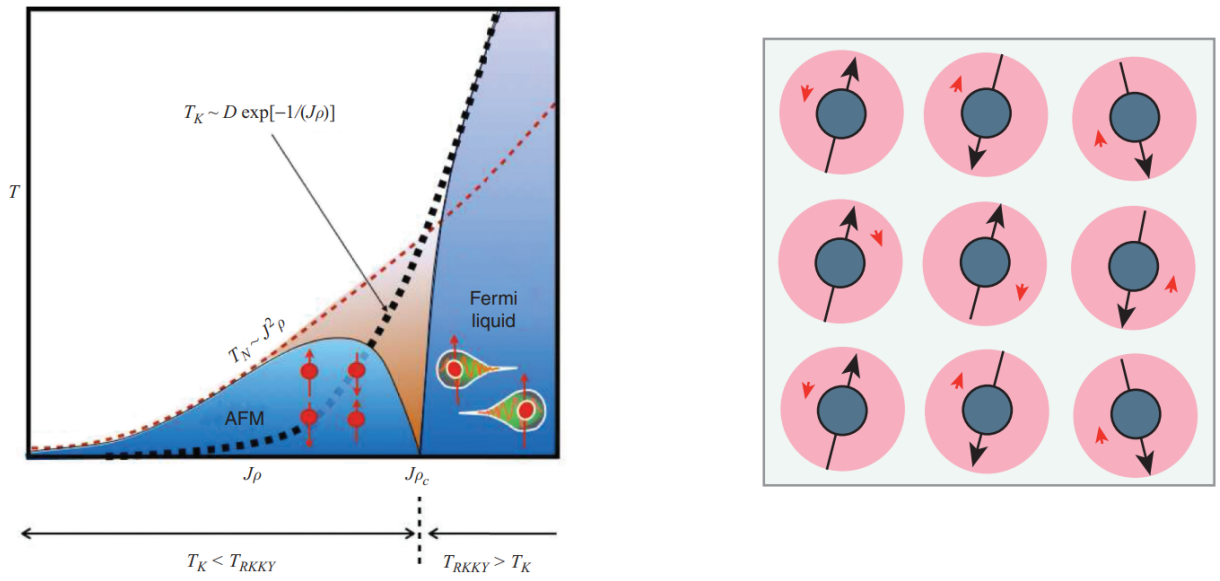

Fig. 1.1. The Kondo effect. *Left:* The Doniach phase diagram for Kondo lattice materials, illustrating the competition between RKKY and Kondo interactions. ρ denotes the conduction electron density of states per spin, and T_N is the Néel temperature. Note that in the case of SmB_6 heavy f-states effectively dope the system, resulting in a strongly correlated insulating ground state, not a Fermi liquid [26]. *Right:* Schematic of the Kondo lattice model. Large randomly oriented localised moments on lattice sites (blue) are screened by clouds of conduction electrons (pink) by Lenz's law. Figure adapted from ref. [26] and reproduced with permission.

1.2 Strong correlations in an insulating state

The Kondo effect

In 1964 Jun Kondo explained the intriguing observation that a non-magnetic metal with a small number of magnetic impurities exhibits a minimum in its resistivity versus temperature profile when cooled to low temperature [27]. This comes about due to the coupling between the spin of conduction electrons, $\boldsymbol{S_e}$, and the spin of the magnetic impurity ions,

$\boldsymbol{S_i}$, which may be expressed formally by the following Hamiltonian:

$$H = J\boldsymbol{S_i} \cdot \boldsymbol{S_e}, \tag{1.1}$$

where the magnitude of J gives the interaction strength between the two spins. The conduction electrons screen $\boldsymbol{S_i}$, leading to the formation of a non-magnetic Kondo singlet. This gives an energy scale that is governed by the density of states at the Fermi energy, $g(E_\mathrm{F})$, and J:

$$k_\mathrm{B}T_\mathrm{F} \sim \frac{1}{g(E_\mathrm{F})} \exp\left(\frac{-1}{Jg(E_\mathrm{F})}\right), \tag{1.2}$$

which allows us to define the Kondo temperature, T_K, as the temperature below which the formation of such singlets is expected [28]. This description is also valid when extended to a Kondo lattice model (where the magnetic ions are no longer just impurities but instead form part of the crystal basis). In this case, in addition to screening the localised moments on the ions, the conduction electrons can also mediate long-range magnetic coupling between two local moments. This can give rise to the Ruderman-Kittel-Kasuya-Yosida (RKKY) interaction [29–31], which for different J competes with the Kondo effect as depicted in Figure 1.1.

From a band theory perspective, the formation of Kondo singlets may be rationalised as the hybridisation between dispersive d-bands with flat f-bands, leading to the opening of a small indirect bandgap, in which E_F lies [32]. To date several Kondo insulators have been discovered, generally incorporating $4f$ elements such as Sm, Yb and Ce [33]. Depending on intricacies of the f-state correlations, Kondo lattice materials can be either metallic or insulating in character.

Samarium hexaboride

The first Kondo insulator to be discovered was samarium hexaboride (SmB_6), which in 1969 was found to exhibit a high electrical conductivity at room temperature that quickly diminished on cooling, yielding an insulating ground state at low temperatures [35]. Be-

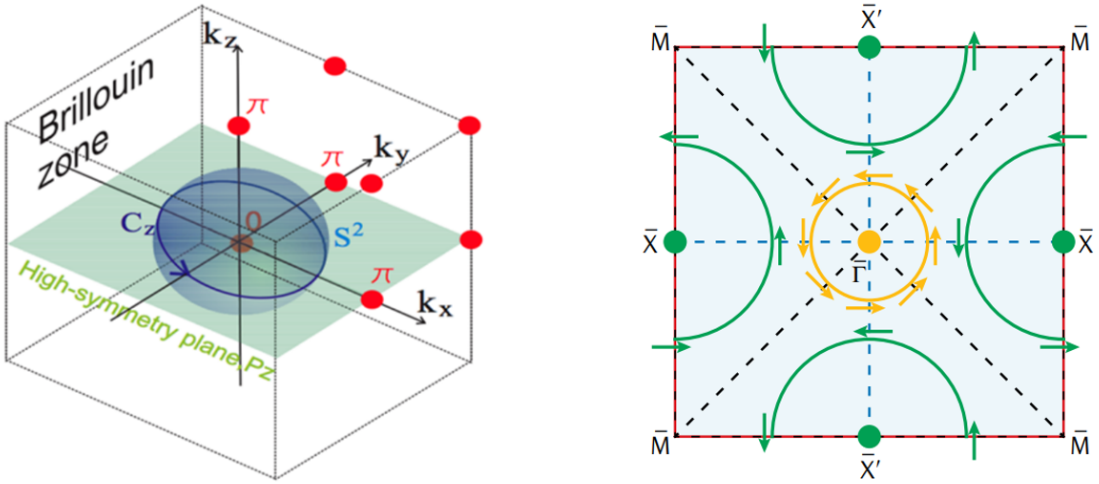

Fig. 1.2. Prediction of SmB_6 as a topological Kondo insulator. *Left:* Brillouin zone of SmB_6. The blue curve depicts the expectation of a nonzero Chern number, C, on the sphere labelled S^2. *Right:* Surface state prediction for the (100) plane. The ochre circle indicates the presence of a surface Dirac point, with arrows indicative of the suggested spin structure. Left panel reproduced with permission from ref. [32]. Copyright (2010) by the American Physical Society. Right panel reproduced from ref. [34] with permission from Springer Nature.

yond the somewhat simplistic Kondo model explicated above, many of the physical properties of SmB_6 emerge due to it possessing a mixed valence character [36]. As all Sm lattice sites are equivalent, two distinct valence states can therefore be mixed together in the ground state and low lying excited states[1]. This gives a $4f$ occupation of ≈ 5.4, and thus a valence of $\approx$ 2.5-2.6 [39]. This picture can be well described by a two-band Hubbard model, explaining the formation of the insulating gap, which closes under small amounts of doping to yield a magnetic metallic state [40].

Early experimental studies of SmB_6 yielded two strange experimental observations that lay unresolved for a number of years – namely, the presence of a low temperature resistance plateau for temperatures $\lessapprox 6$ K, and a finite linear specific heat coefficient in the

[1] Analogous mixed valencies occur in the d-electron analogues FeSi and $FeSb_2$ [37, 38].

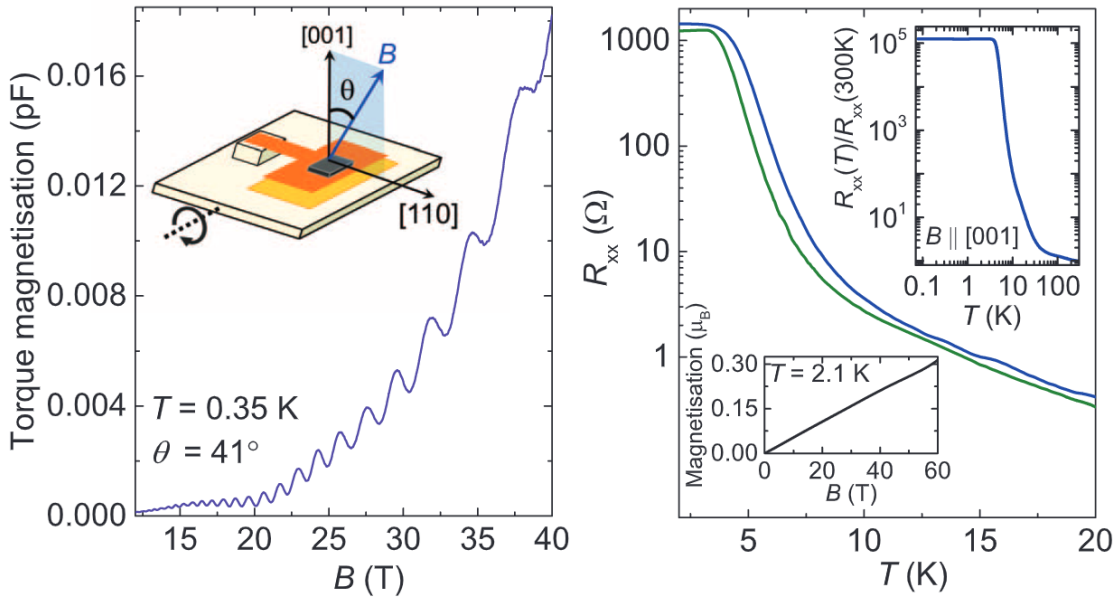

Fig. 1.3. Quantum oscillations observed in the insulating bulk of SmB_6. Quantum oscillations in the magnetic torque (left) of an SmB_6 single crystal mounted on a capacitive torque cantilever (inset). The low temperature electrical resistance of SmB_6 in ambient magnetic field (right, blue curve) is only modestly reduced upon application of a large magnetic field of magnitude 45 T (green curve); hence, the observed oscillations at 0.35 K are anomalously emanating from an insulating phase of matter. Insets show the (normalised) resistivity to 300 K, and the magnetisation to 60 T. Figure adapted from ref. [19] and reproduced with permission of AAAS.

zero temperature limit [41] larger in magnitude than that of its metallic cousin, LaB_6 [42].

The first of these anomalies – the low temperature resistance plateau – was addressed in a 2010 theoretical work that predicted SmB_6 to be a topological Kondo insulator [32]. In this model, a saturating low temperature resistivity can be understood in terms of the presence of a metallic surface state atop an insulating bulk, the formation of which shorts the bulk conduction channel. This thereby leads to a plateauing conductance once the surface state is stabilised at low temperature. A multitude of evidence indicative of the presence of metallic surface states on SmB_6 has since come to light following that original

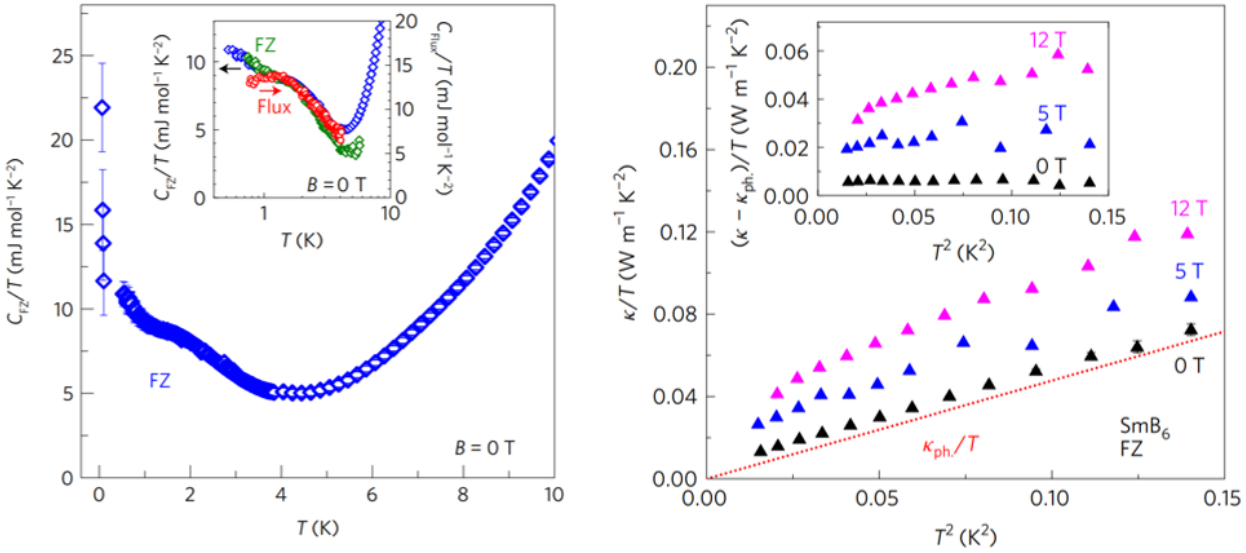

Fig. 1.4. Thermal anomalies in SmB_6. *Left:* Specific heat capacity divided by temperature versus temperature for an SmB_6 single crystal sample grown by the floating zone method. The inset compares specific heat data for floating zone samples (blue and green points) with that for a flux grown sample (red points). *Right:* Thermal conductivity divided by temperature versus temperature squared. A clear enhancement of thermal conductivity is observed for higher magnetic fields. The inset shows the same data with the quadratic in temperature phononic contribution subtracted. Figure adapted from ref. [20] and reproduced with permission of Springer Nature.

theoretical prediction [33, 34]; however, firm evidence of topological protection is yet to be conclusively established.

The question of the second anomaly – the presence of a finite linear specific heat coefficient in the zero temperature limit – has also been revisited in recent years. Figure 1.3 shows magnetic quantum oscillations measured by the torque magnetometry technique on an SmB_6 single crystal reported in ref. [19]. Remarkably, this study resolved quantum oscillatory signatures characteristic of a bulk 3D metallic-like Fermi surface – despite the bulk of SmB_6 being strongly electrically insulating. Comparison between the size of Fermi surface pockets deduced from quantum oscillations, and the residual Sommerfeld coefficient determined from heat capacity measurements (Fig. 1.4) show that the anoma-

lously high low temperature heat capacity of Kondo insulating SmB_6 can be thought of as coming from itinerant fermionic quasiparticles, that couple to magnetic fields but **not** to electrical fields (at least to first order) [20]. We will explore the implications of these findings in greater depth in chapter 3.

1.3 Iron diantimonide

This dissertation examines the intermetallic compound iron diantimonide ($FeSb_2$). We shall find that $FeSb_2$ exhibits several signatures underlining a dichotomy between insulating and metallic behaviours, with electrical measurements indicating the presence of a metallic surface state at low temperatures [43], yet remarkably the bulk of the material yields magnetic signatures indicative of highly mobile fermions – despite being robustly electrically insulating up to very high magnetic fields [44].

$FeSb_2$ is a strongly correlated d-electron insulator [47] that crystallises in the orthorhombic $Pnnm$ crystal structure (No. 58), and exhibits several similarities in common with f-electron Kondo insulators [37]. Evidence of strong electron-electron interactions in this material has been observed in a variety of physical properties, including electrical and thermal transport [48], magnetic susceptibility [49], optical conductivity [50], specific heat [51], and x-ray absorption spectroscopy [38].

At low temperatures $T \approx 10$ K a colossal Seebeck effect in $FeSb_2$ has been reported, of $S \approx$ -45 mV/K [45, 52] (Fig. 1.5). The possession of such a large thermopower has seen numerous investigations into potential technological applications of this effect [37]; however, the thermoelectric figure of merit, $ZT = S^2T/\kappa\rho$, is quite low owing to the high thermal conductivity (κ) and electrical resistivity (ρ) [52]. While the microscopic origin of the high thermopower is not well understood, it has been conjectured to arise from strongly renormalised carrier masses, the transport of which may be assisted through the phonon-drag effect [53–56]; however, a detailed understanding of the details governing this interplay is yet to be fully realised [57].

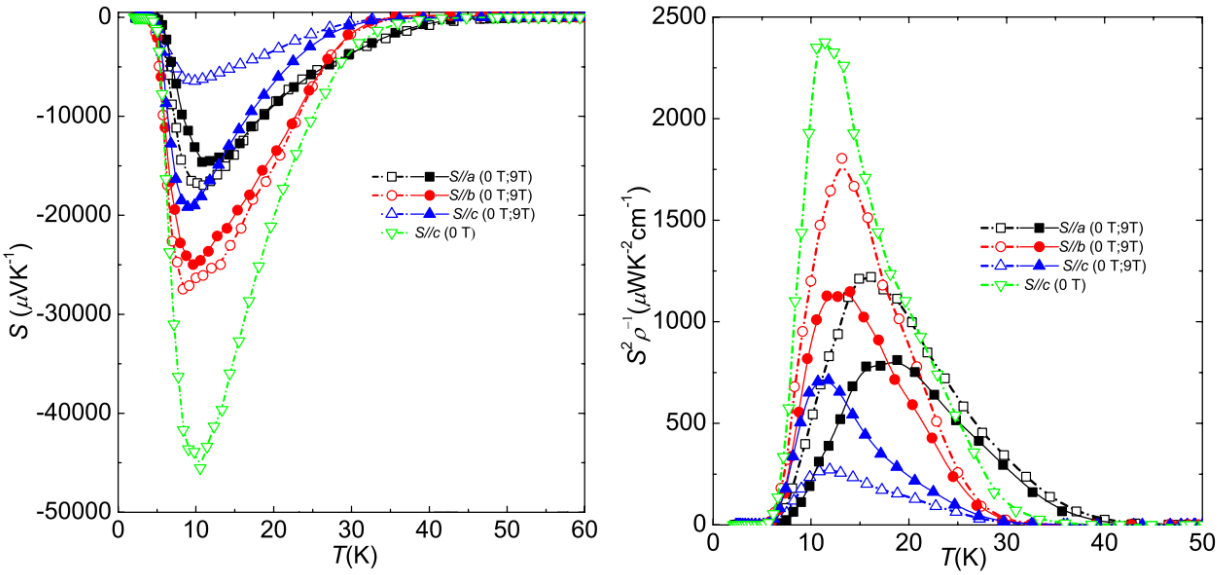

Fig. 1.5. Colossal Seebeck effect in $FeSb_2$. Seebeck coefficient, S (left) and thermoelectric power factor, $S^2\rho^{-1}$ (right), where ρ denotes the electrical resistivity. T is the temperature. Curves correspond to current orientations and magnetic field strengths as indicated. A colossal value of $S \approx$ -45 mV/K is reported for $T \approx 10$ K. Figure adapted from ref. [45] and reproduced with permission.

As a corollary to these thermoelectric properties, the electrical transport behaviour of $FeSb_2$ has been studied by several groups. Two indirect bandgaps have been reported, of sizes ≈ 14 meV (above 20 K) and ≈ 3 meV (at lower temperatures) [58, 59], with Hall effect studies indicating the presence of multiband competition [52, 60]. Meanwhile, optical conductivity measurements detect a much larger direct bandgap of 130 meV [50].

Further effects of the strongly interacting ground state of this material have been uncovered by introducing small doping quantities of Te [61], Co [62], and Sn [63] that reveal a proximate transition to a heavy-fermion metallic state. A similar doping-induced evolution, from strongly correlated insulator to disordered Fermi liquid, has previously been observed in the related compound iron monosilicide (FeSi) [64–66]. FeSi also exhibits several characteristics of Kondo insulator-like strong correlations [37, 67, 68]. Recent elec-

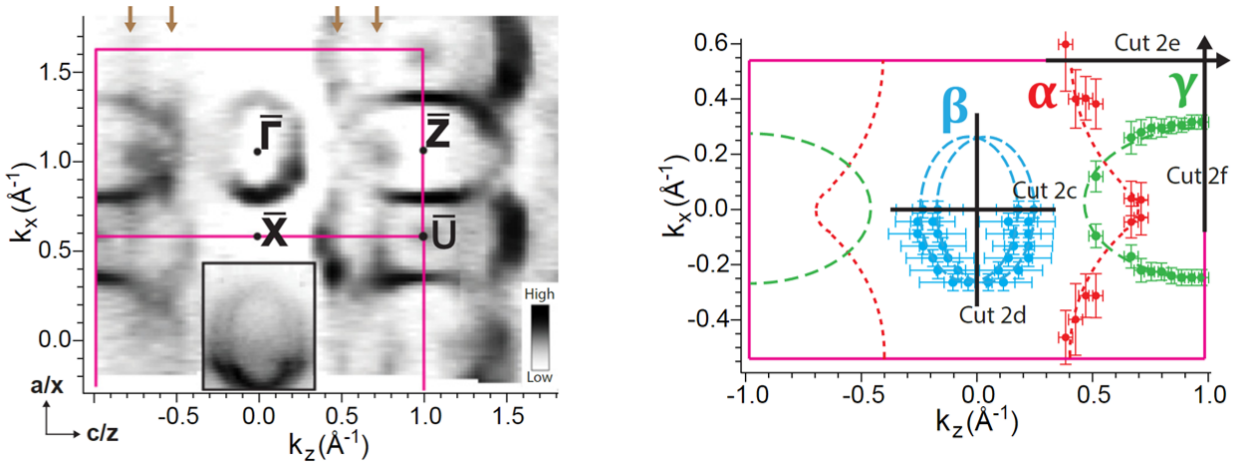

Fig. 1.6. Metallic surface state on the $FeSb_2$ (010) surface. $FeSb_2$ angle-resolved photoemission spectra (left) and interpreted surface Fermi surface sections (right). Figure adapted from ref. [46] and reproduced under a Creative Commons license.

trical transport measurements on FeSi have indicated the presence of conductive metallic surface states [69] – an interesting similarity with recent angle-resolved photoemission spectroscopy results on $FeSb_2$ [46] (Fig. 1.6) – strongly reminiscent of previous findings on SmB_6 [70, 71]. The relation of these findings to the case of $FeSb_2$ will be explored in chapter 6.

1.4 Thesis outline

This dissertation is organised as follows. Chapter 2 introduces some relevant theoretical concepts pertaining to magnetic quantum oscillations, while chapter 3 gives an overview of the nascent field of unconventional insulating materials. In chapter 4 the experimental methods of sample preparation and subsequent measurement techniques are discussed. Chapter 5 examines the magnetic properties of $FeSb_2$ to high magnetic fields, and reveals that the insulating bulk exhibits magnetic quantum oscillations periodic in inverse magnetic field, indicative of an unconventional insulating Fermi surface. Three regimes of

sharply contrasting insulating behaviour are identified and explored, with the unconventional insulating quantum oscillations found to be intimately connected to a metamagnetic transition, pointing to a magnetic origin to this phenomenon. Chapter 6 presents a series of electrical measurements on $FeSb_2$, which indicate the presence of surface dominated conduction at low temperatures, leading onto a discussion of anomalous non-Ohmic resistivity characteristics in chapter 7, before concluding remarks are delivered in chapter 8.

2

Landau quantisation and associated oscillatory magnetic phenomena

It's still magic, even if you know how it's done.

– Sir Terry Pratchett, *A Hat Full of Sky*

2.1 Landau quantisation of fermionic quasiparticles

One of the most powerful techniques for probing a material's Fermi surface is through the observation of quantum oscillations. This technique yields very high resolution across each axis of **k**-space, along with important material parameters such as the (cyclotron) effective mass and the mean free path. However, such measurements are often challenging to perform as they require high crystalline quality, low temperatures, and high magnetic fields.

For free electrons in a magnetic field, **B**, the Schrödinger equation may be solved directly; however this is not the case when subjected to the periodic potential of a crystal lattice. Nevertheless, a semiclassical picture can be obtained through the Bohr-Sommerfeld

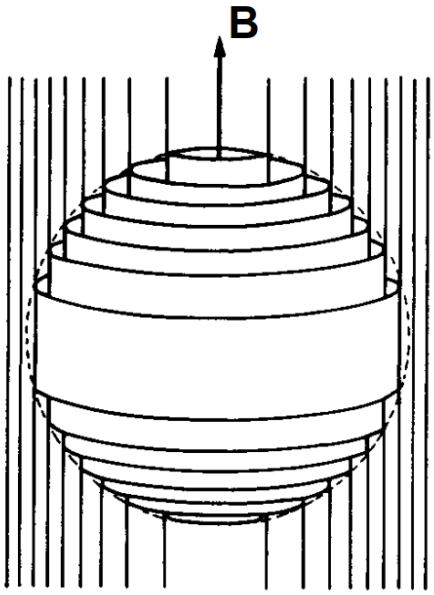

Fig. 2.1. Landau tubes within a spherical Fermi surface. As the magnetic field, **B**, is increased in strength, successive Landau levels cross the Fermi energy, resulting in the manifestation of magnetic quantum oscillations. Figure adapted from ref. [18] and reproduced with permission.

quantisation condition [72].

For $|\mathbf{B}| \neq 0$, electrons form orbits due to the Lorentz force. Using this semiclassical picture, with the electron's field momentum expressed in a gauge-invariant manner, it may be easily shown [73] that the flux threading the particle's real space orbit is quantised, with the corresponding area enclosed by this orbit in reciprocal space, $\mathcal{A}$, being equal to

$$\mathcal{A} = \frac{2\pi e}{\hbar} B \left(n + \frac{1}{2} \right), \tag{2.1}$$

where n is an integer and $\hbar$ is the reduced Planck's constant. (A full treatment is given in the comprehensive review by Shoenberg [18].)

Furthermore, in a crystal, the introduction of a magnetic field causes the allowed **k**-states to no longer form a neat periodic lattice, but instead they superimpose to form a set of concentric cylinders of quantised cross-sectional area termed "Landau tubes" (fig. 2.1). At zero temperature, only those tubes of radius $r < k_{\mathrm{F}}$ will be populated, where k_{F} denotes the Fermi wavevector (and for a spherical Fermi surface, the cross sectional area $\mathcal{A} \equiv \pi k_{\mathrm{F}}^2$). As the field strength is increased, the Landau tubes' radii shall also increase. When $r = k_{\mathrm{F}}$, at a certain field strength for each particular Landau tube, there will be a sudden increase in the density of states, $g(E_F)$. With increasing $|\mathbf{B}|$, one Landau tube after another will satisfy this condition, at field values given by:

$$B_n = \frac{\hbar \mathcal{A}}{2\pi e} \frac{1}{\left(n + \frac{1}{2}\right)}. \tag{2.2}$$

This allows us to derive the Onsager relation [74], relating the oscillatory period of $g(E_F)$ to the Fermi surface's cross-sectional area:

$$\Delta\left(\frac{1}{B}\right) = \frac{1}{B_{n+1}} - \frac{1}{B_n} = \frac{2\pi e}{\hbar} \frac{1}{\mathcal{A}}. \tag{2.3}$$

The frequency of the oscillations (in units of Tesla) is thus simply given by the reciprocal of eqn. 2.3.

The corollary to this result is that properties that are analytically related to the free energy, such as the magnetisation, will exhibit oscillatory components periodic in inverse magnetic field strength. The experimental observation of quantum oscillations in the magnetisation is termed the de Haas-van Alphen (dHvA) effect [75], whereas the likewise observation in the electrical resistivity is termed the Shubnikov-de Haas (SdH) effect [76]. (It should be noted that although resistivity is not analytically related to the free energy, it does have a strong dependence on $g(E_F)$ [77]).

2.2 The theory of Lifshitz and Kosevich

Lifshitz and Kosevich extended the work of Onsager, by performing a detailed analytical study of the dHvA effect as a measurement of the Fermi surface, for arbitrary dispersion and including the effects of spin paramagnetism [78]. For brevity, we shall focus on the aspects of the Lifshitz-Kosevich (LK) theory that relate most pertinently to the experimental quantum oscillation measurements presented in chapter 5.

For the oscillatory component of magnetisation measured by the dHvA effect, $\widetilde{M}$, of a (metallic) single crystal specimen, a concise form of the LK formula may be written as

$$\widetilde{M} \propto R_T R_{\mathrm{D}} R_S \cdot \sum_f \sin\left(\frac{2\pi f}{B} + \phi\right), \tag{2.4}$$

where f denotes a specific oscillatory frequency branch corresponding to a Fermi surface extremal orbit area (from eqn. 2.3), B is the magnetic field strength, ϕ is the oscillatory phase, and R_T, R_{D}, and R_S denote damping factors for the effects of finite temperature, impurity scattering, and spin-splitting, respectively [18, 79]. To change eqn. 2.4 from a proportionality to an equality generally requires careful consideration of the specific material in question - for detailed treatments, see for example refs. [18, 80]; however, the core features of the theory can be captured by consideration of eqn. 2.4.

2.2.1 Damping factors

The effect of finite temperature

The above discussion of successive Landau tubes crossing the Fermi energy under the modulation of a magnetic field was contextualised in the setting of zero temperature. For temperature $T = 0$ K, the Fermi-Dirac distribution function, $f(\epsilon) = \left(\exp\left[\frac{\epsilon-\mu}{k_{\mathrm{B}}T}\right] + 1\right)^{-1}$ where ϵ is energy, k_{B} is the Bolztmann constant, and the chemical potential $\mu\,\big|_{T=0} \equiv E_{\mathrm{F}}$, is a sharp step function going from 1 to 0 at the Fermi energy (Fig. 2.2). However, at elevated

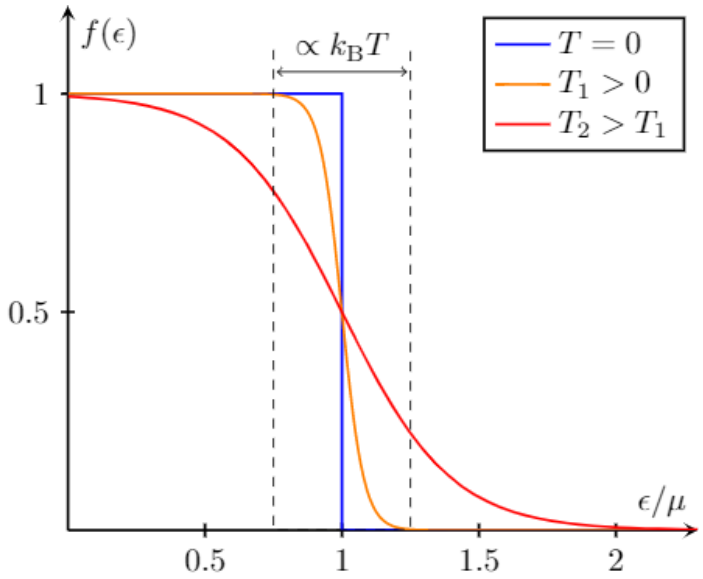

Fig. 2.2. Smearing of the Fermi-Dirac distribution with elevated temperature. The Fermi-Dirac distribution at zero temperature (blue curve) becomes gradually smeared away from a sharp step function as the temperature in increased (orange and red curves). Figure created by the author utilising open source software under an MIT license [81].

temperatures this becomes smeared out as thermal fluctuations allow for higher energy states to be occupied (within a characteristic width of $\sim k_B T$) [77]. As it is the sharpness of this step function at $\epsilon = E_F$ that gives rise to magnetic quantum oscillations, the effect of elevated temperatures is thus to dampen the quantum oscillatory amplitude.

The temperature damping term R_T in eqn. 2.4 has the form

$$R_T = \frac{X}{\sinh X} \tag{2.5}$$

where

$$X = \frac{2\pi^2 k_B T m^*}{e\hbar B}; \tag{2.6}$$

thus, an effective cyclotron mass, m^*, can be found by fitting the quantum oscillatory amplitude to eqn. 2.5 as a function of temperature.

The effect of impurity scattering

In real bulk 3D materials, with $\sim N_A$ unit cells, there shall always exist some number of crystalline defects. These may include inclusions of other elements (typical in flux growth processes), or imperfections in the crystalline lattice itself, such as dislocations (typical in high temperature growth processes).

The presence of such impurities results in scattering of the quasiparticle orbits that give rise to the dHvA effect; this leads to a shorter quasiparticle mean free path, $\lambda = \tau v_F$, where v_F is the Fermi velocity and the impurity scattering rate is given by τ^{-1}. The impurity damping term R_D in eqn. 2.4, also commonly referred to as the Dingle damping term [82], takes the form

$$R_D = \exp\left(\frac{-B_D}{B}\right) \tag{2.7}$$

where the damping factor

$$B_D = \frac{\pi\hbar k_F}{e\lambda}. \tag{2.8}$$

In real space, an orbit's radius r corresponding to a frequency branch f is given by

$$r = \sqrt{\frac{2\hbar f}{eB^2}}. \tag{2.9}$$

It is therefore often experimentally advantageous to perform measurements at high magnetic field facilities (such as those presented in chapter 5) in order to resolve high frequency quantum oscillations, due to the fact that the exponent of eqn. 2.7 is inversely proportional to the magnetic field strength. Additionally, given that λ is fixed for a given

sample, r is inversely proportional to B, implying that for sufficiently large B orbits for large f will be able to be accommodated without scattering off impurity content. In tandem, these two considerations – the exponential damping of oscillatory amplitude, and the effect of reducing real space orbit sizes with field – makes access to high magnetic field strengths a valuable tool for dHvA studies. However, it should be noted that such measurements are often experimentally challenging due to the introduction of large vibrational noise components that must be balanced against the enhancement in signal from these considerations.

The effect of spin splitting

The final damping factor of eqn. 2.4, R_S, concerns the effect of Zeeman splitting for opposite spin quasiparticles in a magnetic field. The effect of this is to lift the degeneracy of the two spin components, separating their energy levels by

$$\Delta\epsilon = g^* \frac{e}{2m_e} \mathbf{s} \cdot \mathbf{B} = \pm g^* \frac{e\hbar}{4m_e} B, \tag{2.10}$$

where g^* is the spin g-factor, and $\mathbf{s}$ the spin [80]. The contribution of spin-up and spin-down quasiparticle orbits leads to a phase shift of the total oscillatory waveform [18]. This can be described through a multiplicative attenuation factor of the oscillatory amplitude by writing the spin splitting damping factor as

$$R_S = \cos\left(\frac{\pi g^* m_s}{2m_e}\right), \tag{2.11}$$

where it should be noted that the effective spin-mass, m_s, is renormalised solely by electron-electron interactions (unlike the term m^* in eqn. 2.6 that is renormalised by both electron-phonon and electron-electron interactions) [18, 83].

2.2.2 Further considerations

The investigation of magnetic oscillations in metals has proved very fruitful over the past century, with the theory governing magnetic quantum oscillations having been highly developed and extended since the seminal work by Lifshitz and Kosevich [78]. The discussion of the LK theory presented above was deliberately focussed on the most salient aspects governing the fundamental properties of magnetic quantum oscillatory phenomena.

In some cases, additional effects will be important to take into consideration. For example, when the curvature of the Fermi surface becomes large, so too does the number of Landau tubes intersecting it. This leads to a marked reduction in quantum oscillatory amplitude, as the depopulation of allowed energy levels is almost constant in field (whereas, for the simple spherical case given above, the curvature is low hence the depopulation is very sharp).

Furthermore, throughout this discussion we have assumed that the applied magnetic field $\mu_0 H = B$, i.e. that the magnetisation of the sample itself is negligible compared to the magnitude of the applied field. However, should the sample become strongly magnetised by the application of a large magnetic field, magnetic interaction effects can become strong, whereby the oscillating magnetisation of the sample can approach the period H^2/f [73]. This can modify the waveform of the oscillations, greatly increasing the harmonic content [18, 84].

Additionally, we have assumed that E_F is independent of field, which is true for the vast majority of cases, provided that B/f remains small. As B/f approaches unity, we begin to enter the quantum limit, which is easily experimentally attainable for materials such as bismuth [85, 86]. Finally, another important phenomenon that should be mentioned is the effect of magnetic breakdown, where quasiparticles can tunnel from one Fermi surface section through forbidden regions of k-space in order to reach an adjacent Fermi surface section separated by a small energy ε [87]. The criterion for the occurrence of magnetic breakdown may be expressed as

$$\hbar\omega_c \gtrsim \varepsilon^2/E_{\mathrm{F}}, \tag{2.12}$$

where ω_c is the cyclotron frequency [18, 87].

2.3 Probing the dHvA effect by torque magnetometry

For the sake of simplicity, when introducing eqn. 2.4, a concise form was deliberately chosen in order to qualitatively highlight the most important general aspects of the LK theory. However, in order to draw quantitative interpretations from quantum oscillation data, it is necessary to address specific features of both the measurement technique employed and the material being studied. In the case of 2D materials, reduced dimensionality can often simplify the problem, allowing for insightful quantitative information about the density of states of the system to be analytically obtained [88, 89].

For the case of torque magnetometry performed on a 3D bulk metal – for which the experimental procedure shall be introduced in section 4.2.1 – the first harmonic of the oscillatory component of the torque, $\Delta\tau$, may be written as

$$\Delta\tau = \sum_{\text{orbits}} \frac{\partial f}{\partial\theta} \frac{Ve^{5/2}}{\hbar^{1/2}\pi^2 m_e} B^{3/2} \left(2\pi \left|\partial^2_{\hat{B}}\mathcal{A}\right|\right)^{-1/2} R_T R_{\mathrm{D}} R_S \cdot \sin\left(\frac{2\pi f}{B} + \phi\right), \tag{2.13}$$

where $\hat{B}$ denotes the effective magnetic field wavevector (to which the plane of $\mathcal{A}$ is orthogonal), V is the volume of the metal, and the other symbols are as introduced above [18, 79].

2.3.1 Determination of experimental torque amplitude

Torque magnetometers measure variations in a material's magnetic anisotropy as a function of magnetic field, $\mathbf{B}$ [90]. The torque, $\boldsymbol{\tau}$, exerted on a sample of total magnetic moment

$\boldsymbol{\mu}$ is given by $\boldsymbol{\tau} = \boldsymbol{\mu} \times \mathbf{B}$. The measured cantilever displacement, in units of capacitance, may be converted to bulk magnetic moment per unit cell through the following procedure.

The proportional change in the capacitance, C, associated with a small deflection of the cantilever from its equilibrium position, denoted by δ, is given by:

$$\tau = \mu B \sin(\theta) = Lk\delta = Lkd \cdot \frac{\Delta C}{C}, \tag{2.14}$$

where θ is the angle between $\mathbf{B}$ and $\boldsymbol{\mu}$, L is the distance along the distal length of the cantilever between the hinge and the sample, and for the final equality we have used the fact that C is inversely proportional to the spacing, d, between the cantilever and base plate.

Defining the magnetic moment in units of Bohr magnetons per unit cell as $p_e = \mu/\mu_\mathrm{B} \cdot V_\mathrm{u.c.}/s^3$, with $V_\mathrm{u.c.}$ the unit cell volume and s^3 the volume of the sample, we may rearrange Eq. 2.14 to obtain:

$$\Delta p_e = \Delta C \cdot \frac{V_\mathrm{u.c.} Lkd}{\mu_\mathrm{B} s^3 BC \sin(\theta)} = \alpha \frac{\Delta C}{B \sin(\theta)}, \tag{2.15}$$

where α is a constant, of units $\mu_\mathrm{B}\mathrm{TF}^{-1}$.

2.3.2 Theoretically expected torque amplitude

By ref. [18] we can re-express eqn. 2.13 to write the theoretical quantum oscillation magnitude of the first harmonic, Ω_0, measured by the torque magnetometry technique in the limit of infinite field, zero temperature, zero impurities, and zero spin splitting, as:

$$\Omega_0 = -\frac{\mu_\mathrm{B}}{2\pi^4}\frac{m_\mathrm{e}}{m^*}\left(\frac{\mathcal{A}^3 B}{f\left|\partial^2_{\hat{B}}\mathcal{A}\right|}\right)^{\frac{1}{2}} \cdot \sin(\theta). \tag{2.16}$$

We can normalise this to give the oscillation amplitude expected per unit cell, p_t:

$$p_t = \frac{|\Omega_0| V_\mathrm{u.c.}}{\mu_\mathrm{B}} \cdot \sin(\theta) = \mathcal{F}(r)\frac{2m_\mathrm{e}}{m^*}\left(\frac{k_\mathrm{F}}{\bar{k}_\mathrm{BZ}}\right)^3\left(\frac{2B}{f}\right)^{\frac{1}{2}} \cdot \sin(\theta), \tag{2.17}$$

where the Fermi wavevector $k_\mathrm{F} \equiv \sqrt{\mathcal{A}/\pi} = \sqrt{2ef/\hbar}$ by eqn. 2.3, $\bar{k}_\mathrm{BZ} \equiv 2\pi/V_\mathrm{u.c.}^{1/3}$ for unit cell volume $V_\mathrm{u.c.}$, and the anisotropy term $\mathcal{F}(r)$ is defined as $\sqrt{2\pi/|\partial^2_{\hat{B}}\mathcal{A}|}$.

When we come to examine the quantum oscillations presented in chapter 5, approximating the effective mass, value of $\sin(\theta)$, and possible range of $f(r)$ as each being in the range 0.1-1 will thereby allow us to estimate the theoretical amplitude for bulk quantum oscillations in the limit of low temperature, infinite field, and zero spin splitting.

3

On the origin of insulating quantum oscillations

If we want to solve a problem that we have never solved before, we must leave the door to the unknown ajar.

– Richard P. Feynman

3.1 Review of unconventional insulators

Samarium hexaboride

In 2014, Li *et al* reported the observation of the dHvA effect in a torque magnetometry study of SmB_6 [21]. The authors interpreted the quantum oscillation data as emanating from a 2D surface state – however, a subsequent report the following year [19] showed that several of the oscillatory frequency branches were almost isotropic in their angular rotation with respect to magnetic field tilt angle, with too large an amplitude to emanate solely from a surface layer, indicating the presence of a three dimensional Fermi sur-

face somehow being hosted within the insulating bulk of the material. Complementary thermal measurements [20] reinforced the evidence in favour of a charge neutral Fermi surface, revealing anomalous specific heat and thermal conductivity properties highly atypical of an electrically insulating phase of matter, implying the presence of charge-neutral fermionic excitations coupling to magnetic fields, but not to electrical fields (at least not in the dc limit).

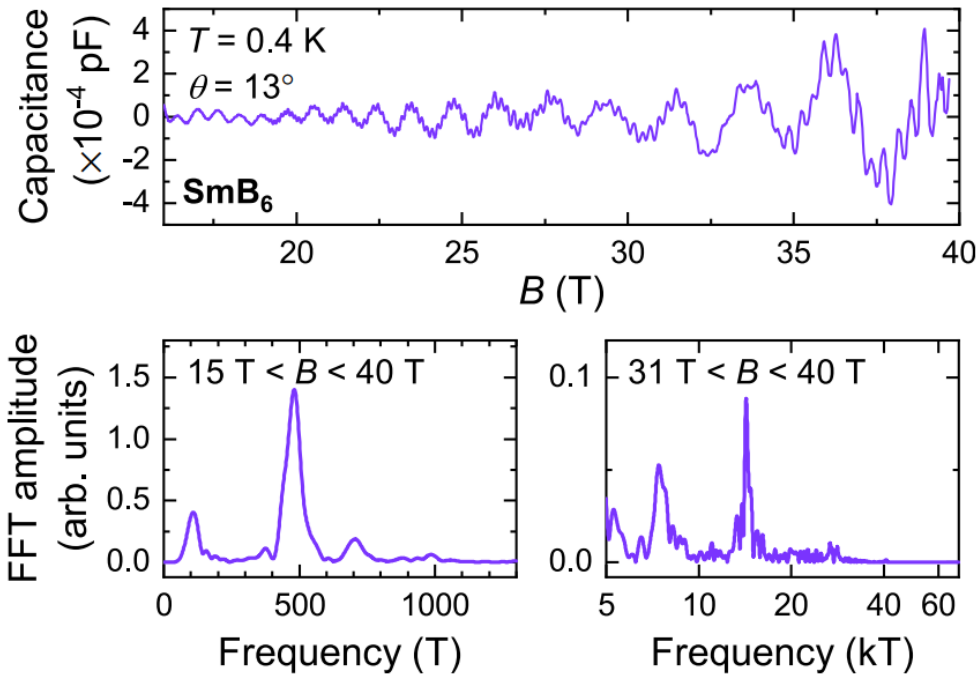

Fig. 3.1. Quantum oscillations from the bulk of the unconventional insulator SmB_6. Large amplitude quantum oscillations are resolved in the magnetic torque of SmB_6 (top), exhibiting multiple frequency branches, as resolved by the fast Fourier transforms (bottom). Figure adapted from ref. [91] and reproduced under a Creative Commons license.

These reports indicative of a charge-neutral Fermi surface in SmB_6 were subsequently questioned by other studies. For example, ref. [92] was unable to reproduce the thermal measurements, whereas ref. [93] reported quantum oscillations from embedded aluminium in flux-grown samples. However, a comprehensive analysis performed in ref. [91]

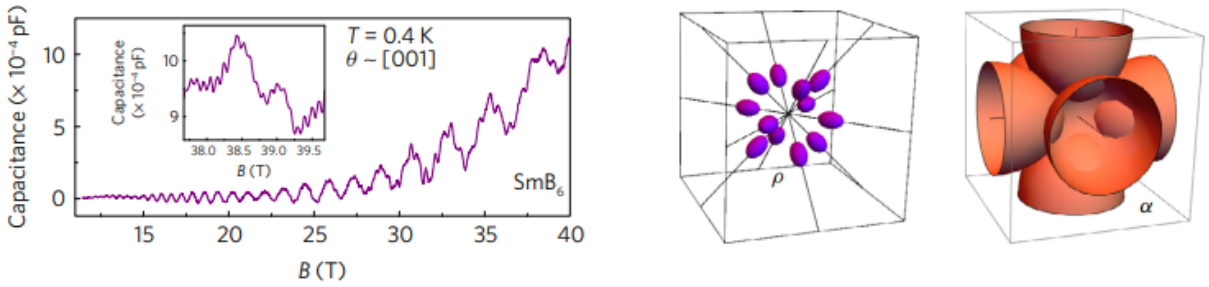

Fig. 3.2. Insulating Fermi surface in SmB_6. dHvA effect of an SmB_6 single crystal measured by capacitive torque magnetometry (left), similar to that presented in Fig. 3.1. Inset shows high frequency components resolved at high magnetic fields. Multiple Fermi surface sheets (right) are observed, corresponding to the different quantum oscillatory frequency branches. High frequencies correspond to the large α sheets, while the lower frequencies indicate the presence of multiple ellipsoidal pockets labelled ρ. Figure adapted from ref. [20] and reproduced with permission of Springer Nature.

shows that the sample purity of specimens studied in refs. [92, 93] is very much inferior to that of the impurity-free SmB_6 samples grown by the floating zone technique that were observed to host quantum oscillations in refs. [19, 20].

Furthermore, several recent studies have corroborated the interpretation of dHvA effect data put forth in refs. [19, 20], of the insulating bulk of SmB_6 possessing a 3D Fermi surface in the absence of a Fermi liquid. For example, in ref. [94] Compton scattering measurements are interpreted to indicate a 'remnant' Fermi surface in SmB_6, where signatures of a bulk Fermi surface are observed. However, despite the resolution of sharp steps indicative of the Fermi level lying in a band, the intensity of the Compton signal is much lower than would be observed for a metal, implying that perhaps only half of the expected quasiparticles are contributing to the Fermi surface signatures. Meanwhile, ref. [95] recently reported bulk magnetoquantum oscillations of the specific heat, exhibiting a similar angular evolution to the dHvA studies of refs. [19, 20] (albeit with seemingly higher effective quasiparticle masses).

While several open questions about SmB_6 remain unresolved [34], the best evidence in favour of the veracity of the phenomenon of unconventional insulating Fermi surfaces

later came from corollary discoveries across other insulating materials families.

Ytterbium dodecaboride

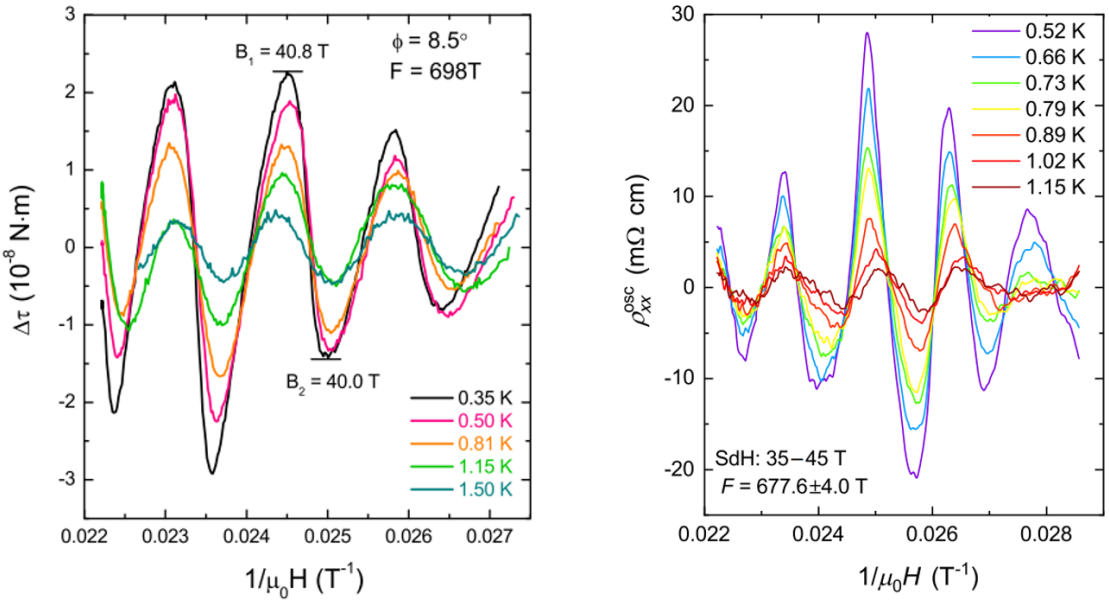

Fig. 3.3. dHvA and SdH effects observed in YbB_{12}. Quantum oscillations in the magnetic torque (left) and electrical resistivity (right) of YbB_{12}. Both measurement techniques reveal a relatively slow prominent oscillation of frequency ≈ 700 T. Left panel adapted from ref. [23] and reproduced with permission of AAAS; right panel adapted from ref. [96] and reproduced under a Creative Commons license.

The rare earth dodecaboride YbB_{12} is a close cousin to SmB_6, hence it was a natural material to next be investigated. It was also found to manifest the dHvA effect [22] – but strikingly, it also exhibited the SdH effect at very high fields [23, 97, 98]. The lack of SdH but presence of dHvA oscillations in SmB_6 was taken to imply the attendance of charge neutral fermions – while YbB_{12} has also been seen to exhibit anomalous thermal properties [99], the manifestation of quantum oscillations in the highly insulating resistivity was an intriguing new development. Furthermore, despite the chemical sim-

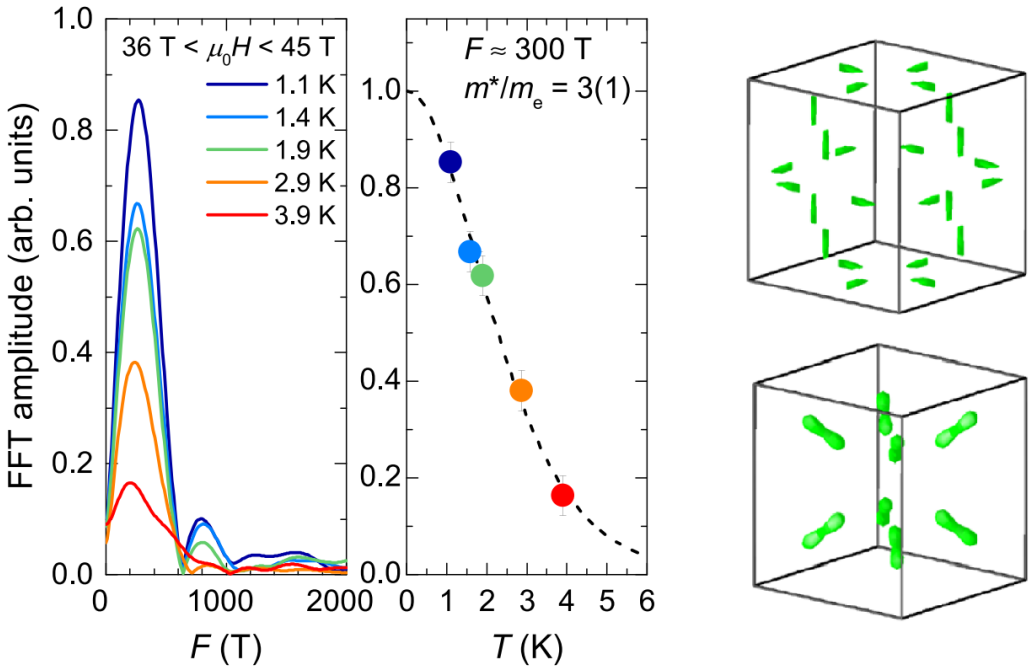

Fig. 3.4. Insulating Fermi surface in YbB_{12}. Fast Fourier transform amplitudes (left) of YbB_{12} dHvA data at incremental temperatures, and corresponding Lifshitz-Kosevich temperature dependence. Small Fermi surface sections (right) are found to possess relatively high masses - in stark contrast to SmB_6. Figure adapted from ref. [22] and reproduced with permission of IOP Publishing.

ilarities between the two rare-earth borides, their quantum oscillatory properties were very different, with SmB_6 yielding features indicative of a light, conduction electron-like Fermi surface, whereas YbB_{12} exhibited a small, heavy Fermi surface akin to that of a semimetal. These contrasting observations hinted strongly that there may be numerous possible routes to the attainment of Fermi surfaces in unconventional insulators.

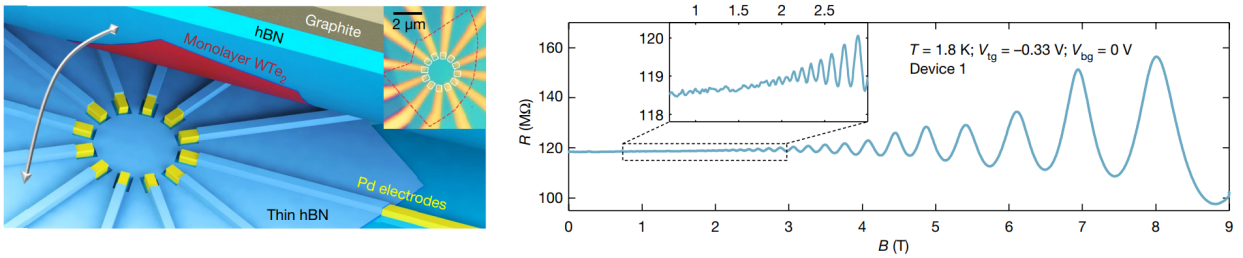

Fig. 3.5. Magnetoquantum oscillations reported in a monolayer tungsten ditelluride device. *Left:* Schematic illustration of the device design. *Right:* Remarkably, despite exhibiting a resistance in excess of 10^8 Ω, the magnetoresistance profile is completely dominated by an oscillatory component periodic in inverse field. Figure adapted from ref. [24] and reproduced with permission of Springer Nature.

Beyond Kondo insulators

Recently, two very different materials – monolayer tungsten ditelluride (WTe_2) [24] and bulk crystals of the alpha allotrope of ruthenium trichloride (α-$RuCl_3$) [25] – have also been reported to exhibit oscillatory phenomena periodic in inverse magnetic field, despite both being strongly insulating. However, at present there are some outstanding questions over these discoveries.

WTe_2 is a Weyl semimetal, with isolated monolayers previously shown to have conducting helical edge states surrounding an insulating bulk [100]. In 2021 it was reported in ref. [24] that this bulk insulating interior of WTe_2 monolayers exhibits magnetic quantum oscillations in electrical transport – despite being extremely resistive, of order 10^8 Ω (Fig. 3.5). However, this result was subsequently questioned in ref. [101], which posited that the oscillatory signal may instead be an artifact of the graphite gate. While ref. [24] includes some data collected on devices fabricated without graphite gates, which do show an oscillatory component, these data are not as convincing as those collected from graphite gated devices such as in Fig. 3.5. As such, it remains to be seen whether these results are corroborated by other groups; however, promising new findings by the authors of ref. [24] indicate that other related materials may also exhibit insulating quantum oscillations [102].

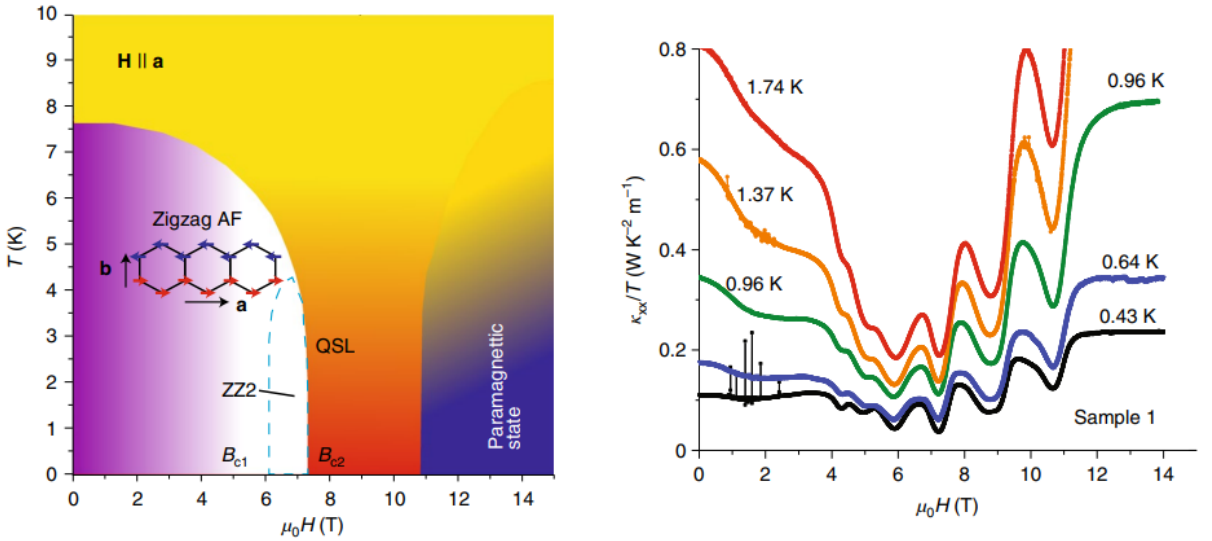

Fig. 3.6. Oscillations of the thermal conductivity in the putative spin-liquid state of α-RuCl$_3$. *Left:* Phase diagram for magnetic field applied along the a-axis of α-RuCl$_3$. *Right:* Longitudinal thermal conductivity divided by temperature, κ_{xx}/T, versus applied magnetic field strength oriented along the a-axis. An oscillatory profile of low frequency is resolved, which the authors assert to be periodic in inverse magnetic field strength (despite only a small number of wavelengths being observed before transitioning into the paramagnetic state above ≈ 11 T). Figure adapted from ref. [25] and reproduced with permission of Springer Nature.

α-RuCl$_3$ is a magnetic insulator, widely regarded to be a Kitaev quantum spin liquid candidate [103, 104]. In 2021 it was reported by ref. [25] that in the putative spin liquid phase, large amplitude low frequency magnetic oscillations are exhibited by the longitudinal thermal conductivity. The authors fit the oscillatory maxima and minima (admittedly small in number) and make the interpretation of them being periodic in inverse magnetic field strength, and hence indicative of Landau quantisation. Interestingly, the oscillations are quenched upon transitioning into the paramagnetic state above ≈ 11 T.

However, this interpretation has recently been questioned by ref. [105], which reproduces the experimental results and interprets them as being indicative not of magnetic quantum oscillations originating from chargeless itinerant quasiparticles, but instead at-

tributes the features to a series of field-induced phase transitions. Recently, another group investigating this material has also interpreted their preliminary observations in the context of this model of magnetic phase transitions as opposed to magnetic quantum oscillations [106]; hence, careful further study of this phenomenon is urgently called for.

However, the possibility that WTe_2 and α-$RuCl_3$ may be potential new additions to the list of unconventional insulating materials discovered to date opens the horizon of this nascent field, implying that the range of material classes – and likely the causal microscopic mechanisms – of this phenomenon may be much more diverse than initially assumed purely in the case of Kondo insulators. As we shall see in chapter 5, $FeSb_2$ is another member of the unconventional insulating family – however, $FeSb_2$ exhibits markedly different characteristics than any of the materials reviewed in this chapter, affording us a much clearer view to the origin of this paradoxical phenomenon.

3.2 Theoretical proposals for insulating Fermi surfaces

As discussed in chapter 2, our conventional theoretical framework describing magnetic quantum oscillations [18, 107–112] is premised on Landau quantisation of itinerant (charged) fermionic quasiparticles having a large number of proximate available energy levels, thus being exclusive to Fermi liquids in metallic materials at low temperature. Thus, since the seminal report of the dHvA effect emanating from the insulating bulk of SmB_6 [19], a multitude of new theoretical proposals have been put forth [113–153] in attempt to reconcile the paradoxical observations of Fermi surfaces hosted within the bulk of electrical insulators.

A number of these theories postulated some extrinsic origin to the observed magnetic quantum oscillations, such as through substitutive impurities introducing impurity bands, or invoking the effects of vacancies [125–128]. However, the strong correlation between sample purity and quantum oscillatory amplitude in later studies [23, 91, 97], the correspondence between the observed bulk quantum oscillations and attendant bulk ther-

mal properties [20, 99], and the variety in observed quantum oscillations across disparate unconventional insulating materials families argues strongly against such an explanation.

Other theories seek to reconcile these experimental observations by attributing them to tunnelling effects, or by proposing Kondo breakdown at the surface [137–141]. However, tunnelling effects are unlikely to be the case due to the disagreement between these models' temperature dependence of quantum oscillation amplitude with that observed experimentally. Kondo breakdown models are also unlikely, as while these theories were posited in the case of SmB_6, later work on YbB_{12} – which exhibits an experimentally accessible insulator–metal transition at $\approx$ 50 T – revealed strong similarities between the (bulk) metallic Fermi surface and (bulk) insulating Fermi surface. In addition, the fact that YbB_{12} exhibits both dHvA and SdH signatures characteristic of a bulk 3D insulating Fermi surface, but SmB_6 only exhibits such features through the dHvA effect, indicates that there may be numerous possible routes to manifesting an insulating Fermi surface. The recent observations in the disparate materials WTe_2 and α-$RuCl_3$ further underline this point. As we shall see in chapter 5, $FeSb_2$ exhibits bulk magnetic properties strongly interconnected with the insulating quantum oscillations, helping to shed light on the microscopic origins of this phenomenon.

A number of proposed theories have instead focused on the intriguing possibility that these materials possess low energy charge-neutral excitations, of either excitonic [117–122] or Majorana [113–116] character. Thus, they are posited to be able to host neutral Fermi surfaces. Those exploring excitonic effects build on previous work that considered potential charge-neutral Fermi surfaces in single band Mott insulators [154–157]. As an example, ref. [118] posits that the presence of strong correlations and intermediate valence allows the bulk of SmB_6 to host electrically neutral gapless fermionic excitations (Fig. 3.7). The authors refer to these excitations as composite excitons, and show that they can qualitatively capture several of the anomalous properties of this material.

Alternatively, refs. [113–116] use the fact that Majorana fermions are (by definition) their own antiparticle [158], and hence charge-neutral, to come to a similar inference that SmB_6 hosts a neutral Fermi surface. This was also partly motivated by the observation

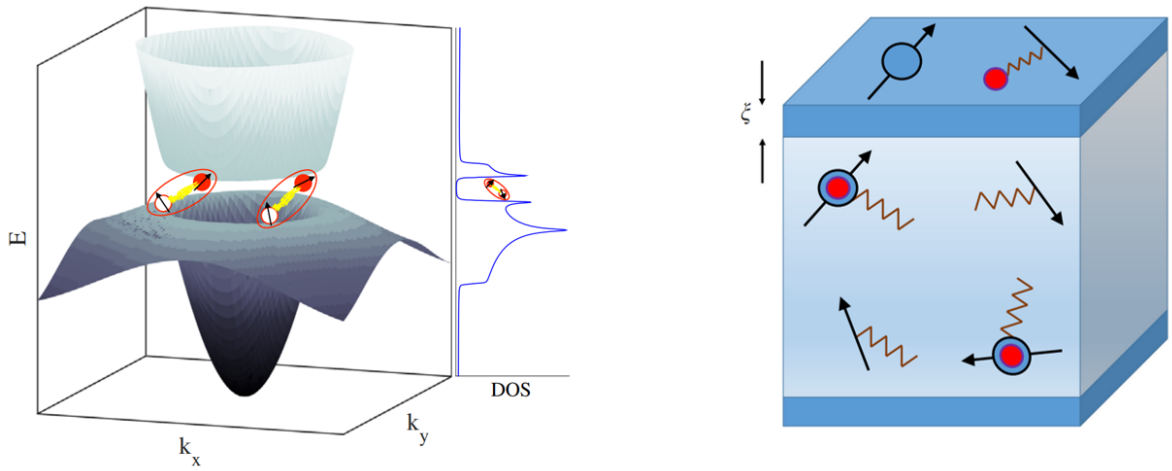

Fig. 3.7. Charge neutral excitonic models for SmB_6. *Left:* Computed Mexican hat-like band structure, caused by strong Coulombic repulsion between localised samarium f states in SmB_6, giving rise to a large density of states (DOS). This interaction is posited to give rise to the excitonic pairs (in red ellipses). *Right:* Alternative excitonic model for SmB_6, wherein the bulk hosts a composite exciton Fermi liquid, which can host a charge-neutral Fermi surface and thus give rise to magnetic quantum oscillations. Within a length scale ξ of the surface, fermionic composite excitons are posited to decouple, resulting in a metallic surface state. Left panel reproduced with permission from ref. [117]. Copyright (2017) by the American Physical Society. Right panel reproduced from ref. [118] under a Creative Commons license.

that SmB_6 exhibits quantum oscillations in its magnetisation but not its resistivity – as we shall see in later chapters, $FeSb_2$ is similar in this regard, while also exhibiting fast, light oscillations reminiscent of SmB_6 (and quite distinct from the heavy slow oscillations of YbB_{12}). The discovery of an analogous material in this respect thus helps to constrain this multitude of theoretical speculation. Indeed, further constraint on future theoretical models is forthcoming from the anomalous magnetic effects of $FeSb_2$ – which at the highest fields sees a metamagnetic insulator–to–insulator transition wherein the anomalous insulating quantum oscillations are abruptly quenched, in stark contrast to numerous models explored above [125–128, 137–141].

4

Experimental methods

It is not enough to acquire wisdom; it is necessary to employ it.

– Marcus Tullius Cicero

This chapter outlines sample preparatory procedures and experimental measurement techniques. Growth processes for obtaining single crystal specimens of $FeSb_2$ are discussed, before leading onto a discussion of characterisation experiments. A suite of sample purity analyses is presented, establishing the very high purity of the crystals studied in this thesis. Measurement techniques for various experiments at high magnetic fields are introduced, encompassing various magnetic and electrical physical properties, for which data on $FeSb_2$ are presented in the following chapters.

4.1 Sample preparation

4.1.1 CVT growth

All measurements on $FeSb_2$ presented in this thesis were performed on samples grown by Kejun Xu of the Shen group, Stanford University. Single crystal samples were grown by the chemical vapour transport (CVT) method. The low-temperature CVT method avoids the possibility of introducing extraneous flux inclusions, impurities, and disorder through higher temperature growth conditions. Starting materials of 99.995%at Fe and 99.999%at Sb, in stoichiometric ratio, were placed at one end of a quartz tube along with approximately 1 mg/cm^3 of I_2 (as the transport agent), and sealed under vacuum. Growth was conducted at a 750 °C – 650 °C temperature gradient and was maintained for one week. After the growth, the charge end was quenched to rapidly condense any remaining vapour, in order to preserve pristine surfaces on the $FeSb_2$ crystals. Typical as-grown single crystals are $\approx 1 \times 1 \times 1$ mm^3 in size, with the largest specimens weighing up to ≈ 5 mg each.

4.1.2 $FeSb_2$ sample characterisation and purity determination

In order to quantify the purity of our $FeSb_2$ crystals, a suite of characterisation measurements was undertaken.

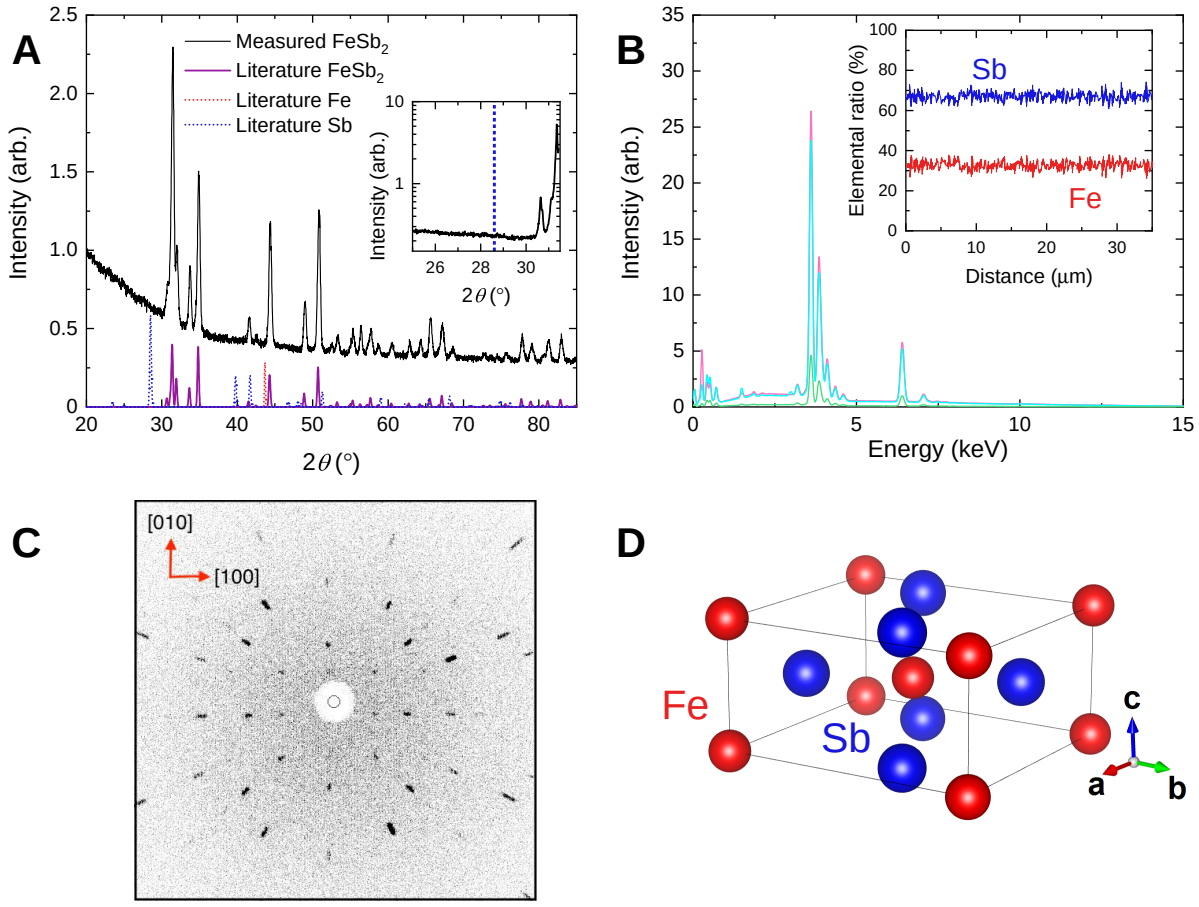

Fig. 4.1. X-ray diffraction studies of $FeSb_2$. **(A)** Measured powder x-ray diffraction data, black line, plotted alongside purple, blue, and red lines indicating literature data for $FeSb_2$ [159], elemental Sb [160], and elemental Fe [161], respectively. The smooth background at low 2θ is primarily due to fluorescence signal. All peaks correspond to the known crystallographic phase of $FeSb_2$; no extraneous peaks from impurity phases were resolved. *Inset:* The inset shows the same sample in the region around the largest Sb peak from the literature, at $2\theta = 28.6°$ (marked in blue), plotted on a logarithmic scale. No evidence of elemental Sb inclusions were resolved, to the resolution of this measurement. **(B)** Energy-dispersive x-ray diffraction spectrum. A single crystal of $FeSb_2$ was measured using a ZEISS GeminiSEM 300 running 20 kV, using an Oxford Instruments X-MaxN 50 EDS detector. No deviations from the expected stoichiometry were observed within experimental limitations in three area scans of different faces of a $FeSb_2$ sample, shown in cyan (225 μm^2), pink (225 μm^2), and green (1200 μm^2).

Fig. 4.1. (cont.) *Inset:* A line-scan along a surface of the $FeSb_2$ single crystal, showing no indication of Fe or Sb inclusions within the resolution of the measurement. **(C)** Lauegram with x-ray beam aligned along the [001] direction of an as-grown CVT $FeSb_2$ specimen. Single crystallinity is evident, with all spots as expected for this material [162]. The [010] and [100] directions are indicated for reference. **(D)** Marcasitic crystal structure of $FeSb_2$, with lattice constants: $\hat{a} = 5.83$ Å, $\hat{b} = 6.53$ Å, and $\hat{c} = 3.19$ Å [163, 164]. The Fe ions are surrounded by octahedra of Sb ions, which share an edge in the (110) plane.

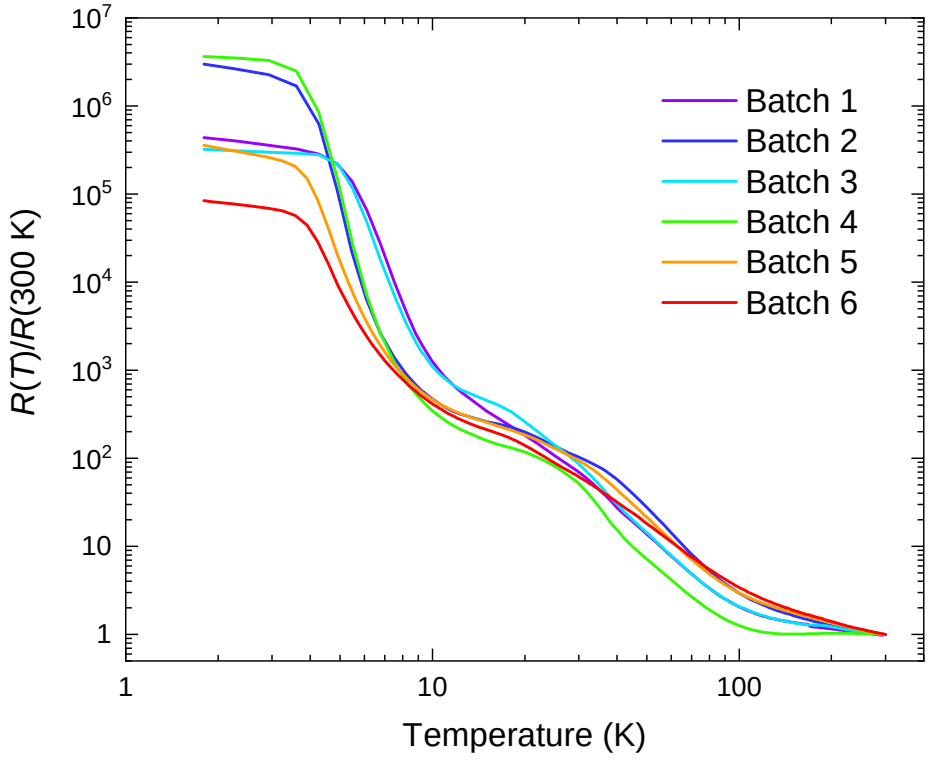

Fig. 4.2. Inverse residual resistivity ratios for various $FeSb_2$ sample batches. Resistance R at temperature T divided by the resistance at 300 K, for various $FeSb_2$ sample batches as indicated, plotted versus temperature. Sample batches were grown by our collaborators in Stanford, with different growth batches often trialling starting materials from differing sources, in order to optimise the procedure for obtaining high quality crystals as characterised by high iRRR values.

iRRR

All samples presented in this thesis were initially screened by their inverse residual resistivity ratios [iRRR ≡ $R(T = 2\text{ K})$ / $R(T = 300\text{ K})$, where R is resistance and T is temperature]. A high iRRR is indicative of high sample purity – whereas a low iRRR indicates that the presence of defects such as vacancies, grain boundaries, substitutive impurities etc are contributing to higher rates of scattering (and thus a lower iRRR). Samples investigated in this dissertation exhibit iRRR values up to $\sim 10^6$ (Fig. 4.2), an order of magnitude higher than in previous reports, signalling very high purity [58, 165]. For the quantum oscillation study presented in chapter 5, samples with iRRR values $> 10^6$ were selected.

It should be noted that, as shall be examined in chapters 6 & 7, $FeSb_2$ exhibits surface dominated conduction at low temperatures that is highly non-Ohmic in character. Therefore, an identical procedure for obtaining the iRRR was performed on each measured sample. Furthermore, it should also be noted that the development of surface dominated conduction at slightly different temperatures for differing samples may lead to variations in the obtained iRRR value that are not directly correlated to sample purity. Therefore in future, comparison of iRRR results obtained in the manner performed here, along with the temperature profile of the isolated surface and bulk conductivity components, would be informative with regards to better comparing the effects of sample quality on electrical conductivity.

PXRD

As-grown crystals of $FeSb_2$ were ground into a fine powder for powder x-ray diffraction (PXRD) to identify the primary phase and any impurity phases (Fig. 4.1A). PXRD was performed using Malvern Panalytical X'Pert and Empyrean diffractometers with a Cu Kα excitation source. Coarse scans were performed through 2θ from 25° to 90° over 30 minutes, accompanied by fine scans to check for Sb impurities through 2θ from 24° to 32° over 15 minutes for each scan, with a total of 11 scans added together. All observed peaks correspond to the known crystallographic phase of $FeSb_2$, with marcasitic struc-

ture (Fig. 4.1D). No impurity peaks corresponding to Sb inclusion or any other impurity phases were observed down to < 0.5%at.

EDX

Energy-dispersive x-ray diffraction (EDX) was performed on a single crystal of $FeSb_2$ using a ZEISS GeminiSEM 300 running 20 kV using an Oxford Instruments X-MaxN 50 EDS detector. No deviations from the expected stoichiometry were observed on three separate scans, as shown in Fig. 4.1B. Scans were performed on three regions on different faces of a $FeSb_2$ sample, with surface sizes between 200 μm^2 and 1200 μm^2. The elemental ratios of Fe : Sb for the three regions were found to be 0.494, 0.496, and 0.493 with an error of 0.01 from calibration. To detect potential elemental Sb inclusions, a line scan was performed along 40 µm of the sample to search for any small regions with a possible change in stoichiometry. No elemental Sb (or Fe) inclusions were resolved within the resolution of the measurement. These measurements were performed in collaboration with S. M. Fairclough of the Department of Materials Science, University of Cambridge.

Laue diffractometry

X-ray Laue backscattering imaging was performed with a Multiwire Laue camera to determine the single crystallinity of the grown crystals and to select and orient as-grown single crystal samples. All crystals showed well-defined spots in the Laue diffraction pattern, an example of which is shown in Fig. 4.1C, evidencing high single crystal quality.

Mass spectrometry

Chemical impurity analysis was performed with inductively coupled plasma optical emission spectrometry (ICP-OES) by Exeter Analytical UK Ltd. Samples from the same growth batches as those used in quantum oscillation measurements were used, with a total mass

of 55 mg to allow for a broad multi-element scan with high levels of precision. The samples were digested in a nitric acid matrix under the application of microwave radiation, then introduced to the ICP-OES (in combination with internal standards, to aid precision). Impurity concentration is ruled out to 100 parts per million. The full results are shown in Table 4.1.

Concentration (parts per million)	Elements
< 10	Ag, Al, As, B, Ba, Be, Ca, Cd, Co, Cu, Dy, Er, Eu, Hg, Ho, In, Ir, K, La, Li, Lu, Mg, Mn, Mo, Na, Nb, Ni, Os, Pb, Rb, Re, Ru, Sc, Se, Si, Sn, Sr, Tb, Ti, Tm, V, Y, Yb, Zn, Zr
< 20	Au, Ga, Ge, Hf, Pr, Rh, Sm, Tl
< 30	Bi, Nd, P, Pd, Pt
< 40	W
< 50	Ce
50-100	S
> 100	None detected

Table 4.1. Chemical impurity analysis through mass spectroscopy. Chemical impurity analysis using inductively-coupled plasma optical emission spectrometry performed on $FeSb_2$ samples from the same growth batches as those used in the quantum oscillation measurements. Pristine sample quality is indicated, with no impurities detected above 100 parts per million.

Magnetic susceptibility measurements

Magnetic susceptibility measurements shown in Figure 4.3 were taken at 1.8 K with magnetic field oriented along the [001] direction. Additional magnetisation measurements,

taken as functions of both field and temperature for various magnetic field alignments, are discussed later in section 5.6.1.

The sample magnetisation as a function of applied magnetic field was fitted with a Langevin function to approximate the level of magnetic impurity content. The magnetisation per mole was fitted by:

$$M(H,T) = \chi_{\text{bulk}} H + c_{\text{impurity}} \mu_{\text{eff}} \left(\coth\left(\frac{\mu_{\text{eff}} H}{k_{\text{B}} T} \right) - \frac{k_{\text{B}} T}{\mu_{\text{eff}} H} \right), \tag{4.1}$$

where χ_{bulk} is the intrinsic bulk susceptibility, H is the applied magnetic field strength, c_{impurity} is the impurity concentration, k_{B} is the Boltzmann constant, and T is temperature [166]. The effective magnetic moment, μ_{eff}, was set as a free parameter in the fit, and yielded a value of 5.4(3) μ_{B}. The fit limits any magnetic impurity content to 60(20) parts per million.

Specific heat capacity

The specific heat capacity of a single crystal of $FeSb_2$ was measured to high precision at low temperatures on a zero field cooled sample by using the cooling relaxation technique. Heat capacity measurements in zero applied magnetic field reveal a finite Sommerfeld coefficient γ = 0.19(2) mJ mol^{-1} K^{-2} at the lowest measured temperature of 0.75(5) K (Fig. 4.3). These measurements were performed in collaboration with S. Yamashita of Osaka University.

Raman spectroscopy

A complementary study of sample purity was performed by measuring the Raman spectra of our $FeSb_2$ single crystals and making a comparison with elemental Sb. Raman scattering was excited by a HeNe laser operating at 632.8 nm, appropriately filtered to suppress the plasma line. Measurements were conducted at both room temperature and

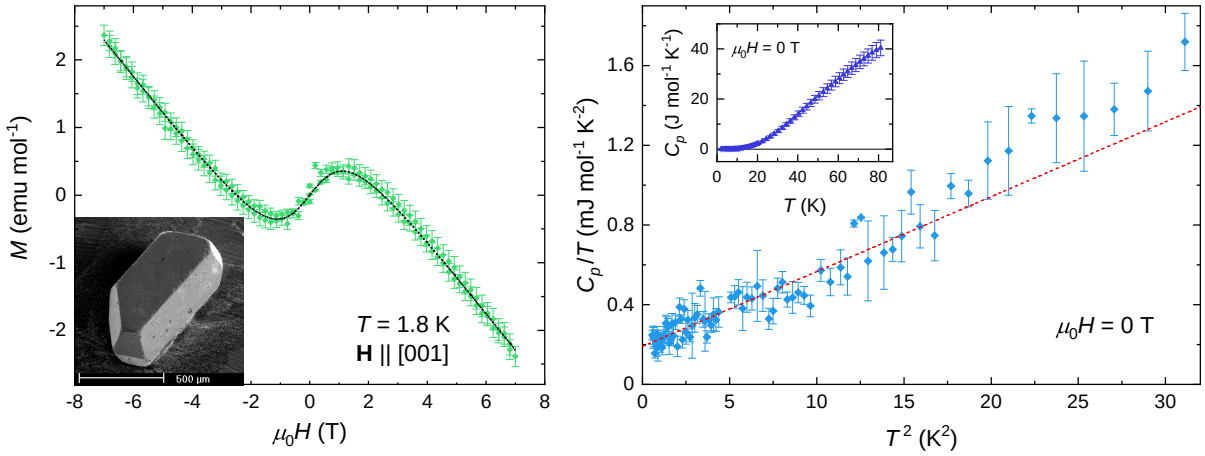

Fig. 4.3. Magnetisation and specific heat of single crystal $FeSb_2$. *Left:* Magnetisation of an $FeSb_2$ crystal measured in a Quantum Design MPMS at 1.8 K. The black dashed line is a fit to eqn. 4.1. Magnetic field was applied along the [001] crystallographic direction. A small paramagnetic component at low field is observed, due to the presence of a small quantity of magnetic impurities. These moments are quickly saturated, with the bulk (diamagnetic) response of the sample dominating for higher fields. *Inset:* An as-grown $FeSb_2$ specimen grown via the CVT method, imaged using a scanning electron microscope. *Right:* Specific heat divided by temperature versus squared temperature. A linear fit to the low-temperature region yields a value of the Sommerfeld coefficient (γ) as 0.19(2) mJ mol^{-1} K^{-2}. *Inset:* Specific heat of a different $FeSb_2$ crystal measured up to 80 K. Error bars in all plots are the standard deviation from computing the mean of multiple measurements.

at 4 K, with the sample thermally bonded to a coldfinger cryostat. Up to 3.0 mW was focused onto the sample via an Olympus 50x long-working-distance 0.5 NA objective. The objective also collected the Raman scattered light, which was analyzed by a Jobin-Yvon T64000 spectrometer operating in subtractive mode.

Raman peaks for the six vibrational modes allowed by selection rules are seen and in good agreement with DFT simulations of $FeSb_2$ [167], with no extraneous peaks observed. These measurements were performed in collaboration with R. Phillips of the Cavendish Laboratory.

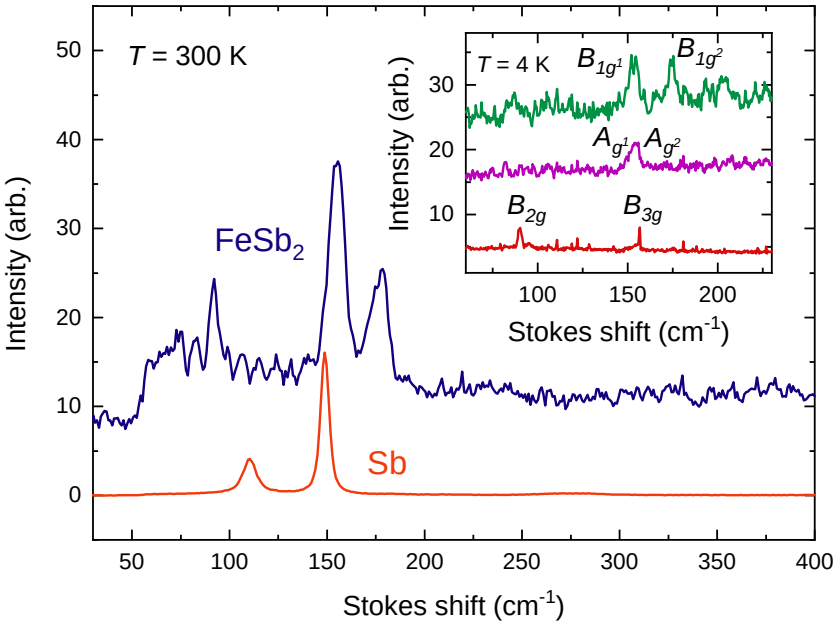

Fig. 4.4. Raman spectra of single crystalline $FeSb_2$. Raman spectra of a single crystal of $FeSb_2$ (blue) and elemental Sb (orange) taken at 300 K, both of which were excited and measured normal to the (110) face. No contribution from elemental Sb can be resolved in the $FeSb_2$ Raman spectrum. (Inset) Raman spectra of the same $FeSb_2$ sample obtained at T = 4 K; the green spectrum was excited and measured normal to the (110) surface, the purple spectrum was excited and measured along the [001] direction, and the red spectrum was excited along [001] and measured normal to the (110) face. The six allowed vibrational modes, B_{1g^1}, B_{1g^2}, B_{2g}, B_{3g}, A_{g^1}, and A_{g^2}, corresponding to $FeSb_2$, are marked. Raman peaks for all six vibrational modes allowed by selection rules are observed and in good agreement with DFT simulations [167].

Summary of sample characterisation and purity analyses

Here we summarise results of characterisation methods that we use to establish the bulk intrinsic character of quantum oscillations in insulating $FeSb_2$. Mass spectroscopy on crystals from the same batch as those used in high field measurements observed an overall impurity content upper bound of 100 ppm. A Langevin fit to the measured magnetic susceptibility, which is sensitive to magnetic impurities and lone spin contributions, lim-

its extrinsic magnetic content to 60(20) ppm. Energy-dispersive x-ray diffraction, which probes spatial variations in elemental content, resolved no elemental Sb nor other impurity content. Powder x-ray diffraction further confirms the crystallographic phase of $FeSb_2$ and rules out elemental Sb and other impurity inclusion to < 0.5%at. Hence, we can conclude that the $FeSb_2$ samples examined in this study are of excellent quality.

4.1.3 SmB_6 sample preparation

In a number of places in chapters 6 & 7, comparisons are drawn between the electrical behaviour of $FeSb_2$ and that of the Kondo insulator SmB_6. All measurements presented on SmB_6 were performed on samples grown by M. Ciomaga Hatnean of the Balakrishnan group, University of Warwick.

Single crystal specimens of SmB_6 were prepared by the floating zone method in an image furnace using 99.9% purity SmB_6 powder [168]. Grown boules were aligned with a Laue x-ray diffractometer, then cut into rectangular cuboidal samples, with two dominant (top and bottom) surfaces, using 25 μm tungsten wire in an abrasive solution of small diamond fragments suspended in glycerol. Samples were then electropolished in dilute perchloric acid to remove strain damage from cutting as per the procedure given in ref. [169], resulting in pristine surfaces.

4.2 Measurement techniques in high magnetic fields

Data presented in this dissertation, collected at low temperatures to applied magnetic field strengths limited to ≤ 14 T, were measured using the Advanced Materials Characterisation Suite at the Maxwell Centre, University of Cambridge, using Quantum Design Ltd Physical Properties Measurement Systems (PPMSs) for electrical measurements and Magnetic Properties Measurement Systems (MPMSs) for magnetic measurements.

All measurements presented in this thesis to applied magnetic field strengths > 14 T

were performed at high magnetic field facilities. These include the dc magnetic field facilities The National High Magnetic Field Laboratory, Tallahassee, Florida, USA, and the High Field Magnet Laboratory, Radboud University, Nijmegen, The Netherlands. Pulsed field measurements were undertaken at the Hochfeldlabor, HZDR, Rossendorf, Dresden, Germany, and at the International MegaGauss Science Laboratory, Institute for Solid State Physics, University of Tokyo, Tokyo, Japan. Excellent reviews of high magnetic field facilities are given in, for example, refs. [169–171]; for brevity, this section omits such a review of the engineering aspects of high magnetic field science, focussing instead on the measurement techniques themselves – and on the specific aspects of these experimental methods that are most salient for the interpretation of the data presented in chapters 5, 6 & 7.

4.2.1 Capacitive torque magnetometry

Torque magnetometry measurements presented in chapter 5 were performed in dc magnetic fields of strengths up to 45 T. Cantilevers were laser-cut from a 20 μm thin sheet of non-magnetic BeCu into flexible T-shaped pieces, with narrow tails and wide rectangular heads, a schematic of which is given in Fig. 4.5. After sample mounting, cantilevers were secured at the narrow end so as to have the head suspended above a Cu film, thus forming the two plates of a capacitor. The change in capacitance of this configuration was measured by a General Radio analogue capacitance bridge in conjunction with a phase sensitive detector.

This configuration of cantilever and base plate was mounted on a rotatable housing unit capable of rotating through 2π radians in a plane parallel to that of the applied magnetic field. A Hall probe was affixed to this unit, allowing for accurate determination of the angle between sample orientation and applied magnetic field. Proximity to highly symmetric crystallographic directions was verified by the observation of vanishing torque signals accompanied by a change of sign of the magnetic torque background with increas-

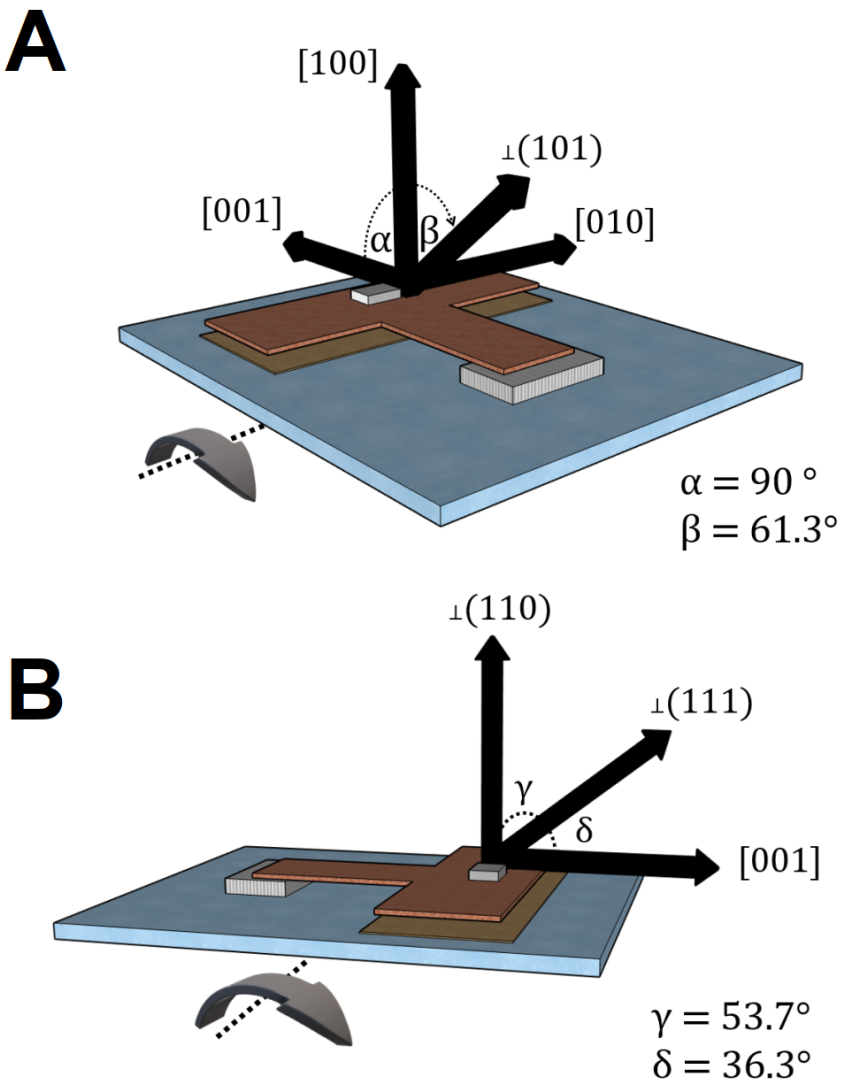

Fig. 4.5. Alignment of single crystal $FeSb_2$ samples with respect to torque cantilever rotation. (**A**) Alignment configuration in the $c-a$ rotation plane, allowing for magnetic field to be applied parallel to the [001] and [100] directions, as well as through the vectors normal to the (101) and $(\bar{1}01)$ planes. The [010] direction is indicated to aid perspective, which is oriented orthogonal to the plane of rotation. The angle β between [100] and the vector normal to the (101) plane is 61.3°, hence the angle between [001] and the vector normal to the $(\bar{1}01)$ plane is 28.7°. (**B**) Alignment configuration in the $c-ab$ rotation plane, allowing for magnetic field to be applied normal to the (110) and (111) planes, as well as along the [001] direction.

ing field on either side of the axis of symmetry.

For the sample presented in Fig. 5.3, which has dimensions of $0.95 \times 1.12 \times 0.57$ mm^3 and a mass of ≈ 1 mg, the total deflection of the cantilever up to the maximum applied magnetic field of $\mu_0 H = 45$ T was $\lesssim 0.01$ radians, small enough to remain well within the elastic limit and to preclude torque interaction effects. Other measured samples have similar dimensions, and smaller deflections, compared to this sample.

4.2.2 Electrical transport measurements

dc magnetic field measurements

Resistance measurements were obtained using a standard 4-terminal technique, with current sourced/drained through the two outermost leads, and the potential difference across a portion of the sample measured by the two (inner) voltage leads. Samples were contacted with Au wires using DuPont 4929N silver epoxy thinned with 2-butoxyethyl acetate to obtain a suitable consistency with low contact resistance ($\sim 1\ \Omega$ at 300K). Some samples were also spot welded, with no discernible differences in results between the two preparation techniques.

At high magnetic field facilities, ac excitations were sourced from Keithley 6000-series current sources, with the potential difference across the sample measured by Stanford 8600-series lock-in amplifiers. For measurements in fields ≤ 14 T performed in Cambridge using a Quantum Design PPMS cryostat, several measurements were performed using the BRT resistivity option sourcing dc excitations. This was utilised due to the sensitivity of surface states to ac excitation frequency as explicated in the overview of the measurement suite presented in chapter 7. For these measurements, voltages were obtained by averaging the absolute value of the potential drop across the sample from positive- and negative-polarity dc excitation currents, thereby eliminating any possible errors from dc offset voltages. dc square waves were sourced at a frequency of 8.33 Hz, with each measurement point being comprised from the average of 25 individual read-

ings.

Measurements of carrier density and mobility in dc fields

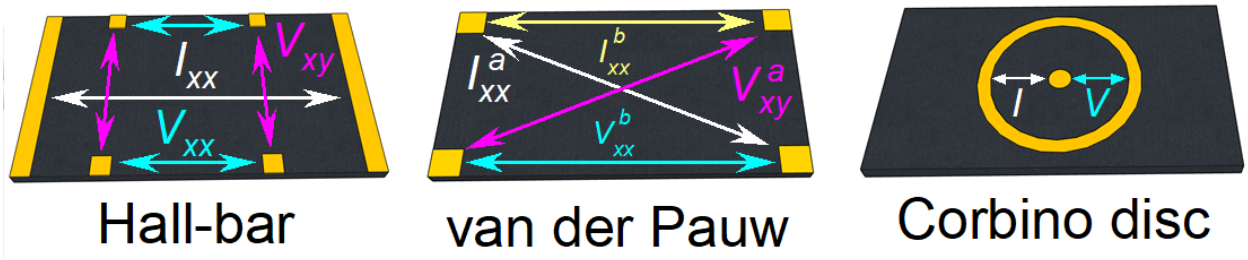

Fig. 4.6. Wiring configurations for extracting transverse magnetoresistivity components. The respective geometries for Hall-bar, van der Pauw (vdP) and Corbino disc measurements. xx subscripts refer to the longitudinal component, while xy denotes the transverse component that is of interest when performing Hall measurements.

Hall effect measurements were performed using Hall-bar and van der Pauw (vdP) geometries (Fig. 4.6). Quantitative values for the carrier density, n, and carrier mobility, μ, can be extracted from the transverse voltage, V_{xy}, in an applied magnetic field, of strength $\mu_0 H$, assuming the domination of one species of charge carrier. We can write the Hall coefficient, R_{H}, as

$$R_{\mathrm{H}} = \frac{tV_{xy}}{\mu_0 HI} = \frac{1}{nq}, \tag{4.2}$$

where t is the sample thickness (perpendicular to the xy plane), I is the magnitude of the current, and q is the negative (positive) elemental charge for electrons (holes) [172]. Hence, n is easily obtained.

We can reconsider R_{H} in terms of μ, by writing $R_{\mathrm{H}} = \rho\mu$, where ρ is the resistivity of the material [172]. Thus,

$$n = \frac{qtV_{xy}}{\mu_0 HI}, \qquad \mu = \frac{tV_{xy}}{\mu_0 HI\rho}. \tag{4.3}$$

Measurements of n and μ were also performed using the Corbino geometry [173] (Fig. 4.6). In the case of Corbino disc measurements, current is sourced between an inner circle (of radius r_{in}) and a concentric annulus (where the inner part of the annulus is a distance r_{out} from the centre of the inner circle). Under the application of a magnetic field out of the plane of the disc, the charge carriers perform cyclotron orbits, thereby modifying the observed resistance of the disc.

Assuming that the observed resistance of the Corbino disc will be dominated by a 2D metallic surface state, we may write the two-terminal resistance of the disc, R_{Corbino}, as

$$R_{\text{Corbino}} = \frac{1}{2\pi\sigma_s} \ln \frac{r_{out}}{r_{in}}, \tag{4.4}$$

where σ_s is the surface conductivity [174]. Thus, in a magnetic field, $\mathbf{B}$, oriented at angle α out of the plane of the disc, for elementary charge e, we observe

$$R_{\text{Corbino}}(B) = \frac{\ln \frac{r_{out}}{r_{in}}}{2\pi} \frac{1 + (\mu B \sin(\alpha))^2}{ne\mu}. \tag{4.5}$$

Therefore, for a given α we find the carrier concentration to be described by

$$n = \frac{\ln \frac{r_{out}}{r_{in}}}{2\pi} \frac{1 + (\mu B \sin(\alpha))^2}{R_{\text{Corbino}} e\mu}. \tag{4.6}$$

We can thus eliminate the dependence of R_{Corbino} on n by taking a ratio at two different values of α, by considering

$$\frac{R_\alpha}{R_\parallel} = 1 + (\mu B \sin(\alpha))^2, \tag{4.7}$$

where $R_\parallel$ denotes $\alpha = 0°$ [175].

Hence, we can extract a value for μ as

$$\mu = \frac{1}{B \sin(\alpha)} \sqrt{\frac{R_\alpha}{R_\parallel} - 1}, \tag{4.8}$$

whereupon substitution for μ back into eqn. 4.6 yields n.

Pulsed magnetic field measurements

To measure electrical transport measurements in pulsed magnetic fields, the general principle of the four-probe method still applies. However, due to the short timescale over which pulsed magnets operate, high frequency excitations are required (typically up to 100 kHz), which mandate a high sampling rate by the measurement electronics in order to achieve suitable resolution of the measurement. For measurements presented in this dissertation performed at the International MegaGauss Science Laboratory of the Institute for Solid State Physics at the University of Tokyo, digital acquisition was performed with a National Instruments PXIe-6124 system. For measurements performed at Hochfeldlabor, HZDR, Dresden, digital acquisition was performed with a Yokogawa DL 850E with 701251 - HS1M16 cards.

5

Insulating metamagnetism and the dHvA effect in the unconventional insulator $FeSb_2$

For however many things have a plurality of parts and are not merely a complete aggregate, but instead some kind of a whole beyond its parts, there is some cause of it since even in bodies, for some the fact that there is contact is the cause of a unity or oneness, while for others there is viscosity or some other characteristic of this sort.

– Aristotle

We can now see that the whole becomes not merely more, but very different from the sum of its parts.

– Philip W. Anderson

5.1 Introduction

The possession of a Fermi surface is, conventionally, one of the defining characteristics of a metal [14, 18]. As discussed in chapter 1, a material that has the Fermi energy located within a band of allowed energy levels enables low-energy excitations to be easily accommodated, hence metals are excellent thermal and electrical conductors. Conversely, band insulators are characterised by a charge gap wherein the Fermi energy lies outside any available bands – hence they are poor thermal and electrical conductors, and do not possess a Fermi surface.

As discussed in chapter 3, SmB_6 was the first unconventional insulator to defy these conventional assumptions, manifesting evidence of a Fermi surface through observations of the dHvA effect despite exhibiting robustly insulating electrical resistivity up to the high magnetic field strengths at which quantum oscillations were observed [19]. In the time since this original discovery, a number of other unconventional insulator candidates have been reported [22–25], prompting a multitude of theoretical speculation with respect to the novel microscopic mechanism(s) that may be at play [113–153].

In this chapter, I shall detail my findings pertaining to quantum oscillations in the magnetisation of $FeSb_2$ [44]. A quantitative analysis of the oscillation amplitude reveals that, remarkably, they are shown to a very high level of confidence to emanate from the insulating bulk, rather than from a metallic surface state or from any extrinsic impurity origin. Three regimes of starkly contrasting insulating behaviour are identified, with each explored in turn.

Notably, unlike other unconventional insulators reported to date, the unconventional quantum oscillatory profile in $FeSb_2$ is found to be closely related to changes in the bulk magnetisation of the material. At low fields, a pronounced enhancement in the growth of the magnetic torque signal is accompanied by a concomitant enhancement in both the quantum oscillatory amplitude and frequency. Then, at the highest fields, a sharp metamagnetic transition abruptly quenches the insulating quantum oscillations – in marked contrast to numerous tunnelling and magnetic-breakdown posited models of unconven-

tional insulating behaviour. These findings point strongly to strong spin-orbit interaction effects being responsible for the manifestation of this paradoxical phenomenon.

The chapter concludes with a comparison of anomalous features in the isotropic magnetisation, and the discussion of a minimal magnetic model that can qualitatively capture the most salient features of the anomalous magnetic torque profile of $FeSb_2$.

5.2 de Haas-van Alphen effect within the insulating bulk of $FeSb_2$

5.2.1 Magnetic torque profile

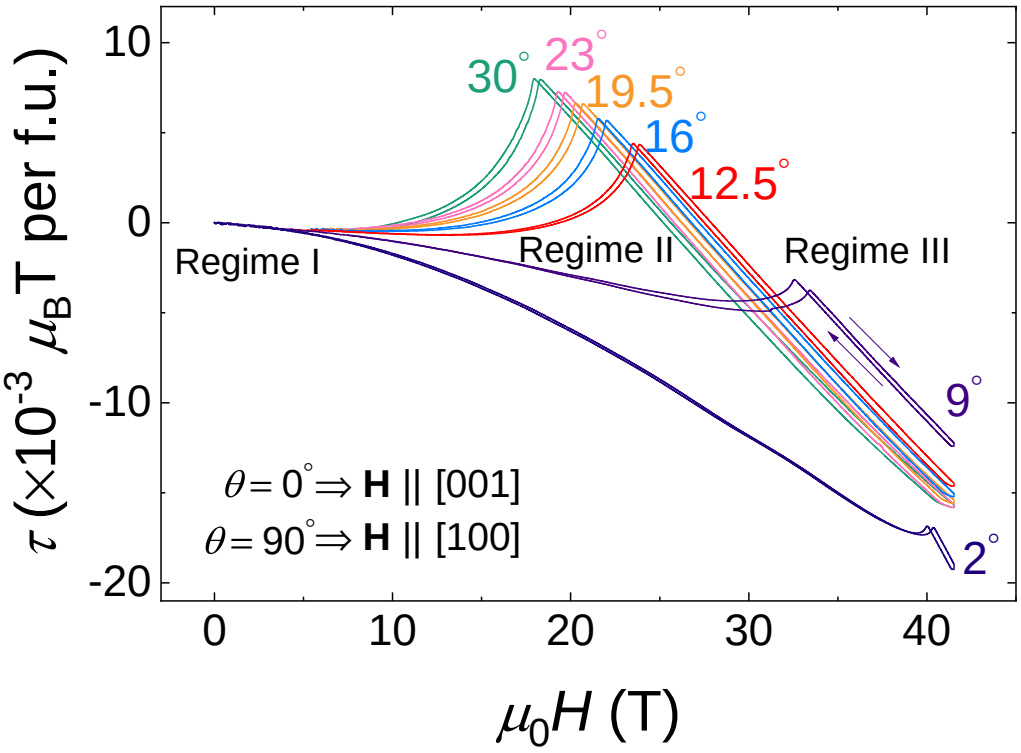

Fig. 5.1. Angular evolution of magnetic torque profile of $FeSb_2$ in the $c-a$ rotation plane. Magnetic torque, τ, measured up to $\mu_0 H$ = 41.5 T at various values of magnetic field tilt angle θ on a single crystal specimen of $FeSb_2$. We identify three regimes of contrasting magnetic torque behaviour. At low fields, the magnetic torque is quadratic in magnetic field (Regime I), before showing a steep exponential upturn (Regime II) on the rising side of a peak. Finally, at yet higher fields, τ decreases linearly on the falling side of the peak upon evolution to Regime III. Arrows indicate the direction in which the field was swept, with a small hysteresis observed at each angle.

Figure 5.1 shows the magnetic torque, τ, of $FeSb_2$ measured by the capacitive torque magnetometry technique as a function of magnetic field strength, $\mu_0 H$, for various magnetic field tilt angles. As the sample is rotated away from $\mathbf{H} \parallel [001]$ (corresponding to 0°) towards $\mathbf{H} \parallel [100]$ (corresponding to 90°), a strong, clear angular dependence of the torque profile is apparent.

We identify three regimes of sharply contrasting magnetic behaviour of $FeSb_2$ in the torque curves presented in Fig. 5.1. Firstly, at low fields, we find that the torque is proportional to the square of the magnetic field strength, which is the usual case for simple paramagnetic materials. As magnetic torque is the vector cross product of a sample's magnetisation with the magnetic field, a quadratic torque profile is characteristic of typical paramagnets, for which the magnetisation is linear in magnetic field [166]. We identify the (low) range of applied magnetic field strengths that induce a quadratic magnetic torque response as Regime I.

Strikingly, we find that as the magnetic field strength is subsequently increased, the magnetic torque grows rapidly, showing a prominent deviation from a quadratic dependence on applied magnetic field strength, and instead exhibits a steep exponential upturn constituting the rising side of a peak – we refer to this as Regime II. Then, on the falling side of this sharp peak observed in magnetic torque, a linear decrease in magnetic torque with increasing magnetic field is observed up to even higher field strengths – we refer to this as Regime III.

5.2.2 Characterisation of the three insulating regimes

Regime I to Regime II

To investigate the nature of the crossover from Regime I to Regime II, we must pay careful attention to the slope of τ. Figure 5.2 shows the derivative of the $\theta = 2°$ curve from Fig. 5.1 with respect to applied magnetic field strength. At low fields, a derivative linear in magnetic torque is observed, thus characterising Regime I. However, above 30 T the deriva-

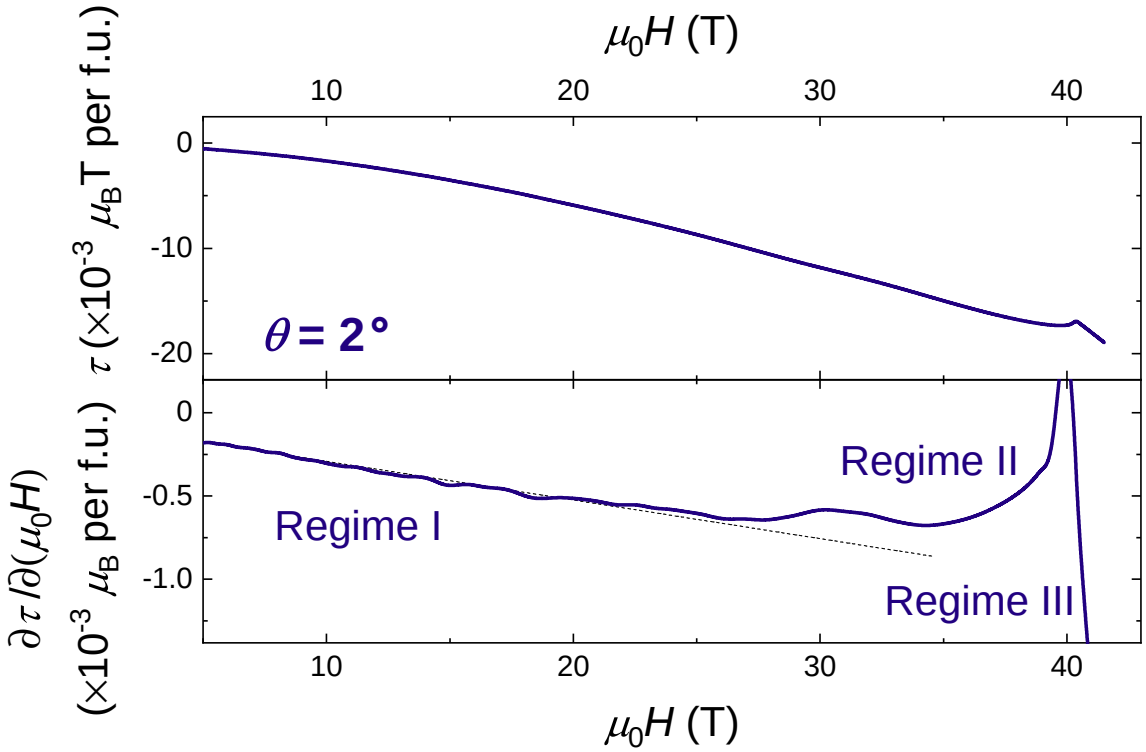

Fig. 5.2. Quantum oscillations in quadratic magnetic field-dependent magnetic torque (Regime I). *Top:* Magnetic torque, τ, for field oriented at $\theta = 2°$ away from the [001] direction in the $c - a$ rotation plane, is largely dominated by Regime I, characterised by quadratic magnetic field-dependence. *Bottom:* Derivative of the magnetic torque curve in the top panel with respect to magnetic field strength shows slow quantum oscillations in Regime I. The dashed line shows the range of magnetic field strength over which the derivative is linear, indicating the extent of Regime I. Beyond this regime, a steep exponential upturn in magnetic field (Regime II) is observed, constituting the rising side of a metamagnetic insulator – to – insulator peak, the falling side of which constitutes Regime III.

tive is clearly no longer linear – thereby indicating the occurrence of the crossover from Regime I to Regime II. Furthermore, a clear oscillatory profile is present in the derivative of τ with respect to $\mu_0 H$, the amplitude of which clearly grows with increasing H upon

entering Regime II. As we shall see over the coming pages, these oscillations are periodic in inverse magnetic field strength, indicating the presence of Landau quantisation – despite $FeSb_2$ remaining robustly insulating up to magnetic field strengths at least as high as 70 T. Thus, $FeSb_2$ is found to be a new member of the family of unconventional insulators.

To further examine the evolution between Regime I and Regime II, in Figure 5.3 magnetic torque at an angle $\phi = 16^\circ$ from $\mathbf{H} \parallel [001]$ in the $c - ab$ rotation plane is plotted[1]. In this rotation plane, unlike the $c - a$ plane (presented in Fig. 5.1) the transition between Regime II and Regime III is not observed up to the highest attainable laboratory dc magnetic field strength of 45 T. This gives a large magnetic field range over which to examine Regime II in detail.

Fig. 5.3A shows the departure from $\tau \propto H^2$, that is characteristic of Regime I, which occurs around $\mu_0 H \approx 25$ T. In panel B, the background magnetic torque has been removed by subtracting a smooth monotonic polynomial fit by the local regression technique [176], to isolate the oscillatory component $\Delta\tau$. Similar to Fig. 5.2, a clear oscillatory component in the magnetic torque of $FeSb_2$ is resolved. Remarkably, the magnetoresistance of this material remains robustly insulating up to the highest accessed magnetic field strength of 45 T – despite the presence of large amplitude, high frequency magnetic quantum oscillations characteristic of the dHvA effect (Fig. 5.3B). As we will see in Fig. 7.8, resistivity measurements to even higher magnetic fields using pulsed magnets reveal no significant closing of the charge gap up to at least 70 T.

The evolution from Regime I to Regime II – characterised by the change in τ from a quadratic dependence on H to an exponential growth in H – also sees marked changes in the quantum oscillations. At low fields, in Regime I, the quantum oscillations are small in amplitude, with low frequencies of a few hundred Teslas. Strikingly, at the highest fields, the frequency and amplitude of the quantum oscillations grows markedly, extending to frequency components up to ≈ 9 kT; this corresponds to quasiparticle orbits with an associated Fermi wavevector spanning an area of $\approx 20\%$ of the first Brillouin zone.

[1]Throughout this chapter, we shall always refer to the angle away from $\mathbf{H} \parallel [001]$ towards $\mathbf{H} \parallel [100]$ as θ, and the angle away from $\mathbf{H} \parallel [001]$ towards $\mathbf{H} \perp (110)$ as ϕ. Further details of these rotation planes were given in section 4.2.1.

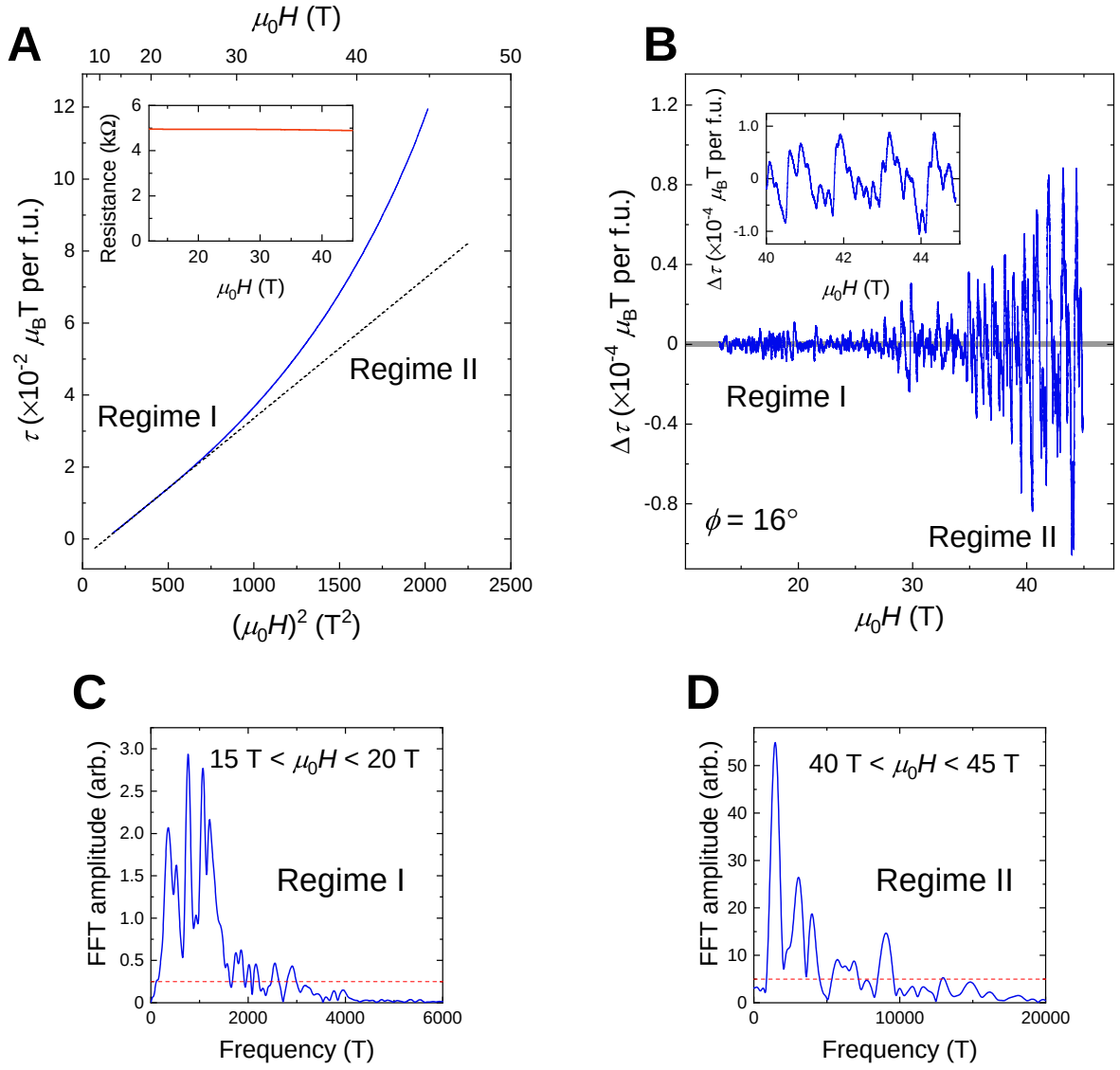

Fig. 5.3. High frequency high field quantum oscillatory spectra measured in the $c-ab$ rotation plane. (**A**) Magnetic torque plotted against squared magnetic field strength. The dashed line is a linear fit to the low-field data, to highlight the departure from conventional paramagnetic (quadratic) behaviour, which indicates the transition from Regime I to Regime II.

Fig. 5.3. (cont.) The sample was oriented with magnetic field applied 16° from the [001] direction in the $ab - c$ rotation plane, and measured at 0.4 K. *Inset:* Measured electrical resistance at the same angle and temperature as the main panel with an applied current of 10 μA along the [100] direction; the electrical resistance shows no obvious change upon the transition from Regime I to Regime II. (**B**) Oscillatory component of the torque in **A** ($\Delta\tau$), showing a clear enhancement in quantum oscillation amplitude upon the transition from Regime I to Regime II. The grey line indicates the noise floor of the measurement. $\Delta\tau$ was isolated by subtracting the background signal using the local regression technique [176]. *Inset:* Highest magnetic field range of the main panel, wherein high frequency components are clearly visible. (**C**) Fast Fourier transform (FFT) of low frequency quantum oscillations in Regime I and (**D**) of much higher frequencies in Regime II. Regime II exhibits a rich quantum oscillatory frequency spectrum, up to at least ≈ 9 kT. Red dashed line indicates the FFT noise floor.

Throughout this investigation, eight separate samples have been measured at high magnetic field facilities, as tabulated in Table 5.1. There is a clear correlation between sample purity - as determined by iRRR measurements - and the resulting quality of the quantum oscillatory spectra attained. These samples were selected from 74 single crystals, from eight separate growth batches, that were screened for iRRR.

The growth in amplitude of quantum oscillations with increasing magnetic field strength is typical of quantum oscillations in metals, due to the impurity (Dingle) damping arguments discussed in section 2.2.1. However, we find that the growth in quantum oscillatory amplitude of the insulating quantum oscillations in $FeSb_2$, upon transitioning from Regime I to Regime II, is markedly more pronounced than expected for Dingle damping. Figure 5.4 shows τ and $\Delta\tau$ at $\phi = 21°$, at which angle the beat pattern structure present at $\mu_0 H \approx 30$ T in Fig. 5.3B is much less pronounced. The right panel of Fig. 5.4 shows a simulation of Dingle damping, by plotting grey dashed lines fitted to the amplitude of the Regime I quantum oscillations, to the form $\exp(-B_D/\mu_0 H)$ as per eqn. 2.7. Remarkably, the growth in quantum oscillatory amplitude upon the evolution to Regime II is almost an order of magnitude greater than that expected for Dingle damping [18, 82]. This correspondence between changes in the background (bulk) magnetic torque and the concomitant evolution in the quantum oscillatory profile strongly suggests a link between

$FeSb_2$ Sample Number	Inverse residual resistivity ratio (iRRR) $R(T = 2\text{ K}) / R(T = 300\text{ K})$	Highest observed quantum oscillation frequency (kT)	Maximum applied magnetic field (T)
S1	2,410,000	9	41
S2	5,510,000	9	41
S3	2,950,000	9	45
S4	974,000	4	38
S5	862,000	4	38
S6	692,000	2	35
S7	366,000	2	35
S8	238,000	2	35

Table 5.1. List of iRRR and maximum observed quantum oscillation frequency for all measured samples of $FeSb_2$. Eight samples of CVT-grown $FeSb_2$ were measured to high magnetic fields, each of which exhibited quantum oscillations in the magnetic torque. A clear correspondence between sample quality (indicated by the value of the inverse residual resistivity ratio (iRRR)) and the richness of the quantum oscillation frequency spectrum is apparent. This chapter focusses on quantum oscillations measured on the highest purity samples that offer the best insight into the nature of the unconventional insulating behaviour in $FeSb_2$. Electrical resistance measurements were performed with a low applied current aligned along the [100] direction.

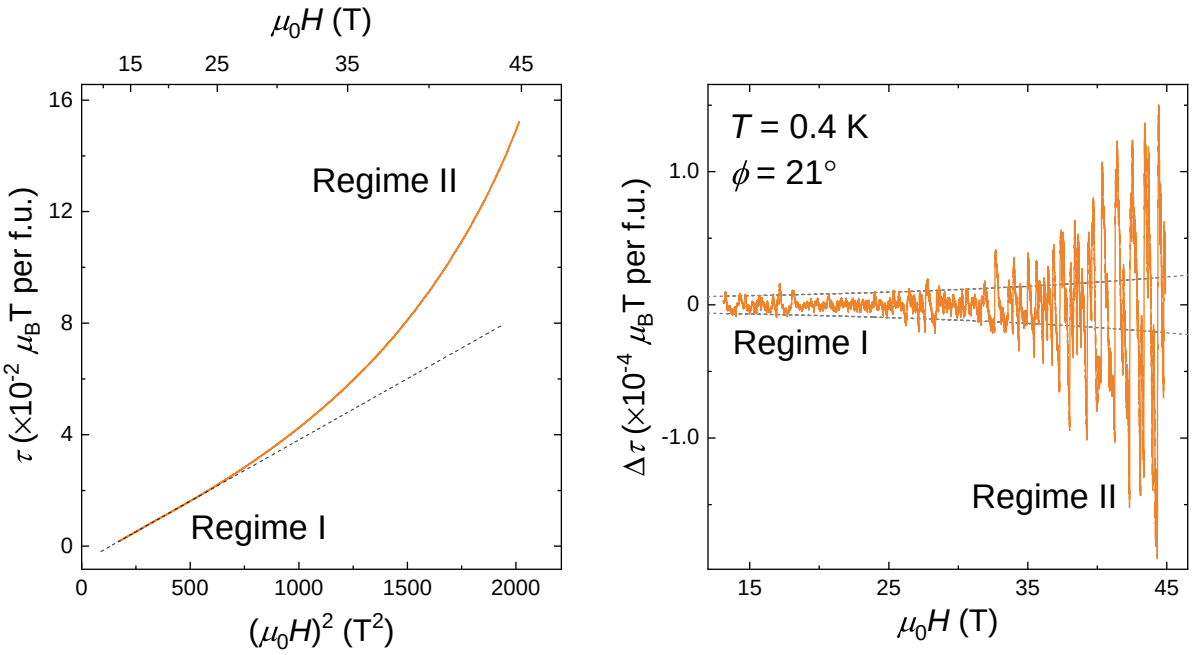

Fig. 5.4. Dramatic enhancement of quantum oscillations from Regime I to Regime II at a different tilt angle. *Left:* Magnetic torque as a function of the square of the magnetic field strength. The sample was oriented with magnetic field applied at $\phi = 21°$ from the [001] direction in the $c - ab$ rotation plane, and measured at 0.4 K. Again, the magnetic torque shows a striking departure from the low field quadratic magnetic field dependence (dashed line) with increasing magnetic field, evolving to a steep exponential upturn in magnetic field upon entering Regime II. *Right:* Background subtracted quantum oscillations in magnetic torque from the left panel show a dramatic enhancement in amplitude upon entering Regime II. Here, the grey dashed lines simulate the expected Dingle growth of Regime I quantum oscillations with increasing magnetic field strength [18].

the magnetic properties of $FeSb_2$ and the origin of unconventional insulating quantum oscillations.

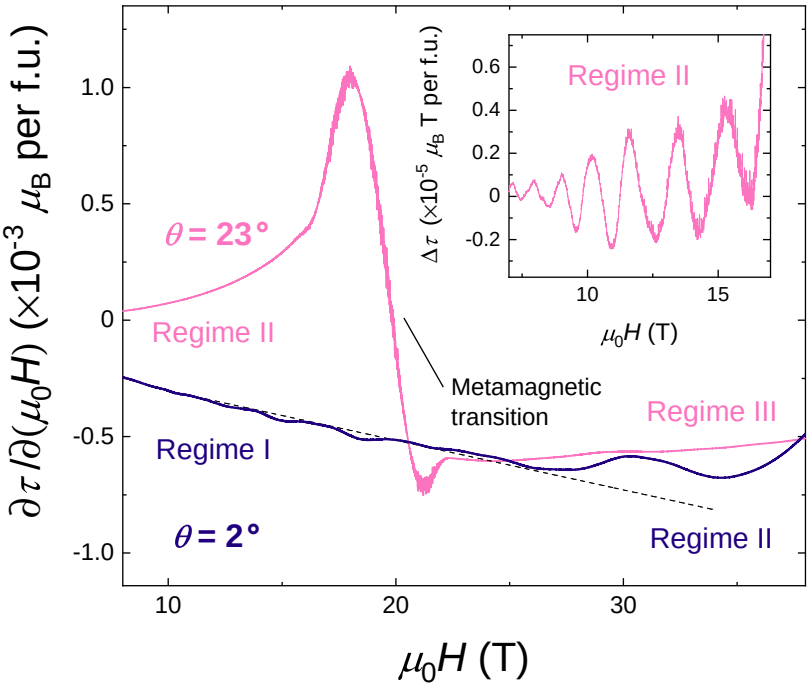

Fig. 5.5. Transitions between regimes. Derivatives of the torque curves at 2° and 23° in the $a-c$ rotation plane. A metamagnetic transition between Regimes II & III is clearly visible in the $\theta = 23°$ data where $\frac{\partial\tau}{\partial(\mu_0 H)}$ suddenly changes sign. *Inset:* The oscillatory component of τ in Regime II of the $\theta = 23°$ curve, just before the metamagnetic transition.

Regime II to Regime III

Returning to the $c-a$ plane, at the highest accessed fields we observe another regime of magnetic behaviour that is starkly different to both Regime I and Regime II. Figure 5.5 shows the derivative of τ at $\theta = 23°$, along with the $\theta = 2°$ curve again for comparison. At $\mu_0 H \approx 20$ T, the sign of $\frac{\partial\tau}{\partial(\mu_0 H)}$ of the 23° curve abruptly changes sign, signalling the occurrence of a metamagnetic transition. The inset shows $\Delta\tau$ of the 23° data, in which quantum oscillations are resolved down to ≈ 10 T.

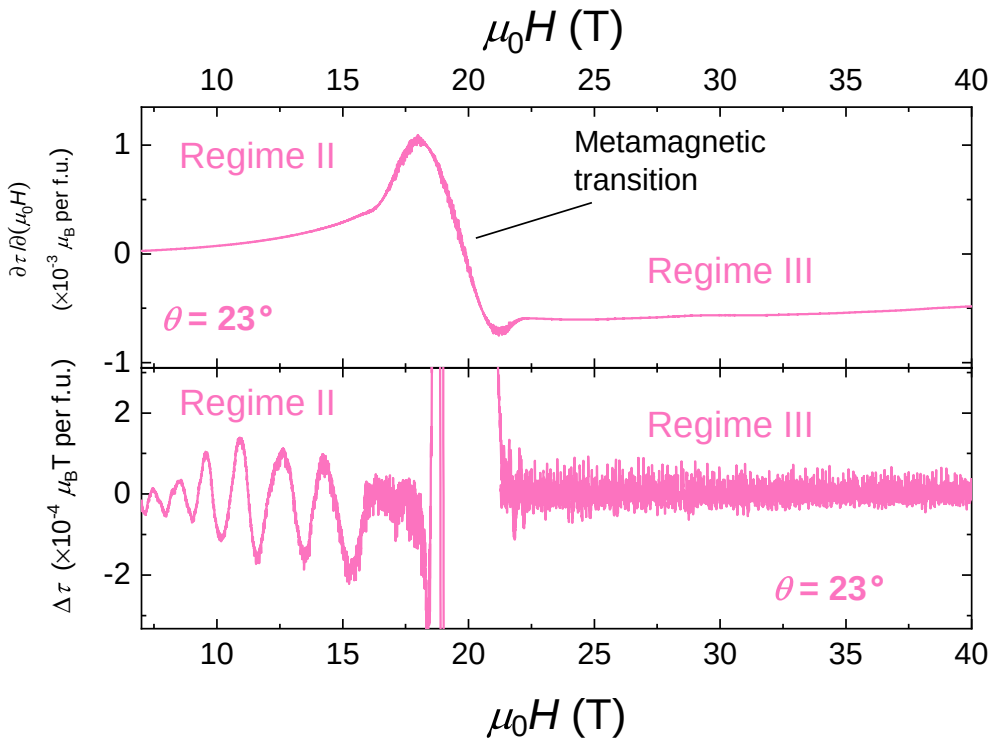

Fig. 5.6. Abrupt quenching of quantum oscillations at the high field metamagnetic transition. *Top:* Derivative of τ at $\theta = 23°$; this is the same data as in Fig. 5.5 duplicated here for ease of comparison. *Bottom:* Oscillatory component of the same torque curve as the top panel, plotted over the identical field range. The subtracted τ signal has been multiplied by an exponential function to simulate the removal of the Dingle damping component [18, 82], which should give the quantum oscillation amplitude in the infinite field limit – however, it is clear that the oscillatory amplitude increases faster than conventional Dingle growth. In Regime II, prominent quantum oscillations are clearly resolved; however, following the metamagnetic transition into Regime III they are strikingly absent.

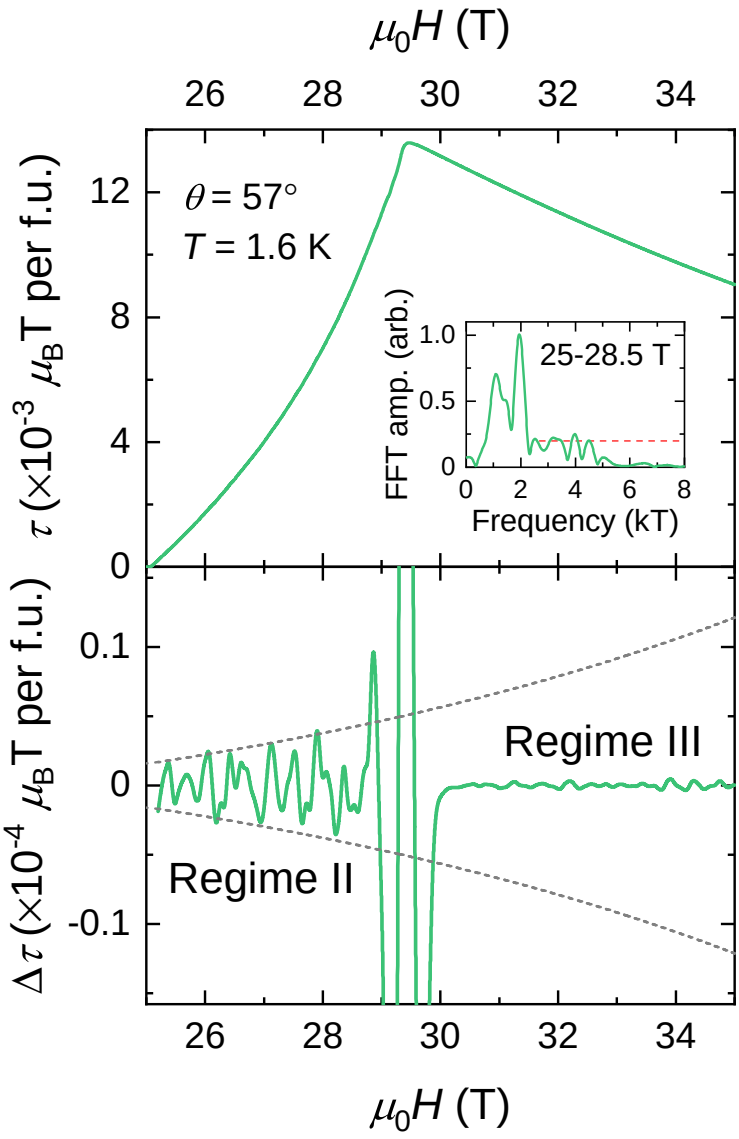

Fig. 5.7. Quenched quantum oscillations upon crossing the metamagnetic insulator–to–insulator transition from Regime II to Regime III. *Top:* Measurement of the metamagnetic transition between Regime II and Regime III measured on a different sample to that of Fig. 5.6. For magnetic field applied at 57° from the [001] direction in the $c - a$ rotation plane, a sharp metamagnetic insulator–to–insulator peak in magnetic torque occurs at magnetic fields $\approx$ 30 T. *Bottom:* Background-subtracted magnetic torque from the top panel reveals the clear presence of quantum oscillations over the magnetic field range 25.0 T $< \mu_0 H <$ 28.5 T in Regime II.

Fig. 5.7. (cont.) Grey dashed lines show the expected Regime II quantum oscillation amplitude extrapolated with increasing magnetic field according to exponential Dingle growth [18, 82]. Upon the transition to Regime III, quantum oscillations are abruptly quenched by at least an order of magnitude below the expectation from Regime II, and are no longer resolvable within the noise level of the measurement.

In Figure 5.6 $\Delta\tau$ has been multiplied by an exponential function (with the exponent inversely proportional to H), which for conventional quantum oscillations would effectively remove the Dingle damping term (eqn. 2.7) and thus yield the oscillation amplitude in the infinite-field limit over the entire field range [18, 82]. However, this treatment does not work here, as upon varying the Dingle damping factor the amplitude of the higher field oscillations starts decreasing before the amplitude of the lower field oscillations has grown to match them. Hence, as per Fig. 5.4, the growth of quantum oscillatory amplitude is found to occur faster than expected for the effect of Dingle damping.

In Regime II, prominent quantum oscillations are clearly visible down to $\mu_0 H < 10$ T. However, strikingly, after going through the metamagnetic transition into Regime III they are abruptly quenched, with no quantum oscillations observed up to the highest applied magnetic field strength of this measurement, of 41.5 T.

Figure 5.7 shows the metamagnetic insulator–to–insulator transition between Regime II and Regime III at $\theta = 56°$, at which this transition is pushed to higher field (occurring at $\mu_0 H \approx 30$ T), thus affording more magnetic field range to Regime II allowing for the unconventional insulating quantum oscillations to have developed to considerably higher amplitudes and frequencies than in the case of $\theta = 23°$.

As per Fig. 5.4, we again plot an extrapolation to higher fields of the growth in quantum oscillatory amplitude expected for Dingle damping by the LK formula. However, again we strikingly see that upon transitioning into Regime III the quantum oscillatory amplitude is abruptly quenched by at least an order of magnitude below the expectation from Regime II, and quantum oscillations are no longer resolvable within the noise level of the measurement.

5.3 Angular magnetic field phase diagram of $FeSb_2$

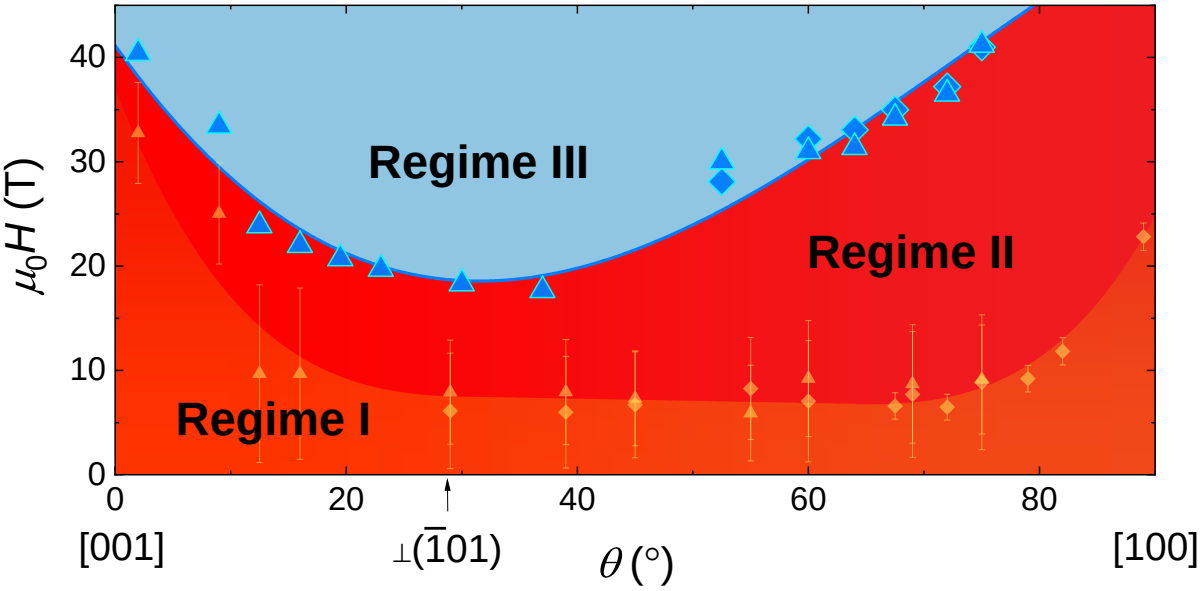

Fig. 5.8. Magnetic phase diagram of $FeSb_2$. The three regimes of magnetic behaviour of $FeSb_2$ mapped as a function of applied magnetic field strength ($\mu_0 H$) at successive tilt angles θ in the $c-a$ rotation plane. At all angles, the low field behaviour is characteristic of a nonmagnetic insulator (Regime I). Then, at higher fields, an unconventional insulating phase is uncovered (Regime II), which we find to host large amplitude, high frequency quantum oscillations – despite the presence of a robust charge gap. Furthermore, at yet higher fields a metamagnetic transition occurs, demarcating Regime II from Regime III, in which we find that the unconventional quantum oscillations are abruptly quenched. The high symmetry direction normal to the $(\bar{1}01)$ plane is identified, at which the transition from Regime II to Regime III appears to reach a minimum magnetic field strength.

Figure 5.8 combines several of the measurements presented in this chapter into a magnetic phase diagram of $FeSb_2$ for magnetic field applied in the $c-a$ rotation plane. Yellow symbols denote the crossover from Regime I to Regime II, with blue symbols showing

the metamagnetic transition from Regime II to Regime III. Triangles and diamonds represent data from two different samples, both of which were measured to 41.5 T. The yellow points were gathered on both samples in a high field resistive magnet in Tallahassee and in a 14 T Quantum Design PPMS in Cambridge; their error bars denote the range over which the data can be fit to the form $\tau(H) = aH^2 + b\exp(cH)$, propagating the residual error in the fit coefficients, and finding the extent of the $3a$ deviation (thus indicating the dominance of the exponential term as Regime II is entered). It is due to this acute sensitivity – of the background magnetic torque profile to the applied magnetic field tilt angle – that has precluded this work from investigating the evolution of quantum oscillatory frequencies as a function of magnetic field tilt angle.

Interestingly, it appears to be the vector normal to the $(\bar{1}01)$ plane, rather than the [101] direction, that is important regarding the symmetry of metamagnetism in $FeSb_2$ in the $c-a$ rotation plane. This may be analogous to another strongly correlated material possessing an orthorhombic crystal structure and exhibiting exotic physical phenomena: the heavy fermion superconductor UTe_2 exhibits magnetic field re-entrant superconductivity to fields exceeding 60 T [177] for magnetic field oriented in a narrow angular range close to the vector normal to the $(01\bar{1})$ plane [178].

5.4 Landau quantisation and temperature evolution of quantum oscillatory amplitude

Given the discussion in chapter 3 of the questions raised to the initial reports of potential unconventional insulating quantum oscillations in WTe_2 and α-$RuCl_3$, it is important to carefully analyse the oscillatory structures measured in the magnetic torque of $FeSb_2$, and make comparison with the expectations of conventional magnetic quantum oscillations predicted by the LK theory [18].

Figure 5.9 plots the oscillatory minima and maxima of the oscillations measured at $\theta = 2^\circ$ and $\theta = 23^\circ$, which are dominated by a low frequency component thus making a

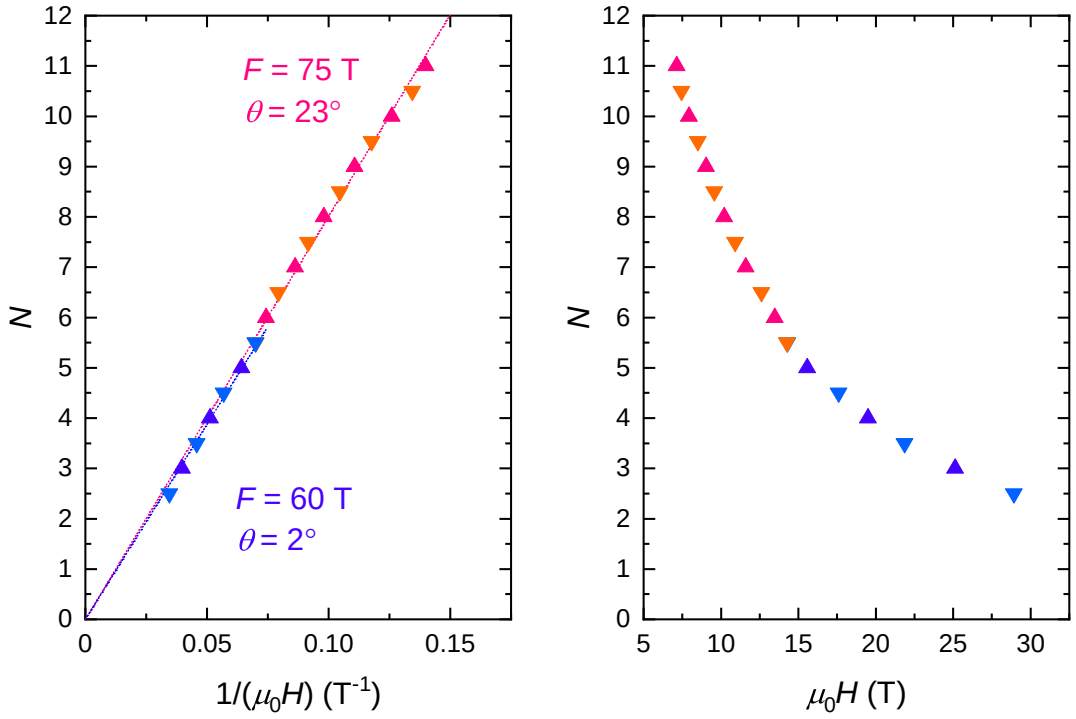

Fig. 5.9. Periodicity of quantum oscillations in inverse magnetic field. Landau-level index, N, plotted linearly in inverse field (left) and linearly in field (right). 'Up' ('down') triangles correspond to the location of oscillatory maxima (minima).

Landau index study feasible. It is apparent – especially for the $\theta = 2°$ data – that the oscillations are not periodic in field but are instead periodic in inverse field. By the considerations introduced in chapter 2, these observations therefore indicate Landau quantisation of itinerant quasiparticles.

To further evaluate whether the observed oscillations follow the form expected by the LK theory, a temperature dependence study was performed. Figure 5.10 shows the temperature evolution of the dHvA effect in $FeSb_2$ for the prominent low frequencies that are visible at this angle over the field range 15 T $< \mu_0 H <$ 30 T. The amplitudes of the waveforms' fast Fourier transforms were analysed as a function of temperature (Fig. 5.11), and found to decay at elevated temperatures in the manner expected for conventional

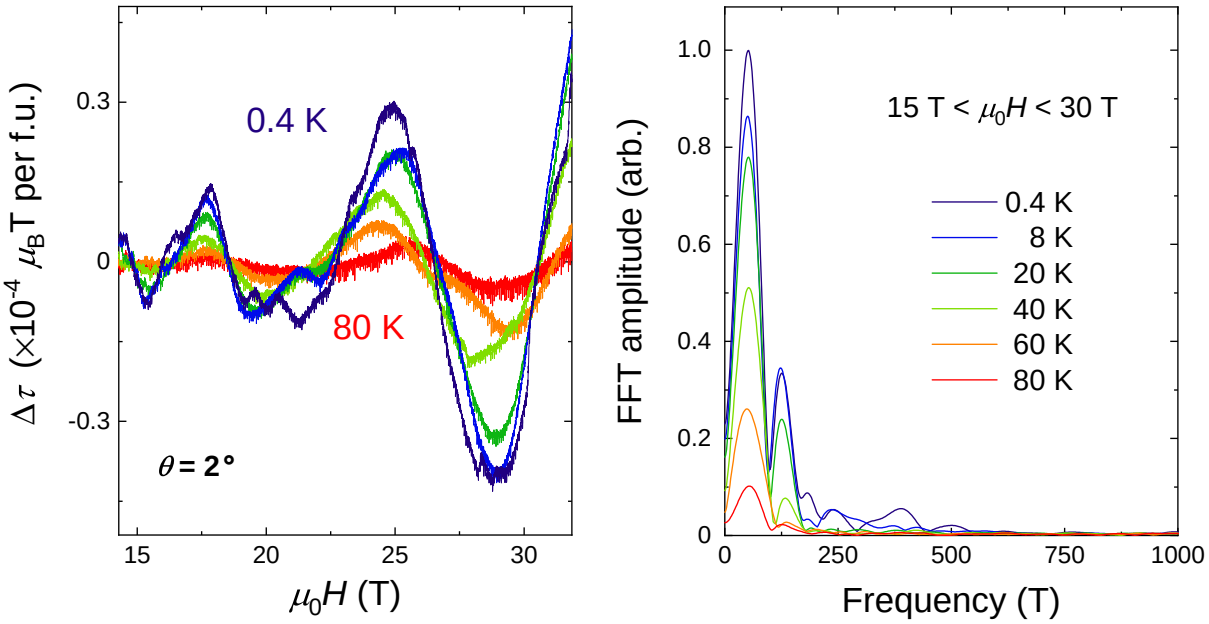

Fig. 5.10. Temperature evolution of quantum oscillations. *Left:* Oscillatory component of τ at $\theta = 2°$ from **H** || [001[towards **H** || [100] at temperature increments between 0.4 K and 80 K. *Right:* FFTs of the data in the left panel. The evolution of FFT amplitude as a function of temperature fits well to the expectation of the LK formula (eqn. 2.5), as would be expected for conventional (charged) Fermionic excitations [18]. Higher frequency components were well resolved over higher field intervals; however, they were found to diminish rapidly at the high temperatures accessed here.

(charged) Fermionic excitations by the LK theory by fitting to eqn. 2.5. The observation of quantum oscillatory amplitude growth down to low temperatures indicates a gapless nature of the responsible excitations [97].

The cyclotron effective mass, m^*, was left as a free parameter in the fitting procedure, and masses in the range 0.07(1) m_e to 0.8(1) m_e were observed, as depicted in Fig. 5.11. It should be noted that for the high frequencies observed in Fig. 5.3, which would be expected to yield yet higher masses, although a sharp attenuation in amplitude with temperature was observed, indicating quasiparticle effective masses of order of a few m_e, a combination of subtle changes in the metamagnetic transition with temperature and the

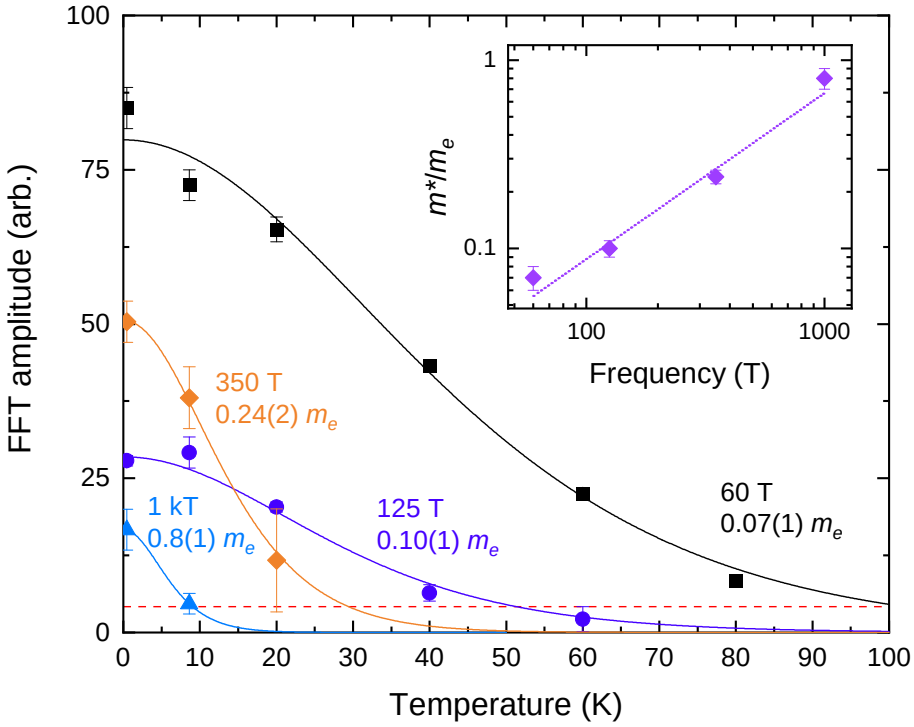

Fig. 5.11. Temperature dependence of quantum oscillatory amplitude. FFT amplitudes of various frequency components at $\theta = 2°$ measured at incremental temperatures from 0.4 K to 80 K. Suitable magnetic field ranges were used to extract the evolution in amplitude for individual frequency branches. Solid curves are fits to eq. 2.5; the red dashed line indicates the noise resolution of the experiment. Error bars are the standard deviation from averaging the results of multiple field sweeps. *Inset:* Cyclotron effective mass, m^*, as a fraction of the bare electron mass, m_e, extracted from performing a fit to the LK temperature formula for each frequency in the main panel.

presence of multiple frequency branches complicates an LK temperature study of these high frequencies. Further experiments, to more carefully probe the temperature evolution of the metamagnetic insulator–to–insulator transition, would be of great assistance in attempting to better understand this evolution.

5.5 Bulk insulating origin of quantum oscillations in $FeSb_2$

5.5.1 Determination of the absolute amplitude

A comparison between the theoretical expectation and experimentally resolved absolute amplitude of the quantum oscillations presented above can be made by reference to section 2.3.1.

By considering the dimensions and Young's modulus of our cantilevers, a value for the spring constant, k, was found to be 28(8) N m^{-1}, with similar values to this also obtained through the gravitational displacement technique [20]. For the case of the quantum oscillations presented in Fig. 5.3, the value of α in eqn. 2.15 may be found through the substitution of the applicable numerical values of $V_{\text{u.c.}} = 5.83 \times 6.53 \times 3.19 = 121$ Å^3, L = 3.8 mm, k = 28 N m^{-1}, d = 100 μm, and $s^3 = 0.95 \times 1.12 \times 0.57$ mm^3, giving α = 0.23 T pF^{-1} μ_B per unit cell.

Now we can compare this with the theoretical amplitude of bulk quantum oscillations expected by application of the Lifshitz-Kosevich theory [18, 78], as laid out in chapter 2. Approximating the effective mass, value of $\sin(\theta)$, and possible range of $\mathcal{F}(r)$ in eqn. 2.17 as each being in the range 0.1-1 allows us to estimate the theoretical amplitude for bulk quantum oscillations in the limit of low temperature, infinite field, and zero spin splitting.

For the dominant ≈ 1450 T frequency in Fig. 5.3, by Eq. 2.17, we expect bulk oscillations to have an amplitude roughly in the range 10^{-5} to 10^{-3} μ_B per unit cell. (It should be noted that the possibility of pocket degeneracy adds further uncertainty to this value.) Comparing this result with the experimentally observed oscillations in Figure 5.3, where the amplitude of the dominant ≈ 1450 T frequency at 42 T was found to be approximately 4.7×10^{-4} pF, use of Eq. 2.15 in conjunction with eqn. 2.7, with Dingle damping factor B_D specific to each frequency branch and found to be ≈ 150 T for this frequency [18], yields an experimentally observed quantum oscillatory amplitude of ≈ $10^{-4}/\sin(\theta)$ μ_B per unit cell. Given that $\sin(\theta)$ lies approximately in the range 0.1-1, the observed quantum oscillations are thus consistent in order of magnitude with the theoretical expectations for

a bulk, three dimensional Fermi surface.

5.5.2 Ruling out an extrinsic impurity origin

Given the multitude of evidence indicative of the presence of metallic surface state formation at low temperatures in $FeSb_2$ that shall be presented in section 6.2, it is therefore important to assess whether this may be the origin of the quantum oscillations reported above.

Firstly, as we shall see when examining Corbino disc magnetotransport measurements in section 6.3.1, a strong $1/\sin(\theta)$ dependence for the angular evolution of quantum oscillations would be expected for a 2D Fermi surface [179] in the case of them arising from a metallic surface state. However, as depicted in Fig. 5.8, the evolution of τ (and hence $\Delta\tau$) with magnetic field tilt angle is much more complicated than some simple $1/\sin(\theta)$ progression. Furthermore, the three regimes of contrasting insulating behaviour, as mapped above, are characteristic in changes in the overall (bulk) magnetic torque of the sample. Unlike the electrical transport measurements presented in chapter 6, magnetic torque is very much a bulk-sensitive measurement, so it is extremely unlikely that they should be dominated by the contribution from a surface layer alone.

The quantitative determination of the absolute amplitude given above, which found the experimentally observed quantum oscillatory amplitude to be in the range $\approx 10^{-4}/\sin(\theta)$ μ_B per unit cell, was based on considering the bulk volume of a crystal. In general, surface layers represent a small fraction that is merely $\sim 10^{-6}$ of the total number of unit cells present in a typical bulk crystal. Hence, for the quantum oscillations presented in section 5.2 to emanate solely from a metallic surface layer, their amplitude would be $\approx 10^{2}/\sin(\theta)$ μ_B per surface unit cell, which is unphysically large [2]. Given that this result is several orders of magnitude larger than the maximal amplitudes that could be explained by the LK theory, the observed dHvA effect in $FeSb_2$ is therefore inconsistent with an attribution to a metallic surface state origin.

[2] Note also that as the $\sin(\theta)$ term lies approximately in the range 0.1-1, this value is only a lower bound.

It is also important to consider whether these observations could be emanating from some alien metallic impurity phase hosted within the material. To investigate this, a comprehensive suite of purity analyses was undertaken, as detailed in section 4.1.2. These measurements limited the inclusion of any extraneous element to < 100 ppm (by mass spectrometry), and the inclusion of magnetic impurities to 60(20) ppm (by a Langevin magnetic susceptibility study). These results point to the extremely high purity of the $FeSb_2$ samples investigated in this study. Furthermore, quantum oscillations were observed on multiple samples from different growth batches, with different sources of starting materials, adding further confidence to the intrinsic nature of the dHvA effect within the insulating bulk of $FeSb_2$.

Furthermore, a strong argument in favour of a bulk-insulating origin of the dHvA effect in this material stems from the dramatic quenching of quantum oscillations upon entering Regime III. Figure 5.6 shows oscillations that have been scaled by the reciprocal of their Dingle damping coefficient, thereby presenting them in the infinite-field limit for all fields [18]. If the oscillations were emanating from some impurity phase contribution, or indeed from some other unspecified extrinsic source, then the measured torque signal would be a combination of the $FeSb_2$ background torque in combination with the torque response of the metallic impurity (including its oscillations). Therefore, at high fields when $FeSb_2$ undergoes the metamagnetic transition from Regime II to Regime III, the impurity/metallic contribution should be unaffected, hence the oscillations should still be arithmetically summed with the torque response of $FeSb_2$.

However, this is very much not what is observed – in Regime III the dHvA effect has been dramatically quenched, although at these very high fields the oscillations that were clearly within experimental resolution down at $\mu_0 H \approx 10$ T should be even better resolved at $\mu_0 H \approx 40$ T. That the observed oscillations show such intimate connection to changes in the background magnetic torque of $FeSb_2$ provides yet further indication that they do indeed emanate from the insulating bulk of this intriguing material, and not from any extrinsic impurity, metallic surface state, or other origin.

Note on the SdH effect

The quantum oscillations presented in this chapter have focussed entirely on measurements of the magnetisation of $FeSb_2$, which has been shown to display high amplitude, high frequency oscillations emanating, remarkably, from the insulating bulk of the material.

High magnetic field studies of the resistivity were also undertaken, to search for evidence of the SdH effect. However, as will be shown in Fig. 7.8, for example, no evidence of the SdH effect was resolved within the experimental resolution up to field strengths of 70 T. The prominent presence of the dHvA effect in the magnetisation, but notable lack of the SdH effect in the resistivity, draws yet further interesting parallels between $FeSb_2$ and SmB_6.

5.6 Complex magnetism in $FeSb_2$

5.6.1 Anisotropic bulk magnetisation

For additional context in considering some of the remarkable features in the anisotropic (torque) magnetisation presented above, it is informative to examine some unusual characteristics of the isotropic magnetisation.

Figure 5.12 shows the magnetisation, M, as a function of applied field for various orientations of field alignment. Measurements were obtained in a QD Magnetic Properties Measurement System, with samples mounted on a quartz holder to minimise the background signal. For $\mu_0 H > 2$ T, a clear anisotropy is observed for $\mathbf{H} \parallel [100]$ compared to $\mathbf{H} \parallel [010]$, with $\mathbf{H} \perp (110)$ lying in between. Strikingly, however, $\mathbf{H} \parallel [001]$ shows markedly different behaviour – here the sample is responding diamagnetically, whereas for the other three orientations a clear paramagnetic response is observed.

Upon warming, for $\mathbf{H} \parallel [001]$ a diamagnetic response (i.e. negative sign of the suscep-

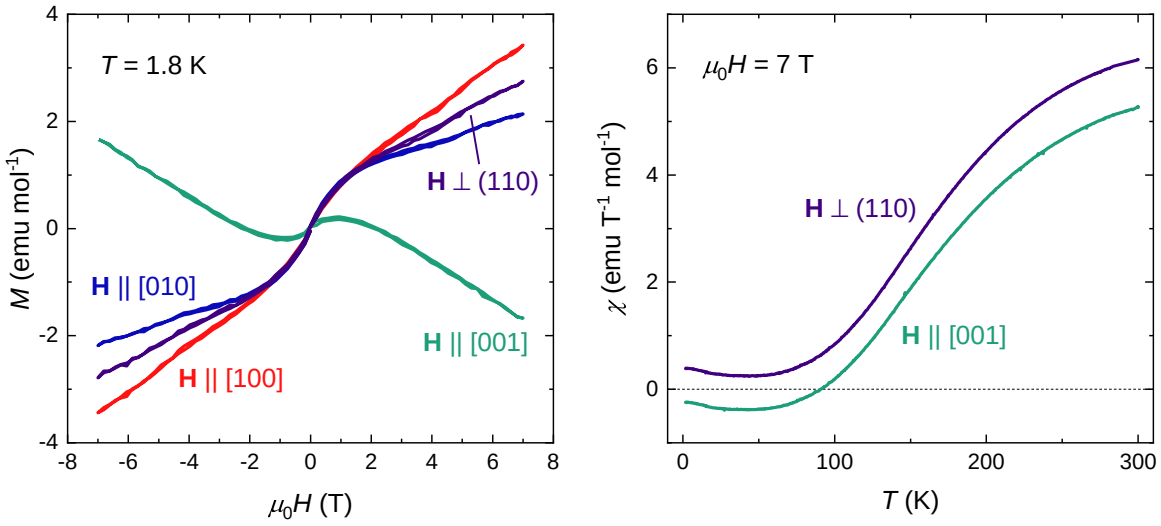

Fig. 5.12. Anisotropic bulk magnetisation. *Left:* Magnetisation, M, of an $FeSb_2$ single crystal at 1.8 K with magnetic field applied along various high symmetry directions. *Right:* Magnetic susceptibility, $\chi = M/(\mu_0 H)$, as a function of temperature.

tibility, χ) is seen to persist up to $\approx$ 90 K, whence χ becomes positive and thermally activated paramagnetism is seen to persist up to at least 300 K, in correspondence with prior reports [180, 181]. Interestingly, for $\mathbf{H} \perp (110)$, χ is positive across the entire temperature range, and the $\mathbf{H} \perp (110)$ and $\mathbf{H} \parallel [001]$ curves do not converge at high temperature, but instead display a strong anisotropy throughout the entire 1.8-300 K measurement range.

As well as enduring to high temperatures, the dia/paramagnetic dichotomy is also observed to persist up to extremely high fields. Figure 5.13 shows M measured by the extraction magnetometry method to high fields for $\mathbf{H} \perp (110)$ and $\mathbf{H} \parallel [001]$. Unfortunately, the size of the signal obtained in this measurement was comparatively small (extraction magnetometry measurements are typically performed on e.g. ferromagnets with much larger values of M), so there was difficulty in quantitatively calibrating the size of M observed here; hence, M is quoted in arbitrary units. However, the *sign* of M is the important feature of this dataset, and was very well resolved to be positive for $\mathbf{H} \perp (110)$ and negative for $\mathbf{H} \parallel [001]$. These measurements were performed by aligning multiple individual

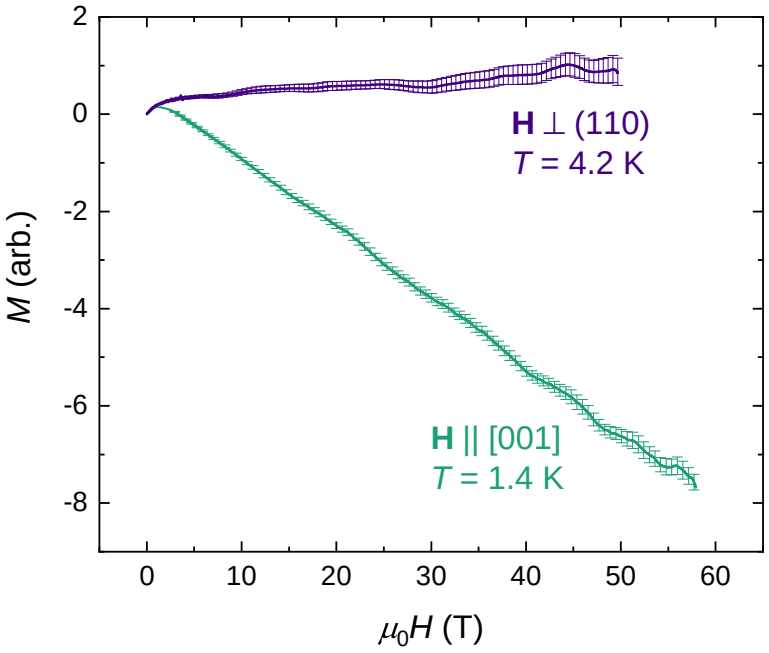

Fig. 5.13. Anisotropic magnetisation to high fields. Extraction magnetometry data for **H** ⊥ (110) (purple) and **H** || [001] (green). The dia/paramagnetic dichotomy is seen to persist up to fields $\gtrapprox$ 50 T. This dataset was acquired in collaboration with A. Miyake of the Institute of Solid State Physics, University of Tokyo, and with my colleague H. Liu. Multiple single crystal $FeSb_2$ samples were oriented within a small volume and all measured together, in order to maximise the observed signal. Error bars are calculated as the standard deviation of averaging multiple pulses, but are very likely an underestimate of the true experimental uncertainty – due to difficulties in calibrating the very small measurement signal in the noisy environment of a pulsed magnet, M is therefore given in arbitrary units.

single crystal specimens together in a small volume, which were then measured simultaneously. In future a follow up study, with field oriented normal to the (110) plane, would be informative in order to probe the nature of the metamagnetic transition uncovered by the torque magnetometry measurements discussed previously.

That the isotropic magnetisation of $FeSb_2$ should exhibit the anomalous properties

of a paramagnetic/diamagnetic transition in temperature for **H** ∥ [001] (but not for the other principal axes), temperature activated paramagnetism for all directions of applied field, but a robust para/diamagnetic dichotomy at low temperatures up to fields $\gtrapprox$ 50 T, yields interesting clues pertaining to the nature of the angular phase diagram depicted in Fig. 5.8 for the anisotropic magnetisation measured by torque magnetometry. Notably, diamagnetism along the [001] direction persists to $\mu_0 H > 50$ T.

For both the isotropic and anisotropic magnetisation, with field aligned along the [001] direction we see a termination in the behaviour observed for other orientations – in the anisotropic magnetisation, the transition between Regimes II & III is pushed above 40 T at 2° from [001], whereas after only a 30° rotation away (towards **H** ∥ [100]) this transition is observed below 20 T. Meanwhile, in the isotropic magnetisation, a highly unusual form of temperature activated paramagnetism is observed for all orientations at elevated temperatures, but at low temperature the [001] direction is again special – this time, by exhibiting a magnetic susceptibility of the opposite sign to the [100] and [010] directions.

5.6.2 Proximate ground states and metamagnetic modelling

We consider here a minimal model that can qualitatively describe characteristic features of a metamagnetic transition in the vicinity of a critical magnetic field, focusing on the quantum oscillations connected to changes in the background magnetic torque presented above. A key ingredient of the minimal model is an internal magnetic field proportional to the bare magnetisation, which arises from a Weiss exchange feedback field, and has the effect of enhancing the linear magnetic field-dependent bare magnetisation. Including the Weiss exchange feedback field has the effect of inducing a metamagnetic transition at a critical magnetic field where the magnetisation tends to diverge. While such metamagnetic transitions are widely seen in metals [184], $FeSb_2$ remains robustly insulating up to magnetic fields at least as high as 70 T, with no indication of a significant charge gap reduction up to these fields. As recently hypothesised in [185], spin fluctuations may be responsible for suppressing the metallic magnetic order predicted by previous

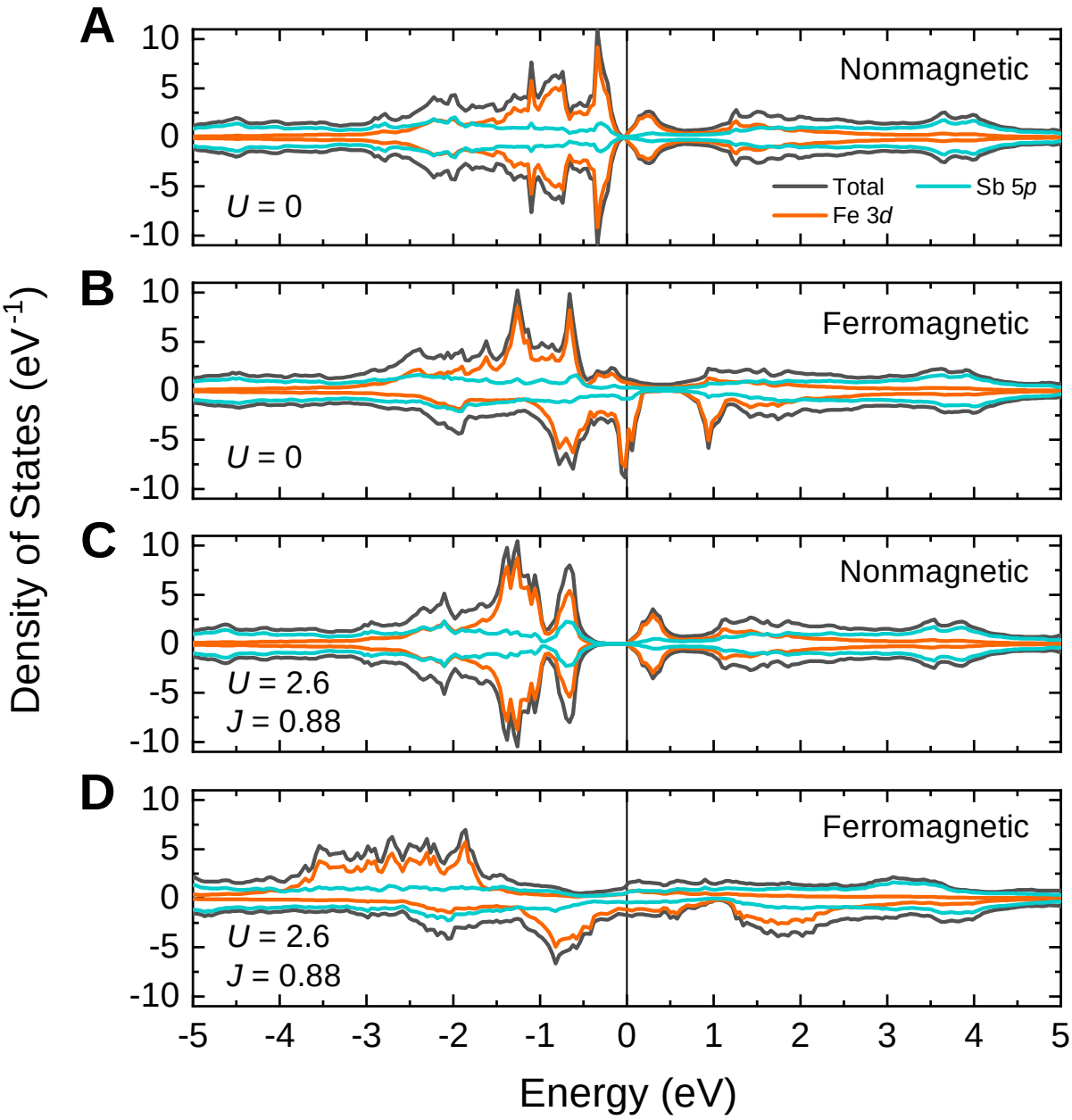

Fig. 5.14. Orbitally-resolved spin-up and spin-down density of states in the non-magnetic and ferromagnetic states. DFT+U calculated orbitally-resolved spin-up and spin-down density of states in the non-magnetic and ferromagnetic states with (**A** & **B**) $U = 0$ and (**C** & **D**) $U = 2.6$, $J = 0.88$. The inclusion of finite U widens the intrinsic gap of the non-magnetic state; meanwhile, the ferromagnetic state remains metallic.

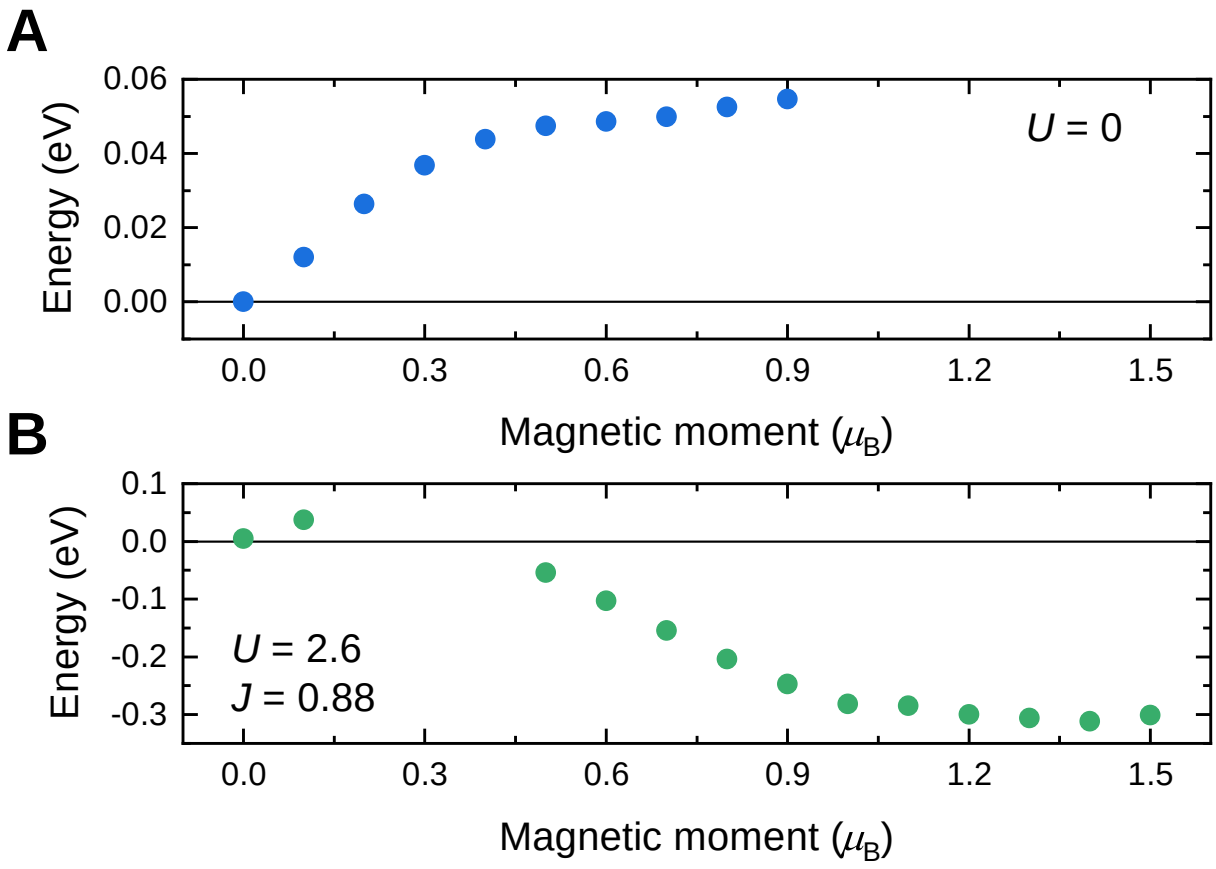

Fig. 5.15. Fixed spin moment calculations of the energy. Fixed spin moment calculations for the $U = 0$ and $U = 2.6$, $J = 0.88$ cases. (**A**) Without U, the non-magnetic state is stable, while there is a local minimum with moment $\approx$ 0.7 μ_B. (**B**) For a finite value of U, the ferromagnetic state with moment $\approx$ 1.2 μ_B becomes stable, in concurrence with previous theoretical studies [182, 183]. For moments up to 0.5 μ_B, the calculations could not be converged due to an electronic gap that cannot be overcome with insufficient field strength.

work [182, 183] and in our DFT+U calculations (Figs. 5.14, 5.15 & 5.16) to occur at high magnetic fields in $FeSb_2$.

We can model a metamagnetic transition in an isotropic system by a paramagnetic

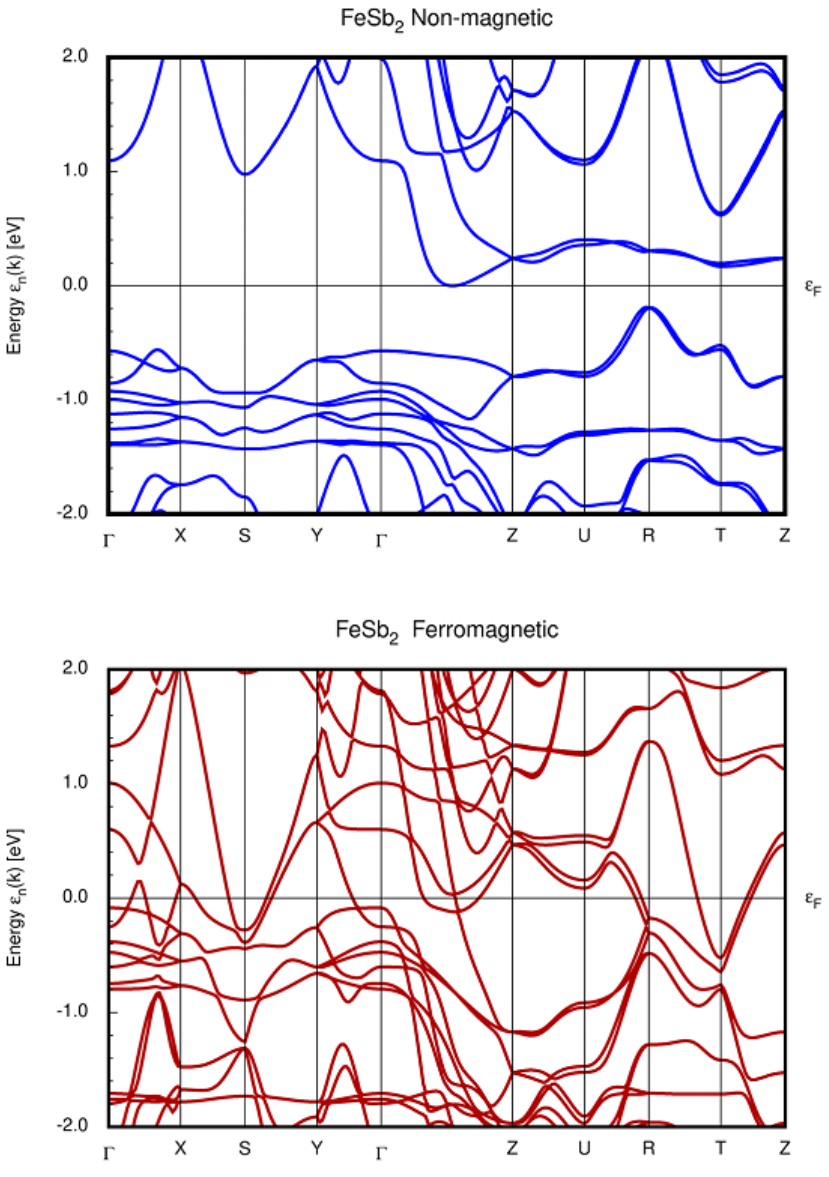

Fig. 5.16. Calculated bandstructure of $FeSb_2$. The non-magnetic (top) and ferromagnetic (bottom) band structures of $FeSb_2$ with $U = 2.4$, $J = 0.88$. The U correction widens the gap of the non-magnetic states with an essentially uniform shift of bands from the $U = 0$ calculation. The ferromagnetic bands remain metallic for finite U, and indicate a complex, multi-sheet Fermiology for finite U. Figure courtesy of collaborator M. D. Johannes [44].

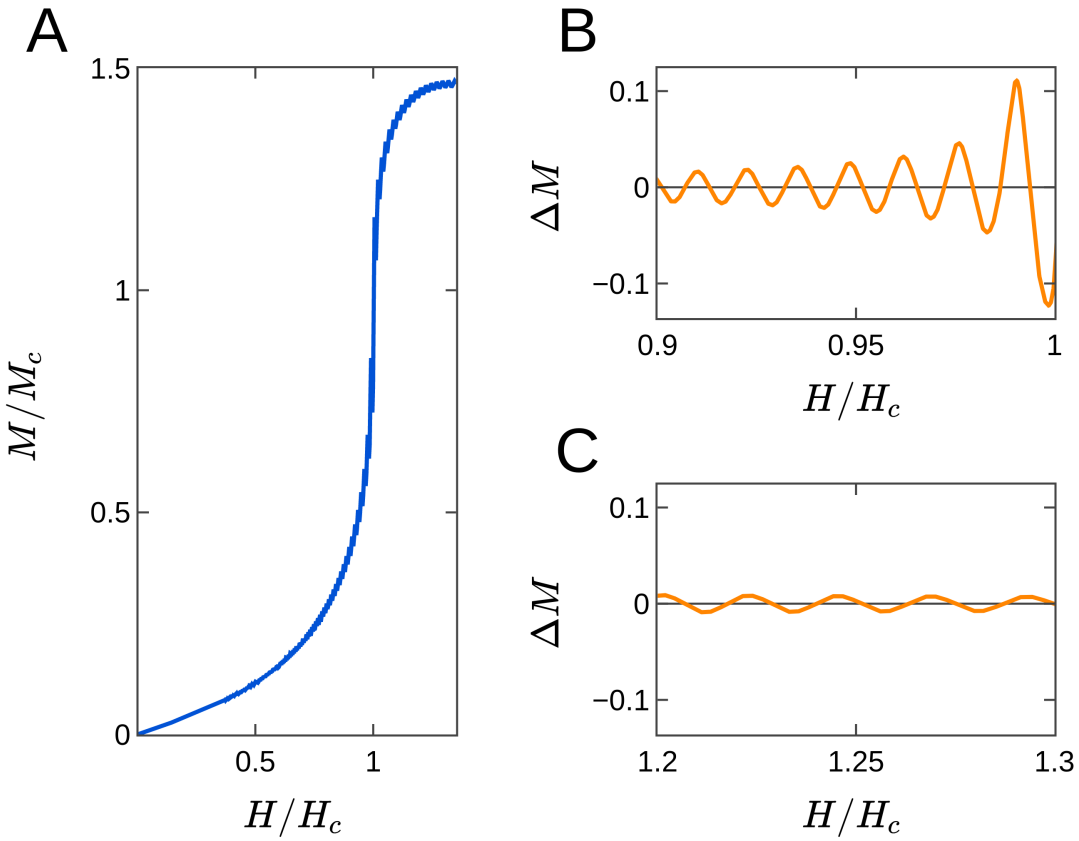

Fig. 5.17. Minimal model of quantum oscillatory behaviour closely connected to a metamagnetic transition. (**A**) Net magnetisation, M, as a function of magnetic field, H. Both magnetisation and magnetic field are normalised against their critical values at which the metamagnetic transition occurs (M_c, H_c). (**B**) Magnetic background subtracted magnetisation (ΔM) with (**B**) highlighting the oscillation amplitude enhancement upon approaching the transition, and (**C**) the subsequent strong suppression of oscillation amplitude upon surpassing the transition.

magnetisation M odd in the applied magnetic field $\mu_0 H$, plus a Weiss exchange feedback field λM. This modelling was performed in collaboration with colleagues G. G. Lonzarich and G. F. L. Rodway-Gant [44]. Assuming that M is an analytic function, a minimal expansion in the paramagnetic regime leading to a metamagnetic transition takes the form [186]

$$M = \alpha(\mu_0 H + \lambda M) + \beta(\mu_0 H + \lambda M)^3 + \gamma(\mu_0 H + \lambda M)^5 \tag{5.1}$$

where $\alpha > 0$ is the initial bare paramagnetic susceptibility, $\beta > 0$ describes the upturn required to generate a metamagnetic instability once the Weiss exchange feedback field is included, and $\gamma < 0$ describes the initial tendency for the magnetisation to saturate with increasing magnetic fields. The solution of this self-consistent equation for $M(H)$ can produce a characteristic sharp upturn, analogous to that observed in Fig. 5.1. A more complete description beyond the critical field and of the torque would require a complicated anisotropic model; however, the upturn in the magnetisation should result qualitatively in a similar upturn in the field dependence of the torque as observed.

If the total magnetisation includes an oscillatory component M_{osc} that does not contribute to the Weiss feedback field, then the amplitude of the oscillations is essentially unaffected by the metamagnetic transition. However, if M_{osc} is included in the Weiss exchange feedback field, then the amplitude of the oscillations is predicted to rise sharply at the metamagnetic transition, assuming M_{osc} to take the form

$$M_{osc} = a \exp\left(\frac{-B_D}{\mu_0 H}\right) \sin\left(\frac{2\pi f}{\mu_0 H}\right) \tag{5.2}$$

where the parameters a, B_D and f represent respectively, the infinite field amplitude, Dingle damping factor, and quantum oscillation frequency. The key features of this model are presented in Figure 5.17.

For non-zero values of λ, in the vicinity of a critical magnetic field, H_c, the model yields a metamagnetic transition. As the magnetisation from quantum oscillations interacts with the Weiss exchange feedback field, the enhancement in background magnetic torque ap-

proaching the metamagnetic transition is accompanied by a stark growth in quantum oscillation amplitude. Following the transition, quantum oscillations are quenched, unlike the case of a simple paramagnet yielded by setting $\lambda = 0$ for which we would see a continuous growth in oscillation amplitude with increasing magnetic field superimposed on a linear magnetic background. We note that DFT+U calculations indicate a close proximity to magnetically ordered ground states (Fig. 5.15), indicating that Regime III may constitute an antiferromagnetically ordered insulating phase in which spins are locked and hence no further insulating quantum oscillations are exhibited.

It should be noted that a key assumption of this model is that it presumes the oscillatory frequency remains constant (in inverse field) at the transition and on both sides of it. However, in the case of metamagnetic transitions in clean metals, the oscillatory frequency can be strongly affected by the result of non-linear spin splitting of the quasiparticle bands in proximity to a metamagnetic transition [187]. Should the Fermi surface area be a function of magnetic field, $A(B)$, this would lead to a change in the observed oscillatory frequency, $f(B)$, as $f(B) \propto A(B) - B\frac{\partial A(B)}{\partial B}$; thus, should there be considerable band dispersion accompanying a metamagnetic transition, a study of quantum oscillatory frequency evolution in proximity to the transition may elucidate valuable information about the microscopic mechanism responsible [188]. Therefore, a future extension of this model would be to consider these effects on the specific case of metamagnetism in $FeSb_2$.

In summary, let us consider the implications of this minimal model at the metamagnetic transition, where the magnetisation tends to diverge at the critical magnetic field. According to this model, if the total magnetisation includes a quantum oscillatory component that does not contribute to the Weiss exchange feedback field, then the quantum oscillation amplitude is essentially unaffected by the metamagnetic transition. However, in the case of quantum oscillations dominated by spin-orbital magnetism, this quantum oscillatory component is part of the magnetisation fed back via the Weiss exchange feedback field. In this case, quantum oscillations are strongly enhanced against the steeply upturning magnetisation at the onset of the metamagnetic transition. Hence, our experimental finding of strongly enhanced quantum oscillations against a steeply upturning magnetic torque background on the rising side of a metamagnetic insulator–to–insulator

transition followed by an abrupt suppression on the falling side of the transition thus points to spin-orbital magnetism-dominated quantum oscillations, differentiating $FeSb_2$ from previously discovered unconventional insulating materials.

5.7 Summary

This chapter presented magnetic measurements on high purity single crystal $FeSb_2$ specimens. Three regimes of contrasting magnetic behaviour were identified from a torque magnetometry study of the magnetic torque as a function of the magnetic field tilt angle. Magnetic torque quadratic in applied magnetic field strength was observed at low fields, characterising Regime I, which upturned sharply (in Regime II) to a peak on the rising side of a metamagnetic transition. Above this peak, on the falling side, Regime III is characterised by magnetic torque almost linear in applied magnetic field strength. Low frequency, small amplitude quantum oscillations were resolved in Regime I, growing to high frequencies and large amplitudes in Regime II. Remarkably, these quantum oscillations were found to emanate from the insulating bulk of the material, indicating an anomalous Fermi surface hosted by this material, adding $FeSb_2$ to the growing list of unconventional insulating materials. Furthermore, at yet higher fields, the quantum oscillations were found to be quenched in Regime III above the metamagnetic transition. Other magnetic properties of $FeSb_2$ were examined and discussed, and the three regimes of magnetic behaviour were found to be qualitatively described by invoking a minimal magnetic model. The connection between insulating quantum oscillations and pronounced changes in the bulk magnetic properties of the material sets $FeSb_2$ aside from previously reported unconventional insulators, and strongly indicates that strong spin-orbit interactions are responsible for the manifestation of unconventional insulating quantum oscillations.

6

Electrical transport measurements of metallic surface states on $FeSb_2$

God made the bulk; the surface was invented by the devil.

– Wolfgang Pauli

In this chapter, a series of electrical transport studies on $FeSb_2$ are presented. They reveal several signatures indicative of the presence of low-temperature metallic surface states in this material. These include the observation of a low-temperature resistivity plateau, a rotational magnetotransport symmetry evolution on cooling, an inversion in resistance observed between local and nonlocal wiring configurations, and sharply contrasting magnetotransport results between employing Corbino and Hall-bar or van der Pauw geometries. Similarities with the topological Kondo insulator candidate SmB_6 are compared and discussed.

6.1 Introduction

The manifestation of electron-electron correlation effects in the bulk of electrically insulating materials has led to several significant advancements in our understanding of quantum matter over the past century [27, 189, 190]. In recent decades, the theoretical prediction, and subsequent experimental realisation, of the juxtaposition of a conducting metallic surface state atop a non-correlated insulating bulk has likewise led to several interesting results [7, 8, 191–194]. The interplay of these two phenomena – metallic surface states in combination with strong bulk interactions – may thereby prove to be fertile ground for exploring novel physical behaviour.

The field of topological insulators (TIs) has exploded over the past decade [7, 8]. Unfortunately, the presence of significant bulk conduction channels in typical non-correlated TIs makes their surface states difficult to isolate [195]. A promising alternative route to achieving this lies in finding correlated TIs, in which bulk conduction may be strongly gapped out. The low-temperature resistivity anomaly [41] of SmB_6, a strongly correlated Kondo insulator [34], has posed a long-standing puzzle. It was later predicted that this feature may be the result of correlation-induced band hybridisation, leading to the formation of a topologically protected metallic surface state [32]; this theoretical prediction has led to intense interest in this material over the past decade [33]. This being said, the research community is yet to reach a consensus on whether the surface states present on SmB_6 are undoubtedly attributable to a topologically non-trivial origin [196].

However, the search for similar model systems has thus-far proved elusive, preventing a comparative analysis of what crucial constituents are required in order to produce such an exotic correlation-driven (putatively) topological surface state, leaving several open questions unresolved [34]. The identification of other materials, with similar low temperature electrical properties to SmB_6, is therefore urgently called for.

6.2 Metallic surface state on $FeSb_2$

6.2.1 Anomalous low-temperature resistance plateau

Recent angle-resolved photoemisurface stateion spectroscopy (ARPES) measurements on $FeSb_2$ have revealed the presence of low-temperature metallic surface states [46, 198]. These observations are reminiscent of previous findings on SmB_6 [34]. The low-temperature electrical resistivity, ρ, of $FeSb_2$ is also very similar to that of SmB_6 (Fig. 6.1). In general, the resistivity of a Kondo insulator should increase logarithmically as $T \rightarrow 0$ K [26]; however, both SmB_6 [71, 199] and $FeSb_2$ exhibit low-temperature resistance plateaux, a hallmark of the development of a surface state, for $T \lessapprox 4$ K. All sample batches examined in this study exhibited a low temperature resistance plateau (Fig. 4.2). The formation of this plateau is found to be accompanied by a steep peak in the Hall coefficient, -R_H.

Fitting the $FeSb_2$ data in Fig. 6.1 to the standard Arrhenius activation model, of the form $\rho \propto \exp(\Delta/k_B T)$, yields a high temperature indirect bandgap, Δ_1, of ≈ 12 meV for $T > 30$ K (Fig. 6.1 upper right inset), comparable with prior reports [37]. However, at lower temperatures another gap – $\Delta_2 \approx 3.7$ meV – opens up, of comparable magnitude to the 4.0 meV gap in SmB_6 attributed to Kondo-induced band hybridisation [34]. Very similar observations, of low-temperature resistivity saturation concomitant with a dramatic reduction in R_H, have previously been attributed with topologically protected surface state formation in the non-correlated TIs Bi_2Te_2Se [200] and $Bi_{1.08}Sn_{0.02}Sb_{0.9}Te_2S$ [201]. The notable similarities between these materials and $FeSb_2$ are strongly suggestive of similar microscopic mechanisms at play in this system.

6.2.2 Rotational symmetry evolution

To further investigate the potential surface state origin of the low-temperature resistivity plateau of $FeSb_2$, a rotational magnetotransport study was performed. Figure 6.2 shows the angular-dependent magnetoresistance (ADMR) of two $FeSb_2$ samples and one SmB_6

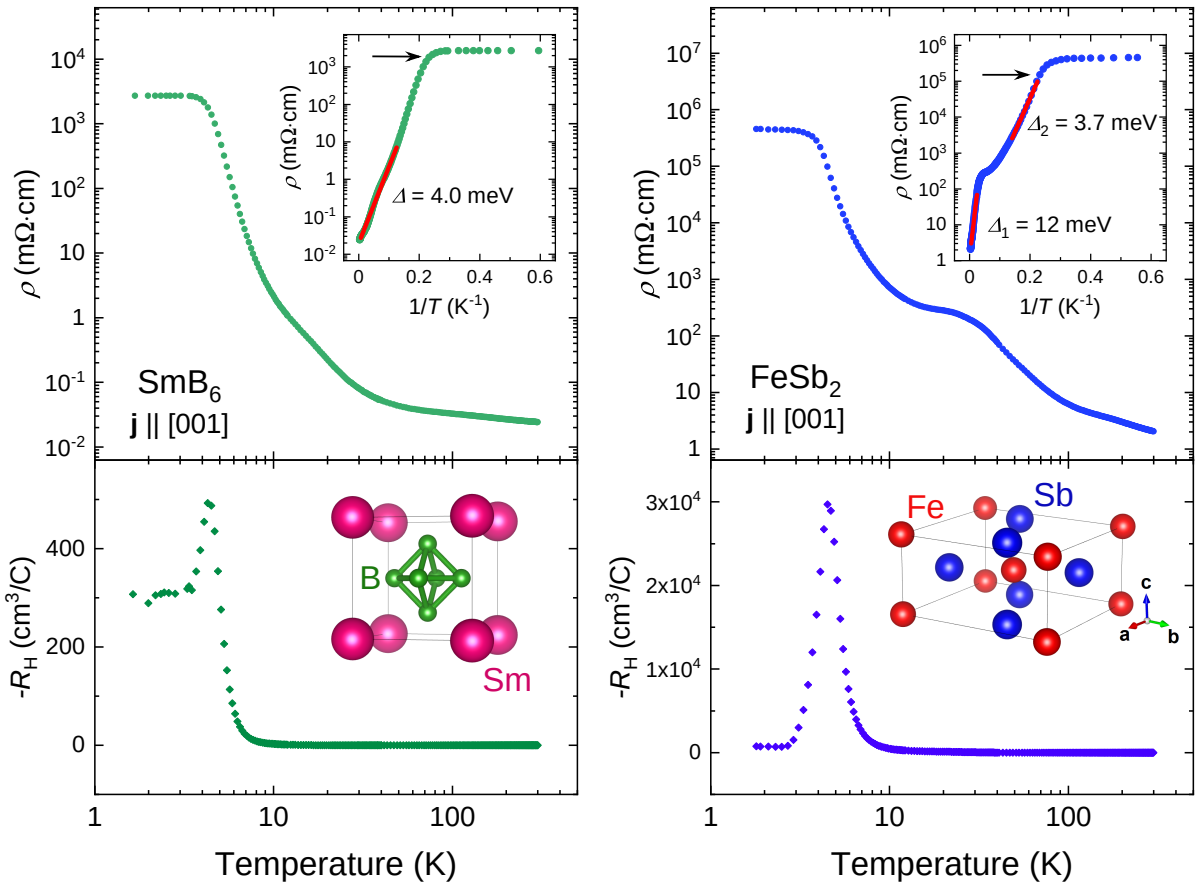

Fig. 6.1. Low-temperature electrical transport anomalies. Resistivity, ρ, and Hall coefficient, R_H, as functions of temperature for SmB_6 (left, green symbols) and $FeSb_2$ (right, blue symbols). Upper insets show resistivity against inverse temperature, with arrows indicating the location of the peak in $-R_H$, which occurs for both materials in close proximity to the resistivity plateau. Red lines show regions fitted to extract activated charge gap energies Δ. $FeSb_2$ exhibits two gaps, with the lower temperature one, Δ_2, being of very similar magnitude to the sole gap of SmB_6. Lower insets show the respective crystal structures [163, 164, 197].

sample as a function of rotation angle θ, at various temperatures in applied magnetic fields of ± 14 T. Samples with large surface to volume ratios were chosen, with $\theta = 0°$ cor-

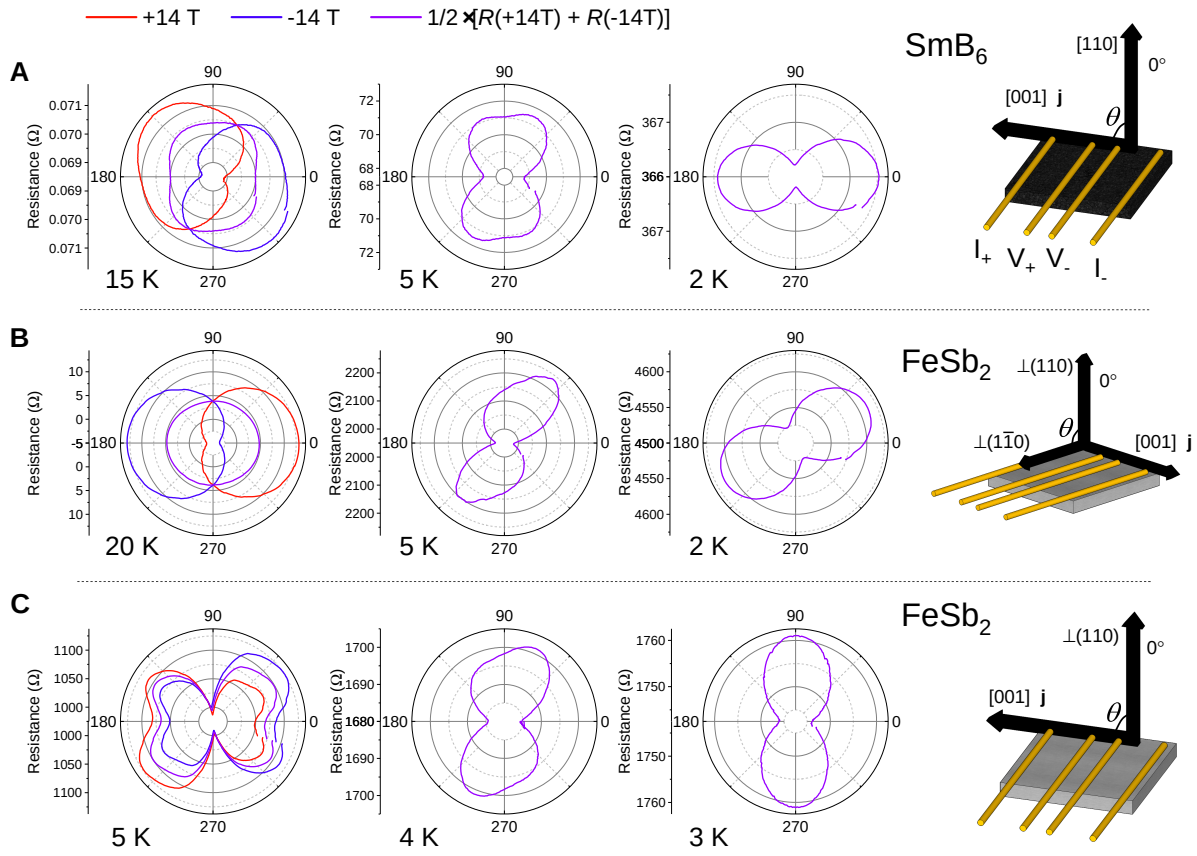

Fig. 6.2. Magnetotransport evolution from bulk- to surface-dominated symmetry on cooling. (A) Magnetoresistance of SmB_6 at successive temperatures as a function of rotation angle, θ. In all panels, the right hand side schematic gives the applied current direction, **j**, and rotational plane, while purple curves in each plot give symmetrised resistance for applied magnetic fields of ± 14 T, to exclude any transverse contributions. At 15 K, away from the resistivity plateau, SmB_6 exhibits C_4 rotational symmetry, whereas at 2 K, on the plateau, this has reduced to C_2 symmetry with a peanut-shaped trace. **(B)**, Similar temperature progression on an $FeSb_2$ crystal as for SmB_6 in panel **A**, clearly exhibiting a peanut-shaped trace at 2 K, indicative of surface-dominated conduction [202]. **(C)**, $FeSb_2$ measured along a different rotational plane to that in **B**, indicating that the development of the pronounced surface-dominated profile at low temperatures is not specific to a singular rotation plane.

responding to field applied normal to the two largest (parallel) faces, the top one of which was contacted with gold wires for standard four-point electrical transport measurements as indicated in the schematics in Fig. 6.2. For $T \geq 15$ K, well away from the plateau, both materials' longitudinal magnetoresistances exhibit almost isotropic rotational symmetry, as expected for simple bulk conduction. However, on cooling to $T \leq 3$ K, within the plateau region, the rotational magnetoconductance profiles of both SmB_6 and $FeSb_2$ undergo a pronounced evolution. In Fig. 6.2A at 5 K the studied SmB_6 sample exhibits nodes (antinodes) in the magnitude of the magnetoresistance at 0° and 180° (90° and 270°); however, at 2 K this has swapped to give nodes (antinodes) at 90° and 270° (0° and 180°). Comparatively, the $FeSb_2$ sample in Fig. 6.2C evolves similarly – with a stark difference between the 5 K and 4 K temperature points, whereby the nodes at 90° and 270° at 5 K have shifted to 0° and 180° at 4 K.

Interestingly, this evolution goes through a drastic change around the temperature of the Hall effect peak (Fig. 6.1), with a convolution of 3D and 2D transport signatures observed in the 'butterfly' shape of the 5 K trace in Fig. 6.2C – similar behaviour has previously been reported in studies of Weyl semi-metals [203]. At the lowest temperatures, a distinct peanut-shaped trace is observed in the rotational magnetoresistance of $FeSb_2$, in marked similarity with prior SmB_6 reports [202, 204].

In Figure 6.3, positive field polarity ADMR curves of both SmB_6 and $FeSb_2$ are plotted this time on Cartesian axes rather than radially.[1] At elevated temperatures (≥ 15 K), both materials exhibit a single period of oscillation in their ADMR traces upon traversing through one full rotation of 360°. This is typical of isotropic bulk conduction in solids [202, 203]. However, on cooling to 2 K, two notable changes have occurred. The first is that the resistance of both materials has increased by several orders of magnitude; the second is that there are now two ADMR oscillations per full rotation.

This symmetry evolution fits well within the surface state model, whereby at the low-

[1]Note that there is some finite transverse contribution to these data owing to slightly misaligned contact placing, giving rise to features in the data such as the $FeSb_2$ 20 K resistance being negative for some angles; in Fig. 6.2 the purple curves give symmetrised resistances whereby transverse components have been eliminated by averaging over both field polarities.

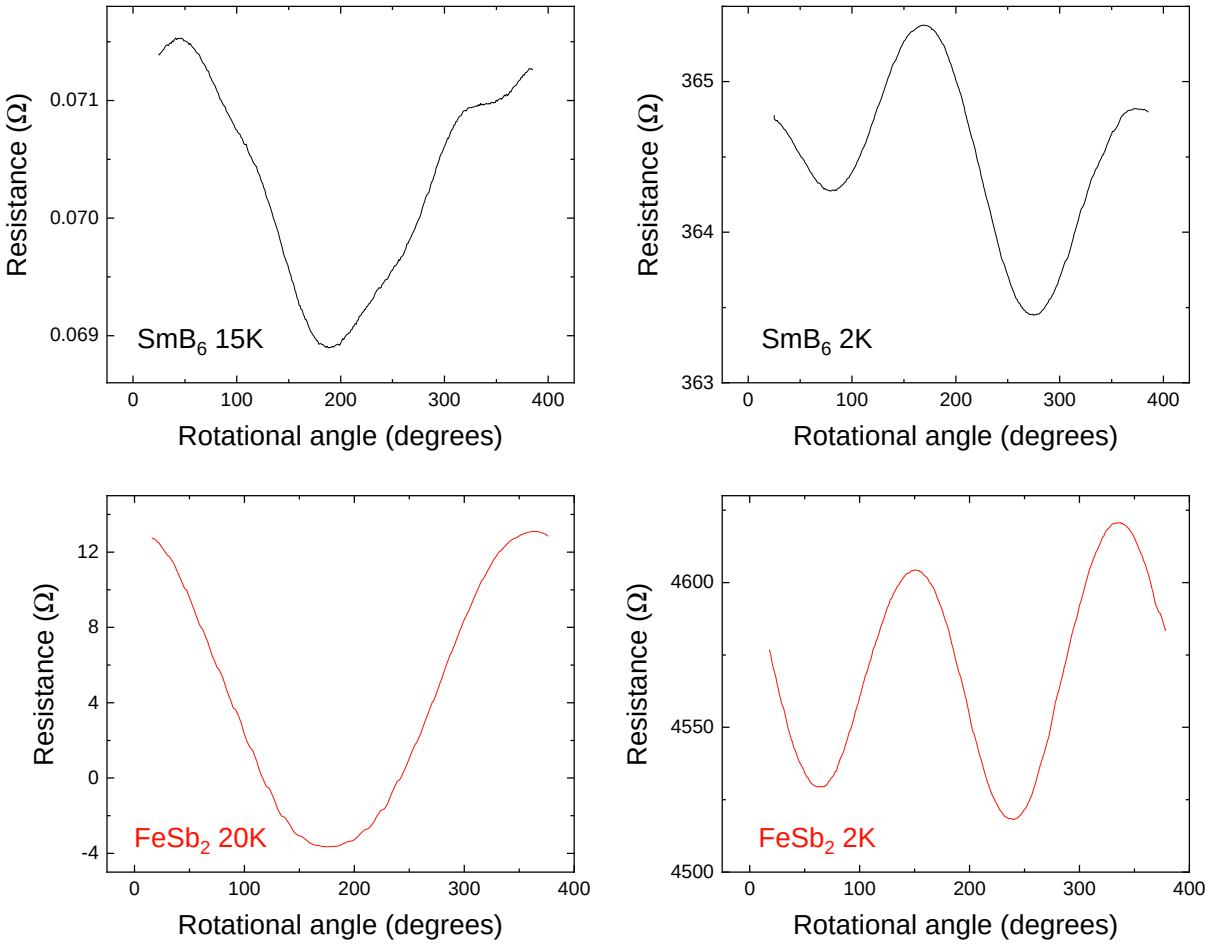

Fig. 6.3. Rotational symmetry evolution. Subset of the data in Fig. 6.2, for positive field polarity of 14 T, of SmB_6 (top, black) and $FeSb_2$ (bottom, red) presented here in Cartesian plots. At elevated temperatures ($T \geq 15$ K) both materials exhibit angular-dependent magnetoresistance traces traversing a single period per 360° rotation. In contrast, at 2 K this has evolved markedly to two periods per 360° rotation.

est temperatures electrical conduction is dominated by these surface states, as their conductivity is much higher than that of the insulating bulk. Hence, for the samples measured here with two large, dominant flat faces (as depicted in Fig. 6.2), we can conclude that a model comprising the presence of surface-dominated conduction for $T \lessapprox 6$ K, and

bulk-dominated conduction at elevated temperatures, very well captures the symmetry evolution observed in the ADMR data as a function of temperature for $FeSb_2$ (and indeed for SmB_6).

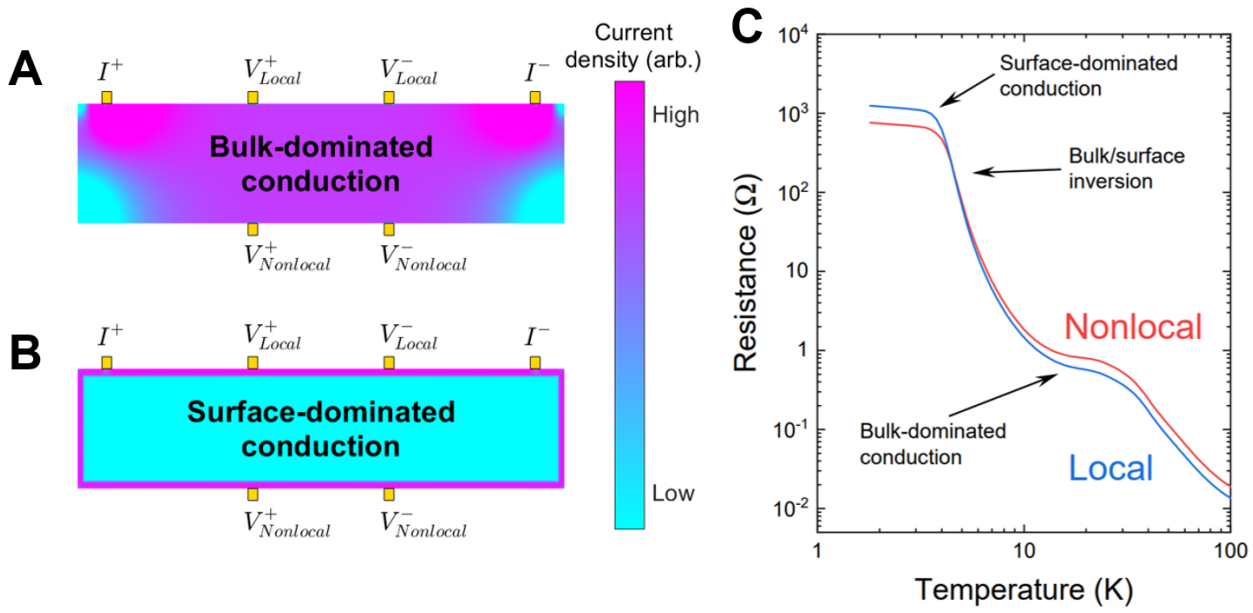

Fig. 6.4. Bulk/surface conduction inversion. Finite element simulations of the current density distribution for electrical transport through **A**, bulk-dominated channels, and **B**, for surface-dominated conduction. Simulations were performed in collaboration with colleague N. J. M. Popiel. **C**, Local and non-local 4-wire electrical transport measurements performed on an $FeSb_2$ single crystal. Current and voltage leads were attached as per the configurations indicated in (A) and (B) respectively. At high temperatures the non-local resistance is greater than the local resistance, as expected for simple bulk conduction. However, at low temperatures the converse is true, with the local resistance exceeding that of the non-local resistance, implying the domination of surface conduction.

6.2.3 Nonlocal resistance inversion

To further probe the character of low-temperature electrical conduction in $FeSb_2$, a nonlocal resistance study was undertaken. Previously, an inversion between local and nonlocal

electrical transport measurements upon cooling to the resistivity plateau was taken as a key piece of evidence in support of metallic surface state formation in SmB_6 [34, 70]. In the general case of electrical conduction through a section of bulk 3D conductor, electrical transport is expected to take place predominantly through the bulk of the material, as indicated by the charge density distribution depicted in Fig. 6.4A. However, for a sample cooled to $T \lessapprox 4$ K, the surface state model predicts that band hybridisation will cause these bulk conduction channels to become strongly gapped out as the surface state forms. This results in electrical transport being constrained almost entirely to the metallic surface of a sample (Fig. 6.4B). By performing four-wire resistance measurements of local and non-local configurations, as explicated by Figure 6.4, the applicability of this bulk/surface model to $FeSb_2$ may be investigated, and compared to the excellent correspondence previously found for such measurements in SmB_6 [34, 70].

Fig. 6.4C shows the measured electrical resistance of an $FeSb_2$ crystal for local (blue curve) and nonlocal (red curve) wiring configurations. At elevated temperatures ($T \gg 4$ K) the resistance of the non-local transport channel is greater than the local channel, as expected by simple geometric resistivity arguments for bulk conduction. However, for $T \lessapprox 5$ K the reverse is true, with $R_{\text{local}} > R_{\text{non-local}}$. This crossover occurs just before the resistivity plateau, over the same temperature range as the Hall effect peak in Fig. 6.1. Such a remarkable observation would be difficult to reconcile within a bulk impurity-band picture, or even with an elaborate low-temperature highly-anisotropic conductivity model. However, these observations may be easily explained by the surface state picture putatively applied to very similar observations in SmB_6 [34, 70], and thus provide compelling evidence that the same phenomenon is occurring in $FeSb_2$.

Furthermore, the fact that the local/non-local resistance inversion should occur over the same small temperature range (approximately 4 to 6 K) as the peak in the Hall coefficient, the opening of the resistance plateau, and the magnetoresistive symmetry evolution, each in concurrence with previous reports on SmB_6, gives strong confidence that these observations all point to the same correlation-driven surface state mechanism, previously investigated in the case of SmB_6, also being present in $FeSb_2$.

6.3 Electrical mobility and carrier density measurements

Given the multitude of evidence indicative of $FeSb_2$ possessing metallic surface states at low temperatures presented in section 6.2, a study of the electrical properties of the low-temperature conduction in $FeSb_2$ was subsequently undertaken. This involved determining the electrical mobility and carrier density through utilising the three difference wiring configurations of Hall-bar, van der Pauw (vdP) and Corbino disc geometries.

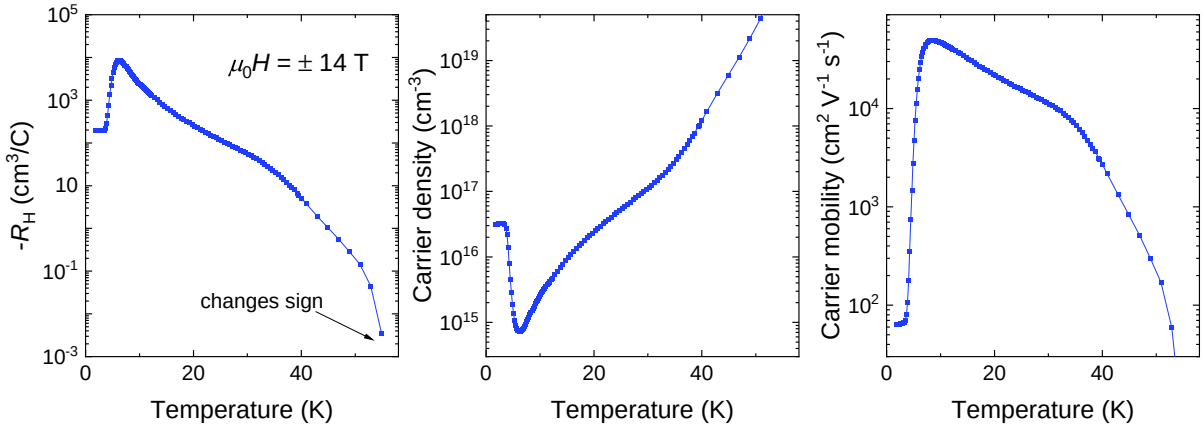

Fig. 6.5. van der Pauw study of $FeSb_2$. Hall coefficient (left), carrier density (centre) and carrier mobility (right) of an $FeSb_2$ single crystal as inferred from utilising a vdP measurement geometry and eqns. 4.2 & 4.3. Note that the sign of the Hall coefficient (R_H) indicates electron-dominated transport below ≈ 50 K. It should be stressed that, at low temperatures (where surface conduction dominates), the vdP method does not yield physically consistent quantitative results, for reasons discussed in the text.

Figure 6.5 shows results obtained from a vdP wiring setup of an $FeSb_2$ single crystal using eqns. 4.2 & 4.3. A peak in the magnitude of the Hall coefficient is observed around 6 K, in concurrence with the Hall-bar data presented in Fig. 6.1B. The carrier density is seen to decrease with decreasing temperature over the temperature interval of 10 K < T < 50 K. This is as would be expected in the case of a typical semiconductor, like silicon [205]. However, a remarkable feature of this dataset is that, at the lowest temperatures, the computed carrier density suddenly increases by over an order of magnitude, before plateau-

ing down to the lowest accessed temperature of 1.8 K. Notably, this occurs whilst the calculated carrier mobility abruptly decreases in magnitude.

For the carrier density to sharply increase on cooling to the lowest temperatures is contradictory to the conventional expectation one would have for a typical semiconducting or insulating material, whereby carriers are assumed to be thermally activated across some indirect band gap(s) and hence, upon cooling to the lowest temperatures, the carrier concentration decreases [205–207]. It is difficult to explain such an observation within some impurity-band model, as was previously invoked in attempt to describe the presence of the anomalous resistivity plateau in SmB_6 [208, 209], as firstly they should be frozen out at these low temperatures, and secondly they would not then be expected to plateau as $T \rightarrow 0$ K. However, within the interpretation of the formation of a metallic surface state, the data is well understood – to be considered *metallic*, the surface state by necessity must posses a large number of carriers that are able to partake in electrical conduction. Hence, an increase in the calculated carrier concentration upon the formation of a metallic surface state is well accounted for in this model.

6.3.1 Corbino disc measurements

However, the manner in which both bulk and surface conductivity contributions are coupled together in Hall-bar and vdP measurements complicates a quantitative analysis of the carrier density and mobility. This is because the two contributions are difficult to delineate, with the required geometric factors specific to the exact dimensions of the surface itself being difficult to quantify owing to possible imperfections through e.g. subsurface cracks that would increase the overall surface area of the surface state. Therefore, several recent studies on SmB_6 have employed a Corbino disc geometry to undertake inverted resistance measurements [174, 175, 210–212]. Utilisation of the Corbino geometry [173] is advantageous in the instance of investigating a metallic surface state as one effectively sets up a 2D Faraday cage on the surface of the material - hence the bulk (insulating) and surface (metallic) components can, in principle, be electrically isolated from each other,

allowing for a rigorous quantitative examination of the surface state's electrical conductivity to be undertaken [174].

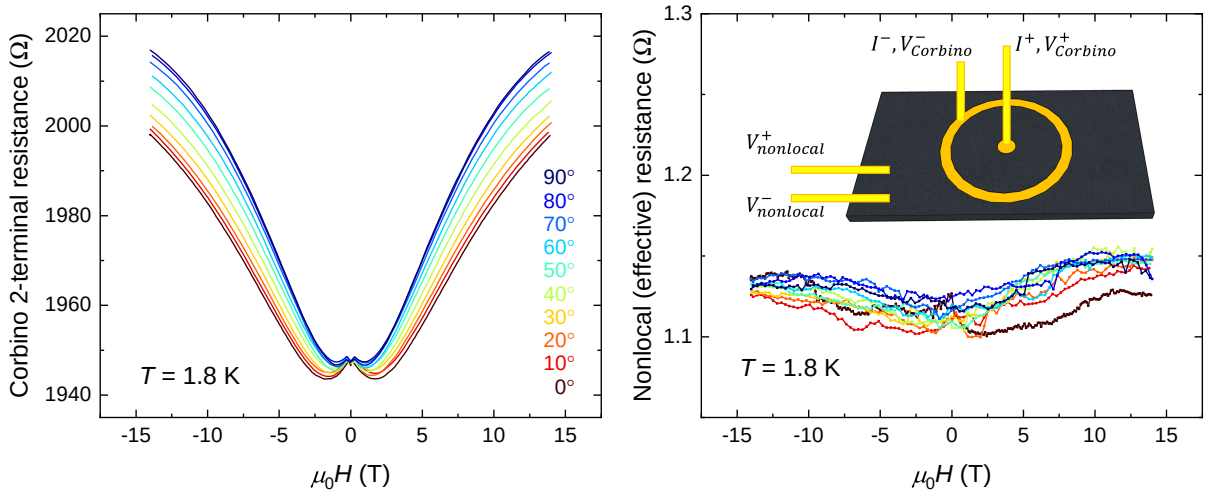

Fig. 6.6. Corbino disc measurements on $FeSb_2$. *Left:* 2-terminal Corbino disc measurements on the (110) face of an $FeSb_2$ single crystal. A dc excitation current of 10 μA was applied at a temperature of 1.8 K. *Right:* Nonlocal voltage outside the Corbino disc, recorded simultaneously to the local measurement. Colours correspond to the same angles as in the left panel. *Inset:* Respective wiring configurations for the Corbino disc and nonlocal channel.

Figure 6.6 shows local and nonlocal Corbino disc measurements on the (110) face of an $FeSb_2$ sample. A small dc excitation current of 10 μA (well within the positive differential resistance regime, as shall be discussed in section 7.2) was applied at a constant temperature of 1.8 K. The sample was rotated in-situ, with 0° corresponding to magnetic field aligned parallel to the plane of the disc, and 90° perpendicular to it. The Corbino resistance exhibits a clear dependence on the angular alignment of the magnetic field,

[2]Note that the nonlocal channel yields an *effective* resistance assuming that a 2D Faraday cage is established on the metallic surface state inside the Corbino disc, hence the magnitude of the current at the nonlocal voltage contacts is not well known; for the purposes of this figure the excitation current of the Corbino disc has been (somewhat naïvely) inserted into $V = IR$, yielding an unreasonably low resistance value for the bulk of order 1 Ω. However, it is the comparison of the qualitative angular magnetoresistance behaviours of the two channels that is of primary importance in this discussion.

unlike the effective resistance of the nonlocal channel, which exhibits no clear angular correspondence within the experimental resolution of the measurement. [2]

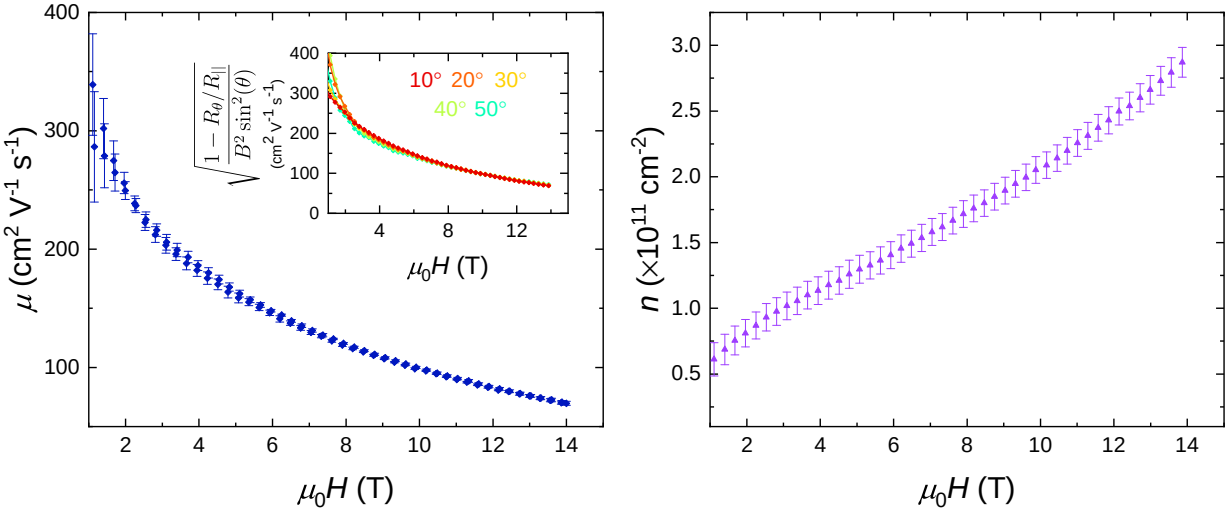

Fig. 6.7. Carrier mobility and density consistent with a 2D surface state. *Left:* Carrier mobility, μ, as a function of applied field strength, computed from the data presented in Fig. 6.6. Error bars were calculated as the standard deviation of averaging over several angles. *Inset:* Data for several angles as labelled. At high fields, they collapse very well on top of each other, in exactly the manner expected for a 2D surface state (with a $\frac{1}{\sin\theta}$ dependence as per eqn. 4.8). *Right:* Carrier density, n, over the same field interval as plotted for μ. The magnitude of n is several orders of magnitude lower than that observed by the vdP method in Fig. 6.5. Here the error bar calculation was dominated by uncertainties in the geometrical dimensions of the Corbino disc – for μ the dominant contribution was the reciprocal field term diverging at low field, hence the data are truncated below 1 T.

Figure 6.7 shows the carrier mobility, μ, and concentration, n, computed from the Corbino disc magnetoresistance data (Fig. 6.6) using eqns. 4.6 & 4.8. That the Corbino disc magnetoresistance curves should exhibit such a strong dependency on the magnetic field tilt angle, in notable contrast to the nonlocal channel, but should then collapse extremely well onto a single curve in the inset to the mobility plot when multiplied by the $\frac{1}{\sin\theta}$ term of eqn. 4.8, adds yet further confidence to the 2D metallic surface model of $FeSb_2$, in addition to that presented in section 6.2.

6.3.2 Quantitative evaluation of $FeSb_2$ surface state characteristics

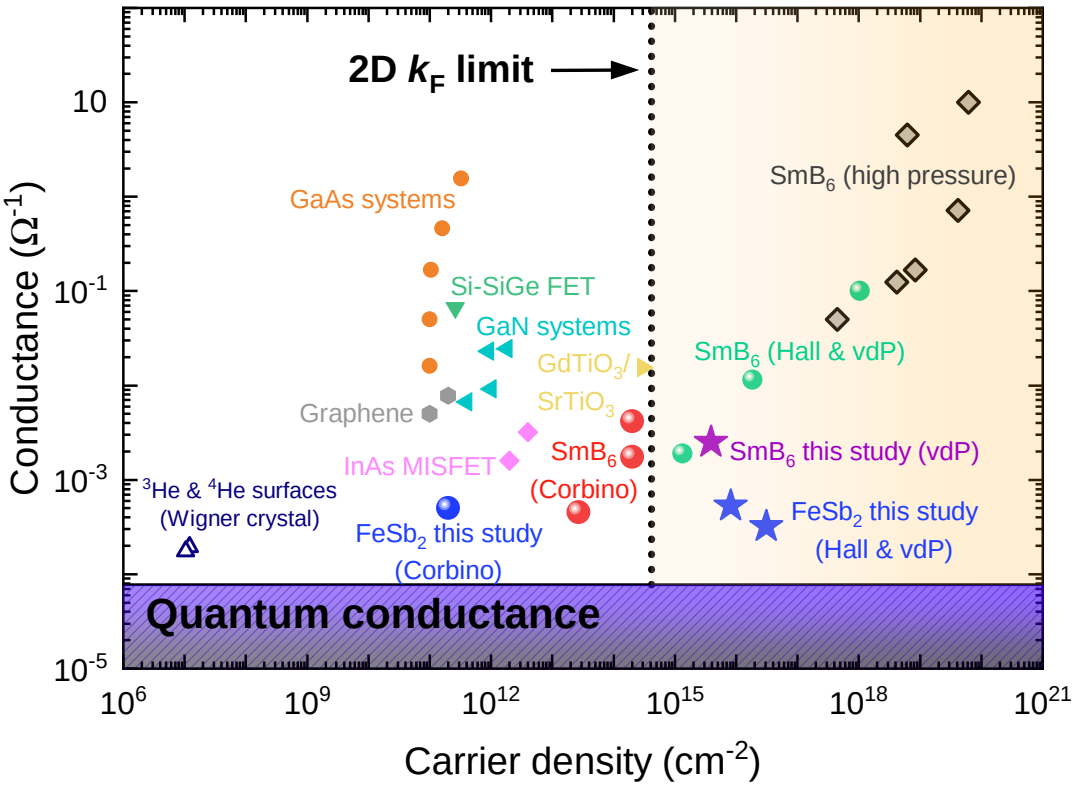

Fig. 6.8. 2D carrier densities. Reported carrier concentrations and conductances for various 2D systems. Prior SmB_6 results from Hall-bar and van der Pauw (vdP) measurement configurations at ambient pressure (green dots) and high pressure (grey diamonds) yield strikingly different values to Corbino disc measurements (red dots). Hall-bar and vdP measurements of $FeSb_2$ (blue stars) give similar carrier density values to measurements by the same techniques on SmB_6, but importantly they strongly disagree with the Corbino measurement (blue dot). The shaded region indicates the quantum conductance limit, while the dotted line denotes the maximum carrier density that can be contained within a single band in a 2D Brillouin zone. Reported values for SmB_6 are taken from refs. [36, 70, 175, 210, 211, 213–215], with values for other 2D systems from refs. [216–224].

Figure 6.8 shows the conductance versus carrier density for $FeSb_2$ measured by the Corbino disc method (Figs. 6.6 & 6.7), by the vdP method (Fig. 6.5), and by the Hall-bar

method, along with values for SmB_6 obtained by the vdP method (both computed from the Hall data presented in Fig. 6.1). Various other 2D systems are included, estimated by employing either classical (Drude) or semi-classical (Boltzmann) transport models, with data from refs. [70, 175, 215] and references therein. One obvious feature of note is the good similarity between Hall and vdP quantities extracted for $FeSb_2$ (blue stars) – yet their marked disagreement with the Corbino result (blue dot) by several orders of magnitude. A comparison of the literature data for SmB_6 likewise shows a much lower value of n for Corbino results than the other wiring configurations. Despite strong evidence in favour of low-temperature surface-dominated conduction, one may naïvely be puzzled that, with the exception of the Corbino results, each of these studies yielded carrier densities considerably in excess of the theoretical single-band limit that can be contained within a 2D Brillouin zone.

However, while the Hall-bar and vdP methodologies can accurately measure transverse conductivities of topologically trivial 2D materials, in the case of a 3D TI such measurements are complicated due to each side of the sample also having a 2D surface state, thereby electrically connecting the top and bottom surfaces by surrounding them with an effective metallic shell. Hence, the faces normal to the field are electrically shorted by this edge channel, thereby lowering the measured transverse voltage across the sample, giving carrier density values much larger than the true concentration on the 2D surface state. [3]

However, recent SmB_6 Corbino disc measurements have addressed this problem [174, 175, 210]. As discussed previously, through sourcing current between the concentric (inner) circle and (outer) annulus of a Corbino disc, an effective 2D Faraday cage is created on one single face of the sample, thereby excluding any edge contributions. These measurements (Fig. 6.8 red dots) have yielded physically consistent values for 2D carrier densities and mobilities [175] – as is also the case established here for $FeSb_2$. As this

[3] Note also that for a robust 3D TI, sub-surface cracks would also present additional metallic conduction channels, as any surface termination requires topologically protected surface state formation. Any such cracks or small surface defects may thereby provide additional surface state area than naïvely calculated by only considering the bulk sample geometry, which in turn would also increase the (incorrectly) calculated value of carrier density from performing Hall-bar and/or vdP studies.

technique is not sensitive to the sign of the charge carriers, but only their overall concentration, it also addressees the ambipolar surface conductivity predicted for correlated TIs [225], which may further complicate Hall-bar and vdP measurements if both electrons and holes are contributing to the surface conduction. Thus, the Corbino technique is therefore considerably more effective at quantitatively determining the electrical transport properties in 3D TI candidates such as $FeSb_2$ and SmB_6 [174, 175, 210].

The quantitative contrast between carrier densities obtained for SmB_6 and $FeSb_2$ from Corbino measurements, compared with those derived from Hall-bar and vdP studies, point quite strongly in favour of the presence of non-trivial topology. While it is possible that multiple-band inversion layers can have carrier densities above the single-band limit, this is not possible by the orders of magnitude observed here; nor, by similar arguments, are simple polarity-driven mechanisms likely[4]. However, the fact that Corbino-derived carrier densities specific to a single surface give physically plausible values, unlike Hall-bar and vdP measurements (that can have detrimental contributions from other surfaces), yields encouraging evidence in favour of topological surface state formation in these materials.

6.4 Comparative discussion of $FeSb_2$ and SmB_6

It should be remarked that a clear-cut consensus on SmB_6 being a topological Kondo insulator is yet to reach unanimous agreement throughout the community; although, recently that appears to be nearing [34]. That these measurements on $FeSb_2$ presented here yield a plethora of striking similarities with SmB_6 offers the exciting possibility that, should SmB_6 indeed be shown to possess metallic surface states owing to non-trivial topology, then the surface states on $FeSb_2$ most likely share that same origin.

An open question concerns the connection between the surface and bulk properties – with both of these materials exhibiting unconventional quantum oscillations in their

[4]For the top and bottom surfaces normal to the field to be shorted by polarity-driven surface states, all sides of the sample would have to also exhibit metallic surface states. While this has previously been

insulating bulk, and low mobility metallic surface states that do not exhibit the SdH effect up to the highest accessible magnetic field strengths. It has been proposed that non-trivial bulk topology may be a necessary prerequisite for the manifestation of insulating quantum oscillations in the case of SmB_6 [114] – which, if true, may help to explain the strong similarities between these two materials' metallic surfaces and insulating bulks.

Studies on SmB_6 into what physical features are fundamental properties required for the manifestation of the (putatively topological) surface state, and what features are not relevant, have been severely hampered by drastic differences between sample preparation methods [34]. Samples grown in aluminium flux are reasonably easy to produce, however the presence of aluminium inclusions, inhomogeneous growth rates of different crystalline facets, and contamination from the melt container, have led to notable inconsistencies in observed properties between different research groups [226]. The presence of small quantities of rare-earth impurities, such as gadolinium, can have a pronounced effect on the physical properties [227] at the low temperatures where the surface state forms, and the purification of elemental lanthanides from extraneous impurities of other rare-earth contaminants is notoriously difficult.

Higher purity SmB_6 samples may be obtained via the floating zone technique [168], as evidenced by these crystals' superior inverse residual resistance ratios, magnetisation, quantum oscillation and thermal transport properties [91]. Samples grown by this method have also exhibited some of the most compelling ARPES evidence for a topologically non-trivial nature of the surface state [228]. However, this method is considerably more difficult to perform than flux growth, with the high melting point of SmB_6 requiring the use of mirror furnaces to reach temperatures approaching $\sim$ 3,000 K [168]. Furthermore, the attainment of such high temperatures increases the likelihood of introducing samarium vacancies, which have also been reported to be a significant variable factor in the correlated electronic properties of this material [229]. This plethora of variation in physical properties between differing growth batches and sample preparation methodologies of SmB_6 has hampered the identification of what constituent properties

explored in the case of SmB_6 [34], the orthorhombic structure of $FeSb_2$ makes it much less likely that such an effect would be observed in this system.

are prerequisite to the development of the correlation-induced surface state.

$FeSb_2$, by contrast, has a much lower melting point of just over 1,000 K. This makes the acquisition of high-purity samples much more accessible through use of the chemical vapour transport (CVT) method, such as for the crystals investigated in this study. The CVT method, like the floating zone method, is immune to extraneous substitutive impurities from a crucible origin, or from flux inclusions; importantly, the considerably lower temperatures involved significantly minimise the probability of introducing vacancies, dislocations, or other sources of crystalline disorder that higher temperature procedures suffer from. Hence, obtaining excellent purity $FeSb_2$ crystals is much more realisable for a number of experimental research groups than is the attainment of similarly high quality SmB_6.

Therefore, given the striking similitude in low-temperature surface state properties between $FeSb_2$ and SmB_6, an exciting possibility lies in the identification of $FeSb_2$ as a model *d*-electron analogue of SmB_6, with extremely similar low-temperature behaviour, but with chemical properties that make the attainment of pristine high-purity specimens significantly easier to realise. Complementary measurements, such as spin-resolved ARPES and scanning tunnelling microscopy, are urgently called for in order to further investigate the potential of a topologically non-trivial origin of these metallic surface states.

6.5 Summary

This chapter presented a suite of electrical transport measurements performed on $FeSb_2$. Evidence indicative of surface-dominated conduction at low temperatures was observed from a variety of sources, including the observation of an anomalous low temperature resistivity plateau, an evolution of magnetoresistive rotational symmetry on cooling, an inversion between local and nonlocal transport channels, and a quantitative disagreement between Corbino measurements with Hall-bar and van der Pauw results of several orders of magnitude. These observations are strongly indicative of the presence of a metallic surface state hosted by $FeSb_2$ at low temperature. Notable similarities with the putative topological Kondo insulator candidate SmB_6 were compared and contrasted, with the temperature profile of surface state formation in $FeSb_2$ found to be remarkably similar to that observed in SmB_6. It is therefore very likely that whatever microscopic mechanism is at work in manifesting low temperature surface dominated conduction in SmB_6 is also at work in $FeSb_2$.

7

Non-Ohmic conduction and associated electrical transport phenomena in $FeSb_2$

The most beautiful thing we can experience is the mysterious. It is the source of all true art and science.

– Albert Einstein

In this chapter, a series of current-dependent electrical transport studies on $FeSb_2$ are presented. At low temperatures, strongly non-Ohmic resistance behaviour is observed, with a negative differential resistance regime present for high excitation currents. This is in common with previous reports on the topological Kondo insulator candidate SmB_6. Importantly, these effects are shown not to be caused solely by Joule heating, but must involve some other mechanism(s) that are yet to be well understood. The chapter concludes with the evaluation of some anomalous high field electrical transport data that exhibits quanitsed magnetoconductance signatures present in the highly unconventional high current, low temperature regime of this material.

7.1 Introduction

Ohm's law states that the potential difference across a section of electrically conducting material is equal to the product of its resistance and the magnitude of the applied current [230]. This holds true for simple metals, such as copper or silver. However, there are numerous materials wherein, under certain conditions, $V \neq IR$. For example, in type-II superconductors dissipation caused by vortices can give rise to non-Ohmic electrical conduction [231]. In the case of a p-n junction, the regimes of forward conduction and reverse breakdown follow markedly different *I-V* dependencies [232]. However, in each of these cases the differential resistance in never negative - that is, $\mathrm{d}V/\mathrm{d}I < 0$ is not observed.

7.2 Non-Ohmic current-dependent phenomena

7.2.1 Negative differential resistance

Negative differential resistance in SmB_6

In 2012, Kim *et al* [233] reported negative differential resistance in SmB_6, whereby at low temperatures and high excitation currents the measured voltage across a sample *decreased* with increasing current (Fig. 7.1). Subsequent studies showed that the negative differential regime (NDR) was acutely dependent on the frequency of the ac drive current, and that remarkably, upon the application of small dc bias currents, ac output voltages up to 30 MHz were attained, with the frequency of the response scaling inversely with the sample size [234, 235]. These results pointed to complex transient dynamics at play, with an anomalous intrinsic capacitance between the insulating bulk and metallic surface state posited to be responsible.

Recently, a different collaboration has reproduced and extended these current-dependent results on SmB_6 with an impedance spectroscopy study [236]. Interestingly, the authors report that unlike the simple models assumed in refs. [234, 235], it is not possible to ex-

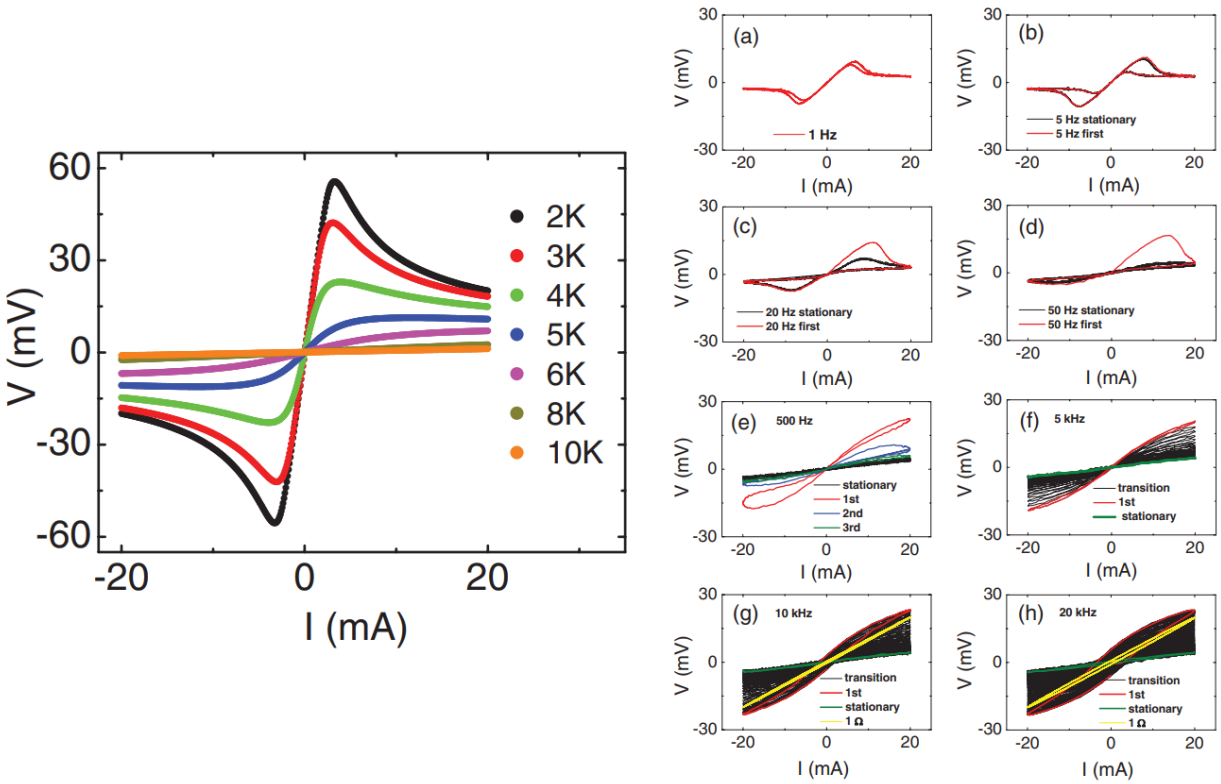

Fig. 7.1. Non-Ohmic conduction reported in SmB_6. *Left:* Voltage, V, as a function of current, I, at various temperatures. Negative differential resistance (a downward slope in V vs I) is observed at high currents for $T < 5$ K. *Right:* Panels at different ac excitation frequencies between 1 Hz to 20 kHz, showing pronounced frequency-dependent behaviour. These measurements were taken on a single crystal of flux-grown SmB_6. Figure adapted from [233] and reproduced with permission. Copyright (2012) by the American Physical Society.

plain the data solely with resistive and capacitive components alone, but instead they show that the inclusion of an inductive component(s) is also necessary in order to fully explain their dataset by way of analogy with an *RLC* circuit. While the model of insulator-metal capacitive coupling is somewhat intuitive to visualise, with charge having to tunnel from one to the other, this new proposal poses the interesting question as to what constituent part of the surface/bulk system could somehow be acting inductively. The

authors of ref. [236] give no indication of what physical aspect of SmB_6 they believe to be playing the role of an electrical inductor, and it is not immediately apparent how a metallic surface state could effectively be storing magnetic field in such a manner. The bulk is therefore more likely to be the source of this intriguing intrinsic inductance – perhaps by hosting soliton-like magnetic objects – which provides a potential a bridge from the electrical behaviour of the SmB_6 surface state to the unconventional insulating properties of the bulk. More work to better understand these dynamics within SmB_6 is therefore urgently called for.

Comparison of SmB_6 and $FeSb_2$ NDR behaviour

Figure 7.2 shows the potential difference across SmB_6 and $FeSb_2$ single crystals as a function of ac excitation current, at a frequency of 0.3 Hz in order to minimise the hysteretic effects at high current and high frequency reported in ref. [233]. The SmB_6 data reproduces well the results previously reported in ref. [233] (Fig. 7.1). Qualitatively, the same set of measurements on $FeSb_2$ are, remarkably, almost identical in character. Both materials show a sharp peak in voltage as a function of current, before going on to exhibit a NDR up to the highest applied currents (in this case of 5 mA amplitude). Quantitatively, the main difference is that at 2 K $FeSb_2$ crystals typically exhibit greater resistance than those of SmB_6 (for similar size and contact placement for both materials), by up to a couple of orders of magnitude (as indicated by the [effective] resistivities plotted in Fig. 6.1).

7.2.2 Transient dynamics

Given the strong similarities between the two materials as depicted in Fig. 7.2, in order to evaluate if the transient effects observed in SmB_6 (Fig. 7.1) are also common across the two materials, a similar time-dependent study of the *I-V* response of $FeSb_2$ was carried out. Figure 7.3A shows the first 25 ms of voltage signal measured across an $FeSb_2$ sample after a sinusoidal excitation waveform of frequency 20 kHz was sourced through the sample. The same data is plotted versus current in Fig. 7.3B. The initial amplitude of the

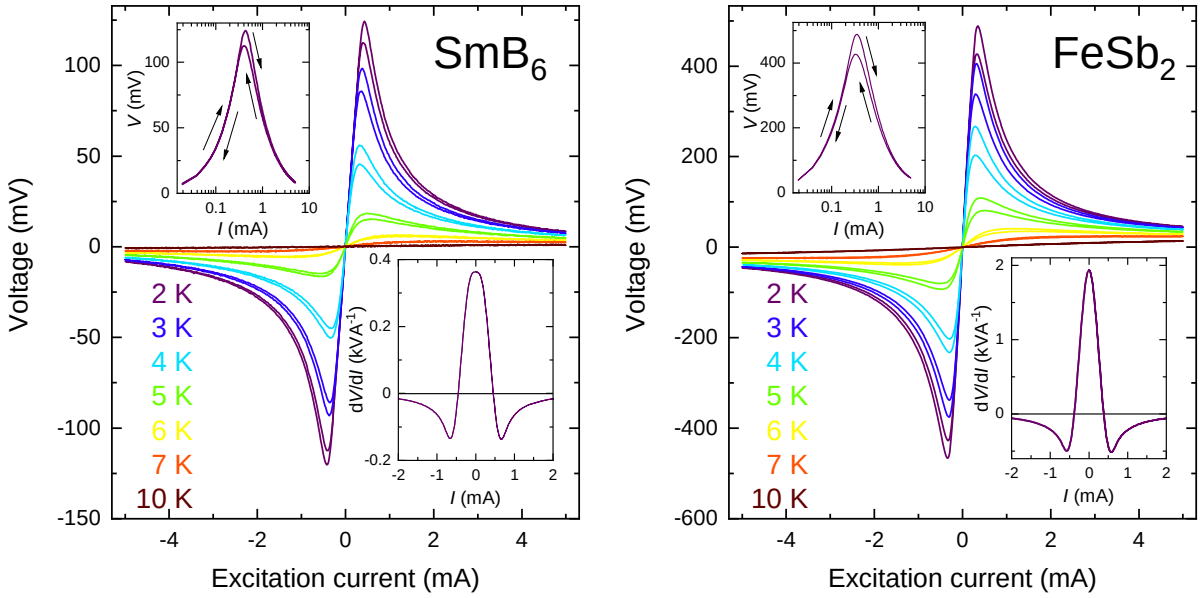

Fig. 7.2. Negative differential resistance. Current-voltage behaviour of SmB_6 (left) and $FeSb_2$ (right), at incremental temperatures. Both materials exhibit remarkably similar behaviour. Upper insets show the 2 K curves of the main panel on a logarithmic current scale; arrows denote the direction of the current sweep, exhibiting hysteresis in the vicinity of the peak in voltage. Lower insets show derivatives of the 2 K curves; the negative differential regime (NDR) is defined as the high-current region in which $\mathrm{d}V/\mathrm{d}I < 0$. All curves were obtained at an ac drive frequency of 0.3 Hz, measured by a lock-in technique.

voltage response (blue curve) is seen to attenuate rapidly, with strong hysteresis observed in the *I*-*V* plot. Similar behaviour is also observed on reducing the frequency down to 500 Hz (Fig. 7.3C&D). These results are very similar with those previously reported in SmB_6 (Fig. 7.1) [233].

Interestingly, a pronounced difference is observed in the time-dependent voltage signal for a 5 Hz ac excitation current at a temperature of 4 K (Fig. 7.3G) compared to that at 0.7 K (Fig. 7.3H). Despite sourcing a clean sinusoidal current excitation, the voltage profile at 4 K is seen to be anomalously shaped, with the peak of each waveform slowly decaying before going rapidly to the minimum, slowly decaying in amplitude again then return-

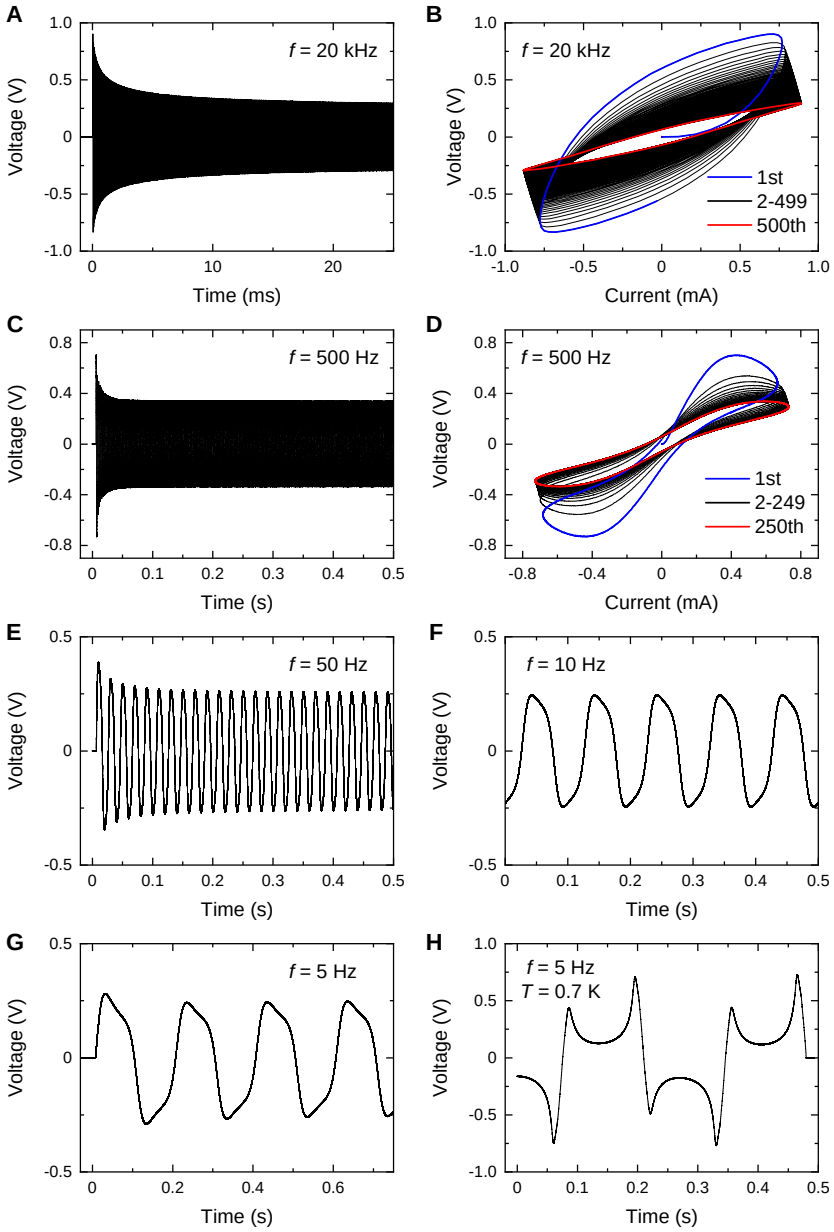

Fig. 7.3. Transient frequency-dependent effects. Frequency dependence of the transient response. All data are measured at 4 K, except **H** at 0.7 K. Data were acquired by a Yokogawa DL 850E digital acquisition system.

ing to the peak and repeating. This behaviour (in SmB_6) was addressed in ref. [233] as representing an anomalous capacitance, as the phase shift between the current and voltage channels cannot be described merely by some resistive model but instead requires the presence of some (virtual) capacitive component. This effect was posited to involve a capacitive coupling between the bulk insulator and the metallic surface state [233–236].

At 0.7 K, the time-dependent voltage profile of $FeSb_2$ clearly shows a considerably different, highly anomalous behaviour. That the voltage profile should evolve so markedly over this temperature interval implies that, if the bulk-surface capacitive coupling model invoked for SmB_6 in refs. [233–236] should also hold true in the case of $FeSb_2$, then the strong gapping out of bulk conduction down at the lowest temperatures appears to be strongly linked to the strength of the capacitive response. More experiments, finely spaced in temperature and frequency, could be extremely useful in revealing how this relationship evolves, and hence place firmer constraints on physical models for the microscopic mechanisms responsible.

7.2.3 Discussion of the NDR origin

In electrical engineering, the attainment of an NDR usually requires the fabrication of complex components, such as tunnel diodes or vacuum tubes [237, 238]. Understandably, the observation of such effects in bulk materials, such as crystals of SmB_6 and $FeSb_2$, is rather uncommon. Of the materials that have been reported to possess an NDR, some have had this effect attributed to Joule heating effects [239, 240] while others are instead ascribed to be indicative of the melting of charge density wave (CDW) order [241–243]. No evidence for CDW formation in SmB_6 or $FeSb_2$ has been reported, however, aspects of a Joule-heating origin of the NDR have been explored [233–236].

An interesting comparison of the exotic *I-V* characteristics of SmB_6 and $FeSb_2$ can be made with $Ce_3Bi_4Pt_3$, an archetypal Kondo insulator [245, 246]. Figure 7.4 shows that, despite this material also exhibiting hysteretic current-voltage behaviour indicative of an anomalous capacitive component, no NDR is observed in this study [244]. Furthermore,

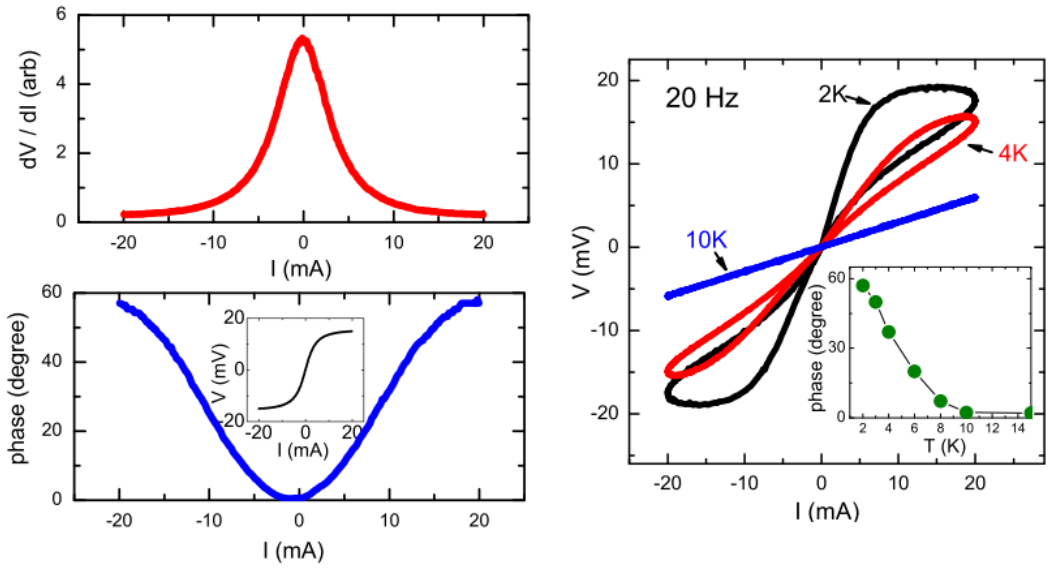

Fig. 7.4. *I-V* characteristics of $Ce_3Bi_4Pt_3$. *Left:* Differential resistance and phase angle of a $Ce_3Bi_4Pt_3$ crystal. No NDR is observed up to the highest applied current magnitude of this study, of 20 mA. *Right:* Lissajous plots of $Ce_3Bi_4Pt_3$ at 20 Hz. Anomalous self-capacitance is also present within this system. The inset shows the phase angle evolution in temperature. Figure reprinted from ref. [244], with the permission of AIP Publishing.

in another study that analysed the transient response of SmB_6, similar measurements performed on $Ce_3Bi_4Pt_3$ found no evidence of dc controlled ac signal oscillations down to their lowest measurement current of 1 K [234]. This was taken to imply that, in order to explain the *I-V* characteristics of SmB_6, although it may be possible to attribute the anomalous capacitance to be due to the presence of Kondo physics, the NDR is instead strongly indicative of the presence of a metallic surface state (as $Ce_3Bi_4Pt_3$ shows no evidence for surface-dominated low temperature conduction) [234, 244].

Effect of Joule heating

In ref. [244], the authors posit that simple Joule heating alone is insufficient to account for the hysteretic Lissajous curves obtained for $Ce_3Bi_4Pt_3$ (Fig. 7.4), but that instead some

form of memristive-like behaviour [247, 248] is caused by a virtual thermal impedance arising from the self-heating by some (as yet) unknown mechanism. In refs. [234, 235], the authors apply this concept of virtual thermal impedance to SmB_6, in tandem with the bulk/surface capacitive coupling framework. They write this model as:

$$\begin{aligned} CR_S\dot{I_S} &= I_0 - GI_S \\ C_H\dot{T} &= 2I_S^2R_SG - I_SI_0R_S - \gamma(T - T_B), \end{aligned} \tag{7.1}$$

where I_S and I_0 are the surface and total currents through the sample, respectively; C is the total (internal and external) capacitance; and $G = (R_S + R_B)/R_B$ where R_S denotes the surface resistance and the bulk resistance, R_B, is given by $R_B = R_B^0 \exp(-\Delta/T + \Delta/T_0)$. At temperature T_0, R_B^0 is the (equilibrium) bulk resistance. C_H is the heat capacity and γ is a temperature-independent rate of heat transfer through the leads [234, 235].

The authors of refs. [234, 235] report good correspondence with this model, which predicts temperature and voltage oscillations offset by a phase difference of 90°, that are verified by experiment. They qualitatively view this as an initially cold sample being at a temperature sufficiently low enough for surface conduction to dominate. Heat is then applied (simply by $P = IV$), warming the system up to a temperature whereby the resistance decreases; hence, I^2R subsequently decreases, the sample cools, and the process repeats.

Ref. [236], meanwhile, in performing a more detailed impedance study of SmB_6, reports that this model only holds well for low frequencies. At high frequencies, they find that an inductive term is required to fully model the electrical response. They verify this on the results published in ref. [234], and show that their model correctly yields $LC \propto \omega^{-2}$, as expected by simple circuit theory [237].

The dc-tunable ac signal response experiments performed on SmB_6 in refs. [234, 235] are yet to be performed on $FeSb_2$, so a direct comparison of the model presented in eqn. 7.1 cannot be conducted. (A subsequent study to this effect is highly recommended by the

author.) However, a comparison of the high- and low-frequency data from Fig. 7.3 can still be performed, and then assessed against the question of whether a Joule-heating argument may be the sole cause of these anomalous *I-V* results in $FeSb_2$.

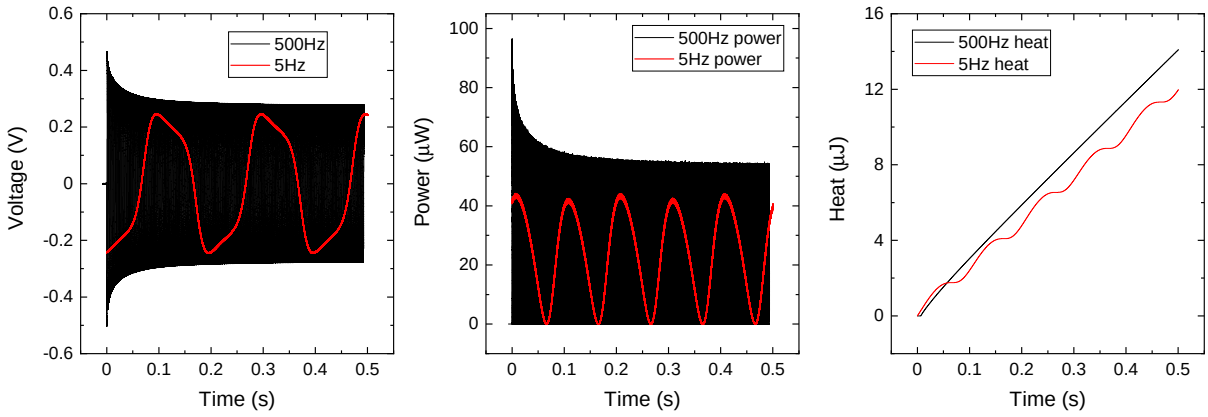

Fig. 7.5. Negligible effect of Joule heating on the transient response. Voltage (left), power (centre) and total heat applied (right) to the same sample of $FeSb_2$ for 500 Hz (black) and 5 Hz (red) excitation frequencies. All panels are plotted over an identical time interval.

Figure 7.5 shows the 500 Hz (black) and 5 Hz (red) data from panels 7.3C and 7.3G, respectively. The voltage amplitude of the 500 Hz trace is seen to decay markedly over the first 0.05 s of the measurement, before going on to continue decreasing (albeit more gradually) over the entire 0.5 s duration of the measurement. The 5 Hz trace, by contrast, shows no attenuation within the resolution of the measurement. Despite the 5 Hz trace actually experiencing more Joule heating over the initial 0.05 s of the measurement, it is the 500 Hz trace that drops in amplitude by over a factor of $1/4$ during this interval. This strongly suggests that Joule heating can be ruled out as the causal factor for the transient response observed in $FeSb_2$. Further detailed investigations into the character of the non-Ohmic conductance in $FeSb_2$, such as the dc controlled ac signals seen in SmB_6 [234, 235], and the SmB_6 impedance study recently reported in ref. [236], would add much greater insight into whether the models proposed thus far for SmB_6 also hold in the case of $FeSb_2$, or whether fresh thinking is required for this material.

Despite the above discussion arguing strongly against a Joule heating origin for the anomalous transient repsonse observed for high excitation frequencies and currents in $FeSb_2$, from these observations alone it cannot be ruled out as the source of the NDR. To better resolve that question, we turn to the application of magnetic fields.

7.3 Current-tuned magnetoresistive effects

7.3.1 Uniqueness of the low temperature, high current regime

Characterising current-tuned behaviour in temperature

To examine the response to applied magnetic fields of the anomalous *I-V* behaviour presented in the previous section, a suite of field-dependent measurements was undertaken. Figure 7.6 shows resistance versus temperature for several dc excitation amplitudes, from as low as 10 nA up to 100 μA (which for this sample is within the NDR). Identical temperature sweeps were performed in applied magnetic fields of 0 T, -14 T, and +14 T, with the dashed curves being the symmetrised combination of the ± 14 T data. This was performed in order to exclude any transverse (Hall) component contribution to the dataset, which can be considerable over this temperature range (Fig. 6.1).

Intriguingly, there is a notable difference between the in-field behaviour of the low and high currents examined here. For example, a visual inspection of the 10 nA (red) curves shows that the 14 T resistance is always greater than that in zero applied field, throughout the entire temperature range of the experiment. However, that is not true for the 100 μA (blue) curve which, at the lowest measured temperatures, exhibits a lower in-field resistance than for 0 T.

In order to further examine this effect, a comprehensive investigation into the magnetotransport dependence on excitation current was undertaken. Figure 7.7 shows a contour plot constructed from many individual magnetoresistance traces, taken at incremental

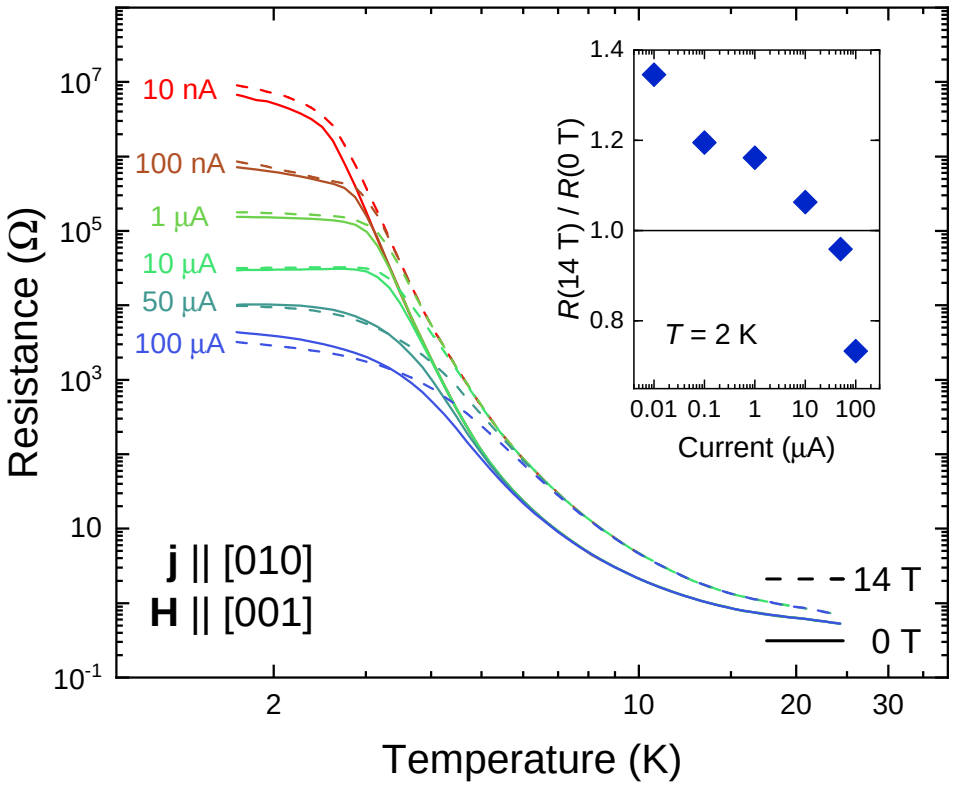

Fig. 7.6. Change of sign of magnetoresistive gradient tuned by excitation current. Solid curves show resistance as a function of temperature in zero applied magnetic field, for several dc currents between 10 nA and 100 μA as indicated, while dashed curves give the symmetrised magnetoresistance (measured at ± 14 T) for the same currents. For low currents, the 14 T resistance is always higher than that for 0 T – but at high currents the 14 T curves cross the 0 T curves at low temperature. *Inset:* ratio of the resistances at $|\mu_0\mathbf{H}|$ = 14 T and 0 T, as a function of current at T = 2 K.

currents and temperatures, on a different $FeSb_2$ sample. This figure was constructed in collaboration with colleague N. J. M. Popiel.

If the anomalous high current, low temperature electrical behaviour of $FeSb_2$ presented in section 7.2 were merely the result of Joule heating, then behaviour observed for high currents at low (measured) temperatures may in fact just be a reproduction of the low current behaviour exhibited at higher temperature, except with the effect of local

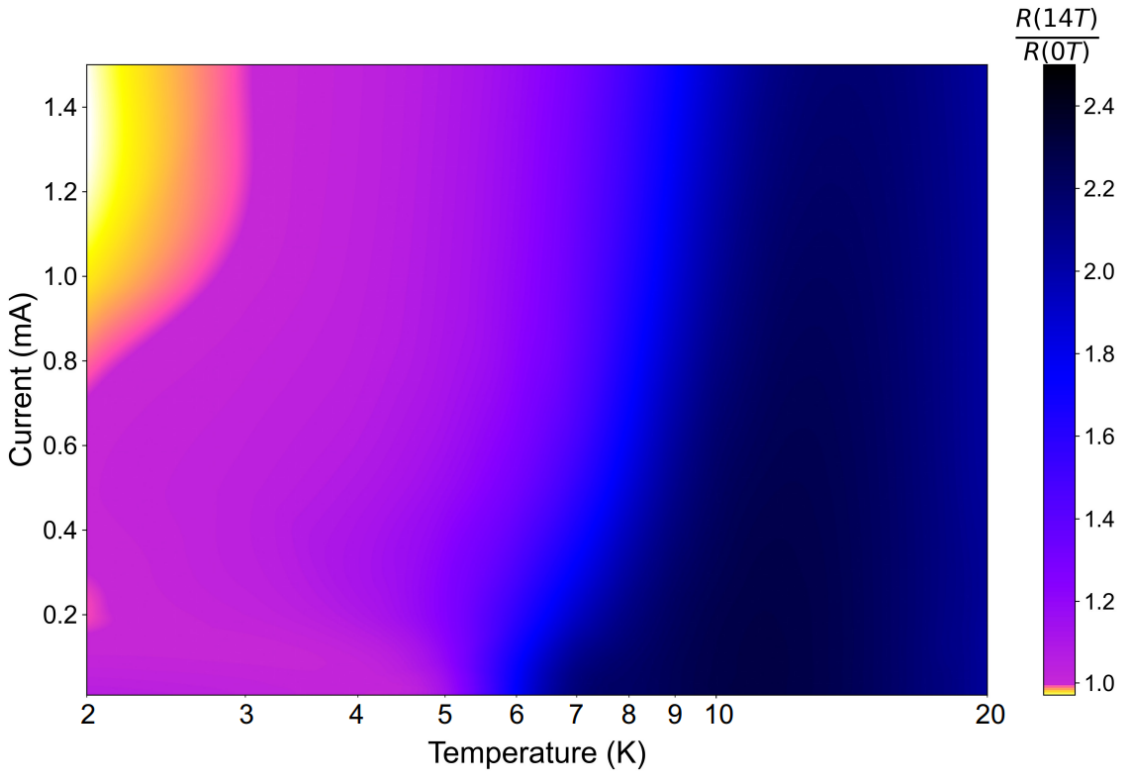

Fig. 7.7. Uniqueness of the low temperature, high current regime of $FeSb_2$. Contour plot of the magnetoresistive ratio of an $FeSb_2$ single crystal in fields of 14 T/0 T. The scale bar has been especially designed to sharply highlight $R(14\text{ T})/R(0\text{ T}) < 1$ (in yellow), which is observed only for the highest currents at the lowest temperatures.

heating to the sample perhaps not having been accurately taken into account in determining the temperature. Thereby, if such effects were caused simply by such a Joule heating argument, then one would expect to see the same effects (i.e. the response to a magnetic field) that are observed at low temperatures and high currents to also be occurring at high temperatures and low currents.

Fig. 7.7 shows conclusively that this is not the case. There is only one region of the plot wherein $R(14\text{ T})/R(0\text{ T}) < 1$; this occurs solely for high excitation currents at the lowest temperatures. Therefore, simple Joule heating arguments are unable to explain the *I-V* characteristics of this material at low temperatures, and simple models such as eqn. 7.1

are clearly insufficient in reconciling the current-controlled behaviour exhibited by $FeSb_2$ under the application of a magnetic field[1], as indeed are conventional models of electrical transport in the presence of an applied magnetic field [249–251].

Persistence of current-tuned magnetoresistance to high magnetic fields

To extend the investigation of this phenomenon to higher magnetic fields, a series of pulsed field measurements was performed. Figure 7.8 shows magnetoresistance traces up to 70 T, for various applied excitation amplitudes. Measurements were obtained in a ^{3}He insert thermally equilibrated with a ^{4}He bath pumped down to 1.4 K, in order to provide maximal cooling power. Data was acquired by a Yokogawa DL 850E digital acquisition system.

Again, a clear distinction between low and high current behaviour is observed, with a positive slope of magnetoresistance exhibited at low I, that then flattens out for increased I before turning to a clear negative slope at high I. This trend – of positive $\partial R/\partial(\mu_0 H)$ in the positive differential resistance regime, and negative $\partial R/\partial(\mu_0 H)$ in the negative differential resistance regime – is common to the three different $FeSb_2$ samples presented in Figs. 7.6, 7.7 & 7.8. These effects were also observed on several other samples (for brevity the results of which are not presented here); hence, it is very likely that these anomalous effects, that cannot be reconciled solely within a Joule-heating framework, are indeed intrinsic to $FeSb_2$, and thus necessitate a more rigorous theoretical explanation than those posited thus far for the case of SmB_6's NDR characteristics[2] in refs. [233–236].

Interestingly, both the lowest measured current of this high field study (20 μA, blue

[1] An interesting side note is that the vivid band of blue shown at ≈ 6 K in Fig. 7.7, which borders the large purple region, is likely characteristic of the opening of the metallic surface state. Note also that for this particular sample, the NDR is accessed only with somewhat higher currents than in the case of the samples in Figs. 7.6 & 7.8, of order a few hundred μA; the location of the peak in the *I-V* curve is found to vary somewhat sample to sample, but is generally in the range of a few tens of μA up to a few hundred μA.

[2] Note that no reports of SmB_6 exhibiting these anomalous in-field signatures have yet been reported – a comparative experimental study, of the same measurements presented here on $FeSb_2$, would likely be very useful in constraining possible models across both systems.

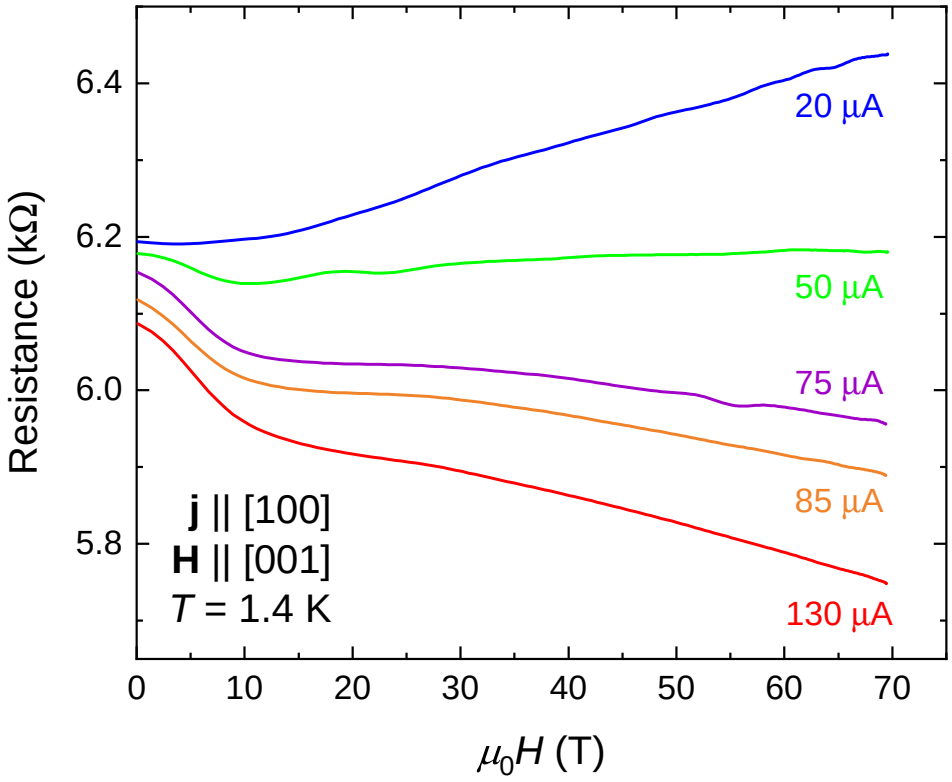

Fig. 7.8. Pulsed-field current dependence of $FeSb_2$. High-field magnetoresistance curves of $FeSb_2$ for various excitation currents measured in the 70 T magnet at HLD, Dresden. Current was sourced along the [100] direction, with field applied parallel to [001]. The dichotomy between high/low currents exhibiting positive/negative magnetoresistive gradients is seen to persist up to at least 70 T, with neither regime appearing to saturate at high field.

curve in Fig. 7.8) and the highest measured current (130 μA, red curve) show no signs of saturating as $\mu_0 H \rightarrow 70$ T. This implies that whatever mechanisms are dominating the respective low and high current behaviours are not fragile to time reversal symmetry breaking. Notably, as per the case of SmB_6 [34], despite the multitude of evidence presented above in favour of electrical conduction being dominated by a metallic surface state at this temperature, no SdH oscillations are observed up to 70 T. However, we should quantitatively consider the value of the carrier mobility extracted from Corbino measurements

in section 6.3.1, which yielded $\mu \sim 100$ cm^{2}V^{-1}s^{-1}. We can make a crude estimate for the magnetic field strength at which SdH oscillations should onset [175], as $\mu \cdot \mu_0 H_{\text{onset}} \approx 1$, i.e. $\mu_0 H_{\text{onset}} \approx 1/\mu$. Assuming $\mu \sim 100$ cm^{2}V^{-1}s^{-1} remains valid up to high magnetic fields, then $\mu_0 H_{\text{onset}} \approx 100$ T. Hence, it is unsurprising that no evidence of the SdH effect emanating from the metallic surface is observed up to the maximum field strength applied here of 70 T. It is interesting to note that, while the insulating bulk exhibits pronounced quantum oscillations in magnetisation at fields as low as ≈ 10 T (Fig. 5.5), no resistivity oscillations (of either a bulk or surface origin) are observed up to at least 70 T – underlining yet another similarity between $FeSb_2$ and SmB_6 [34, 91].

Simple tunnelling model

If we were to assume a simple tunnelling model for the *I-V* behaviour, whereby low currents are considered constrained to the metallic surface of the material, but higher currents are capable of tunnelling through to the bulk, this might qualitatively capture some of the observations reported here. For example, metals typically exhibit positive magnetoresistive gradients, due to additional scattering introduced through cyclotron motion [252], whereas Kondo insulators like $Ce_3Bi_4Pt_3$ exhibit negative magnetoresistive gradients owing to the breakdown of Kondo singlets as the Zeeman energy is increased [253].

However, this picture is likely too simple to really capture all that is happening. Firstly, at low temperatures the magnetoresistance of typical metals such as copper saturates for $\mu_0 H \approx 10$ T [254] - whereas here the 20 μA curve shows a linear, non-saturating response over the field interval 20 T $\leq \mu_0 H \leq$ 70 T. This strongly implies a full description must also incorporate the additional presence of some other effect(s), perhaps Abrikosov quantum linear magnetoresistance [255, 256]. Furthermore, regarding the possible explanation of negative magnetoresistive slopes as originating from the paramagnetic destruction of Kondo singlets, the question of whether $FeSb_2$ can be treated by the same 'Kondo insulator' frameworks of $4f$ materials like SmB_6 is still an open question [37]. Fresh theoretical impetus is urgently called for in attempt to reconcile the plethora of exotic electrical sig-

natures manifested at low temperatures by this material.

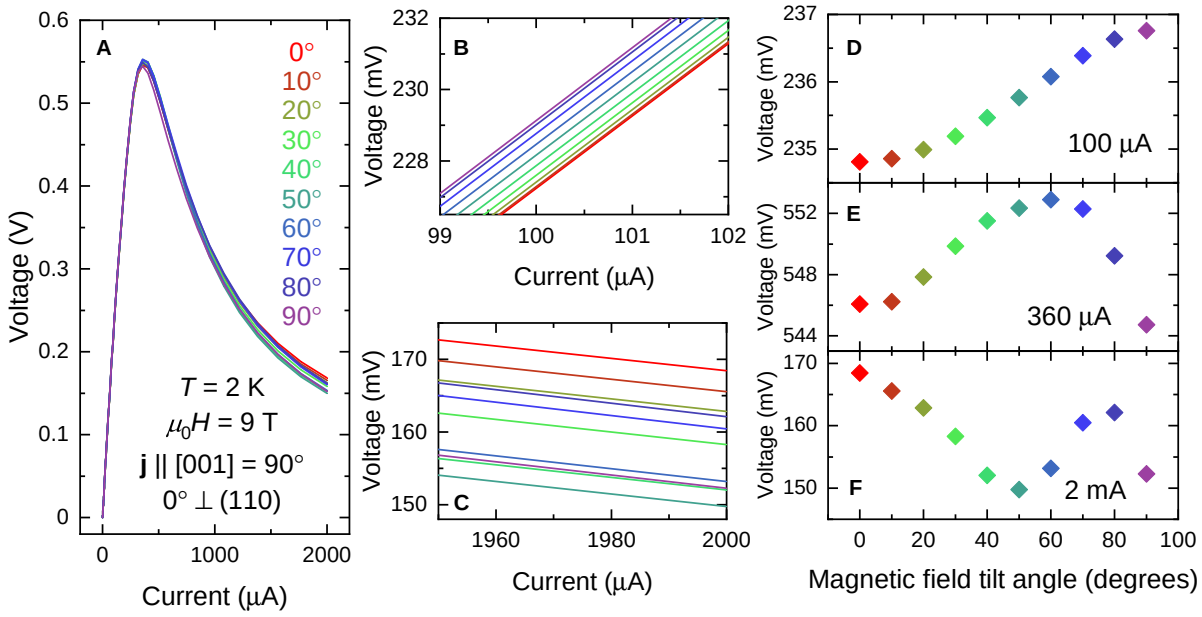

Fig. 7.9. Current-dependent rotational symmetry evolution. (**A**) *I-V* curve for dc excitations up to 2 mA at incremental 10° angles from **H** ⊥ (110) to **H** ∥ [001]. Current was sourced along the [001] direction, and all measurements were taken in an applied field of 9 T at 2 K. (**B**) Low-current and (**C**) high-current blow-ups of the data in **A**. (**D-F**) Voltage versus magnetic field tilt angle for excitation currents of 100 μA, 360 μA, and 2mA. For reference, **H** ⊥ (111) is located at 53.7°.

7.3.2 Characterising the anomalous high current behaviour in field

Rotational study

To further probe the characteristics of the anomalous *I-V* response of $FeSb_2$ in magnetic fields, a rotation study was performed. Figure 7.9 shows voltage as a function of dc excitation current for **H** aligned at incremental angles from **H** ⊥ (110) to **H** ∥ [001] ∥ **j**, where $\hat{j}$ is the unit vector in the direction parallel to that in which the current was sourced.

For this sample, the peak in V vs I is observed to occur for $I \approx 360$ μA. For currents below this, e.g. the range plotted in panel (**B**), a simple sinusoidal behaviour with respect to angle is observed, as explicated in panel (**D**). The sinusoid exhibits half a wavelength over the 90° rotation measured, hence for a full 360° rotation would be expected to yield two full oscillations, in excellent agreement with the results indicative of a metallic surface state in this temperature range presented previously in Figs. 6.2 & 6.3. We can therefore likely interpret the low current region of the *I-V* curve as being dominated by surface conduction.

Once more, we can see that simple heating arguments fail to capture the complexity of the data. If Joule heating were the dominant mechanism responsible for the formation of the NDR, then at high currents we would expect to reproduce the bulk symmetry measured at high temperatures and low current in Fig. 6.3, with one rotation per 360° (and hence a quarter of a wavelength over 90°). However, that is very much not what is observed - in panels (**C**) and (**F**) of Fig. 7.9, for rotation angle α in the range $0° \leq \alpha \leq 70°$, the data appears to indicate there would be a full wavelength of oscillation for the 90° span of rotation. However, the 80° voltage is lower than would be expected, and that at 90° is even lower in magnitude than that measured at 60°. Panel (**E**) shows that, right at the peak of the *I-V* curve, the high angles (80° & 90°) are beginning to deviate from the simple sinusoidal progression of panel (**D**).

This behaviour is highly puzzling, and hints further at the underlying complexity of the high current *I-V* effects in $FeSb_2$ uncovered in this dissertation. It appears that the 90° orientation (i.e. $\mathbf{H} \parallel [001]$) is the orientation for which the behaviour is most anomalous. To determine whether that may be due to the fact that $\mathbf{H} \perp \mathbf{j}$ in this orientation, or due to the [001] direction possessing anomalous magnetic properties as previously explored in section 5.6, is unclear from this dataset alone. Future studies, beyond the scope of those presented here, extending through more angles of rotation, and perhaps employing Corbino geometry to delineate surface and bulk contributions, would be most informative in guiding further evaluation of these anomalous features.

Transverse effects of high currents

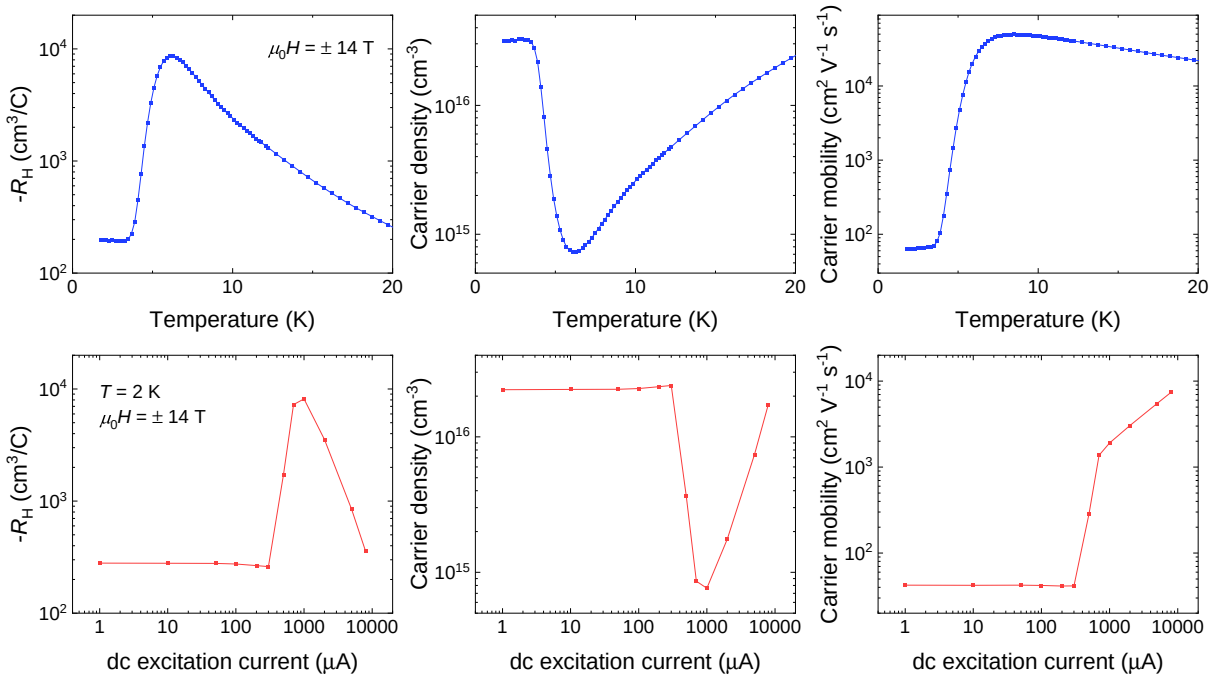

Fig. 7.10. vdP study extended to high currents. *Top:* Blue curves showing Hall coefficient (R_H), carrier density, and carrier mobility for 2 K $\leq T \leq$ 20 K. Data are the same as Fig. 6.5. As discussed in section 6.3.2, these results are not quantitatively valid for the lowest temperatures where surface conduction dominates. *Bottom:* Red curves showing the response of R_H, carrier density, and carrier mobility to the magnitude of excitation current, measured on the same sample as that of the temperature curves above. Symbols give individual data points; lines are as a guide to the eye.

Figure 7.10 shows the effect of current on R_H, μ, and n for incremental currents in the range 1 μA $\leq I \leq$ 8 mA computed through use of eqns. 4.2 & 4.3. For both R_H and n, the dependencies on temperature follow similarly to those on current, with a plateau for low temperatures/low currents, followed by an increase (decrease) in -R_H (n), followed by a subsequent decrease (increase) again at the highest plotted temperatures/currents. An examination of just these two variables in isolation may lead one to assume a Joule heating origin to these effects – however, an examination of μ shows that this is not viable.

Over the temperature domains where -R_H (n) decreases (increases), μ is also decreasing. However, under the application of high current μ is seen to rise sharply upon accessing the NDR, *and then continues rising up to the highest applied currents.* Thus, unlike for -R_H and n, μ shows a contradiction between the high temperature/high current behaviour. Thereby, once more there is another high current-induced phenomenon in the low temperature electrical transport of $FeSb_2$ that requires some more complex explanation than a simple Joule heating argument.

It should be stressed again that, quantitatively, the vdP method is not capable of accurately determining n and μ in the case of a 3D topological insulator (TI) [174]. Although it is yet to be determined whether $FeSb_2$ indeed falls into such a class of materials, we can state with confidence due to the Corbino measurements presented in section 6.3.1 that the vdP technique is not suitable for quantitatively describing the metallic surface states present at low temperatures in $FeSb_2$. This being said, for the elevated temperatures where bulk conduction dominates and -R_H (n) is decreasing (increasing), it should hold well. Yet, intriguingly, the disagreement in $\mu(I)$ compared to $\mu(T)$ over the range examined in Fig. 7.10 clearly indicates some unconventional mechanism at play.

The behaviour of the electrical transport at high currents allows us to speculate as to what features this unconventional mechanism may possess. Applying the simple tunnelling model discussed above, we can interpret the vdP data as giving effective behaviours for n and μ, in the context of a surface/bulk 2-component system. Assuming that low currents are constrained to the metallic surface of the sample, and the application of high currents enables tunnelling through to the bulk insulator, it is intuitive that n should decrease as the vdP measurement becomes sensitive to the bulk contribution at higher currents, as opposed to merely sampling the metallic surface channel in the low current regime. However, the observation of increasing $\mu(I)$ at the highest currents implies that, somehow, some property of the bulk is causing this effect. μ can be simply thought of as the mean drift velocity of the charge carriers divided by the electric field strength. Thus, unlike in the case of e.g. Gunn diodes, wherein negative differential resistance is accompanied by anomalous saturation of carrier velocities [257], in the case of $FeSb_2$ a saturation of μ was not observed up to the highest applied current of the dataset

presented in Fig. 7.10, of 8 mA. Further studies, extended to higher applied currents and perhaps employing local and nonlocal Corbino geometries, would help to provide a more complete understanding of these effects to be attained.

Furthermore, the experiments presented within this chapter were limited in their design owing to the irregular and varied shapes and sizes of high purity single crystals generated by the chemical vapour transport method. In order to preserve the pristine surfaces, no cutting was employed on the samples presented here; however, this made it very difficult to calculate the current density sourced through a given sample to any sensible degree of certainty, hence it has not been attempted in this present work. Future experiments, on perhaps needle-shaped samples (if these can be produced to a good level of quality), wherein the current density could be easily computed, would be very interesting in order to determine if it is the magnitude of voltage, current, or indeed current density that is of the highest importance in manifesting these anomalous effects observed here at low temperatures and high applied currents in $FeSb_2$.

7.4 Summary

This chapter presented a number of electrical transport measurements performed on $FeSb_2$, building on those of the previous chapter. Signatures of non-Ohmic conduction phenomena were explored, with $FeSb_2$ seen to yield an anomalous regime of negative differential resistance for high applied measurement currents. More similarities with SmB_6 were discussed, including some Joule heating arguments that have been proposed in attempt to explain similar effects previously reported in that material. However, in the case of $FeSb_2$ it was shown here that under the application of magnetic fields, for high excitation currents at low temperatures, a negative slope of magnetoresistance is observed that is not seen for low currents at higher temperatures. Therefore, the anomalous low temperature, high current behaviour of $FeSb_2$ must originate from some unconventional mechanism other than simple Joule heating, which was then discussed in the context of a surface/bulk tunnelling model. Future experiments to better characterise these anomalous effects were proposed.

8

Concluding remarks

"Forty-two," said Deep Thought, with infinite majesty and calm.

– Douglas Adams, *The Hitchhiker's Guide to the Galaxy*

This dissertation has presented a series of electrical and magnetic measurements on the strongly correlated unconventional insulator $FeSb_2$.

Magnetic measurements of an unconventional insulating Fermi surface intimately connected to bulk magnetic properties

The de Haas-van Alphen effect was observed through measuring quantum oscillations in the magnetisation of this material. Remarkably, these were shown to originate not from the metallic surface state nor from any extrinsic impurity source, but instead from the insulating bulk of the material – in direct contradiction to Landau's Fermi liquid model of quantum matter. The insulating quantum oscillations were found to be intimately connected to changes in the magnetic torque profile of the material, with three regimes of starkly contrasting insulating behaviour revealed.

At low fields, the torque was found to increase quadratically as a function of field,

as expected for a simple paramagnetic insulator. Then, at higher fields, the material's magnetisation grows much more rapidly, and includes oscillatory components that are periodic in inverse field and possess large amplitudes and high frequencies corresponding to quasiparticle orbits with an associated Fermi wavevector spanning an area of $\approx 20\%$ of the first Brillouin zone. These observations are indicative of a bulk 3D Fermi surface – despite the diametrically opposed observation of robustly insulating resistivity being exhibited up to higher magnetic field strengths than those at which the dHvA effect is observed.

Previous theoretical work had predicted that the $FeSb_2$ system shall transition into a ferromagnetic metal under the application of sufficiently high magnetic field strengths [182, 183]. However, instead of this we observed something markedly different – at the highest applied fields the unconventional insulating quantum oscillations are abruptly quenched at a metamagnetic transition, and no subsequent quantum oscillations are observed under the further application of magnetic fields of magnitude > 40 T.

That $FeSb_2$ stands apart from previously reported unconventional insulators, in exhibiting an intimate connection between the insulating quantum oscillatory profile and bulk magnetic properties, strongly suggests a magnetic origin to this paradoxical phenomenon, and thus tightly constrains future theoretical models [113–153].

Electrical measurements indicative of metallic surface states of potential topological character

For temperature, T, in the range $6\ \text{K} \lessapprox T \leq 300\ \text{K}$ the electrical transport of $FeSb_2$ was found to exhibit activated insulating resistivity. However, for $T \lessapprox 6\ \text{K}$ an anomalous resistance plateau was observed, which through a series of complementary measurements was shown to be indicative of the presence of metallic surface states. These complementary measurements included an evolution of magnetoresistive rotational symmetry on cooling, an inversion between local and nonlocal transport channels, and a quantitative disagreement between Corbino measurements with Hall-bar and van der Pauw results of

several orders of magnitude. Negative differential resistance measurements also underscored the presence of a metallic surface state in this system, whilst hinting at the greater complexity of the underlying mechanism(s) giving rise to this phenomenon.

These results were discussed in the context of SmB_6, a topological Kondo insulator candidate [32–34]. The observations indicative of surface-dominated conduction were found to be extremely similar across the two materials, both in qualitative character and also in their occurrence over very similar temperature ranges. It is likely, therefore, that whatever mechanism is driving the formation of surface states in SmB_6 is also responsible for those in $FeSb_2$. A discussion of the evidence in favour of a topologically non-trivial origin for the surface states in SmB_6 was presented, with future complementary research ideas indicated. An analysis of the numerous discrepancies in reported experimental observations across different sample growth and preparation methodologies of SmB_6 was made. Given the remarkable similitude in physical characteristics at low temperatures observed between these two materials, but the much more favourable chemistry with regards to growing high quality samples in the case of $FeSb_2$, this material therefore proffers a potentially superior alternative to SmB_6 with respect to obtaining single crystal specimens of a strongly correlated topological insulator candidate.

Unusual non-Ohmic conduction in both $FeSb_2$ and SmB_6 was presented, and discussed in the framework of a surface/bulk tunnelling model. Importantly, the effect of a magnetic field on the non-Ohmic resistivity behaviour of $FeSb_2$ strongly rules out a Joule-heating dominated origin, underscoring the anomalous behaviour exhibited by this material in the presence of an applied magnetic field. This study was extended to high applied field strengths, wherein quantised magnetotransport behaviour was observed, suggesting the presence of some exotic emergent physical behaviour underlying this suite of electrical measurements.

The similarities between the bulk and surface properties of $FeSb_2$ and SmB_6 were compared and contrasted. It is remarkable that both of these materials exhibit unconventional insulating quantum oscillations from their bulk, whilst also possessing metallic surface states that appear to be a result of their strongly correlated electronic natures. At present,

it is not clear how these surface and bulk properties may be connected. For the case of a magnetic topological insulator, it is perhaps possible that a magnetic transition of the surface state may induce a magnetic effect within the bulk. Furthermore, the finding of three regimes of starkly contrasting magnetic behaviour in $FeSb_2$ poses the additional question of whether SmB_6 may also undergo a metamagnetic transition at field strengths higher than those applied thus far.

Open questions for further investigation

The findings presented in this dissertation open the door to numerous further complementary studies. Regarding the magnetic features of this material, the rotational magnetic torque study presented in Fig. 5.8 should be extended through other rotational planes, such as $c - b$ and $c - ab$, to fields > 40 T, to fully map the evolution between regimes. Exploring other rotational planes will also be important in order to determine whether the anisotropy of the system may be hiding valuable insights as to the origin of the unconventional insulating quantum oscillations, that are yet to be explored. Furthermore, the empirical search for new materials systems that exhibit unconventional insulating quantum oscillations is imperative in guiding theoretical efforts on the topic. High field magnetic torque measurements of the related compounds FeSi and $FeGa_3$ would therefore be of great assistance – whether they exhibit the dHvA effect or not – in constraining future microscopic models for this phenomenon.

In addition, complementary measurements to further examine the nature of the three regimes of magnetic behaviour of $FeSb_2$, and the associated metamagnetic transition, would be highly informative. Such studies could employ, for example, the techniques of ultrasonic attenuation, specific heat capacity, thermal conductivity, force magnetometry, and/or dilatometry. Performing such measurements in the noisy environment of a high field water-cooled magnet may prove challenging; however, if undertaken successfully they could shed considerable light on the underlying mechanism responsible for the manifestation of unconventional quantum oscillations in insulators.

With regards to the metallic surface states, a thorough examination from complementary measurement techniques, such as spin-polarised ARPES and scanning tunnelling microscopy, would be extremely valuable in determining if their origin is indeed of a non-trivial topological character. Additionally, other transport measurements, such as thickness-dependant studies, have previously been well applied to SmB_6 [199, 234], yielding strong results indicative of surface dominated conduction; these would be reasonably straightforward to conduct for the case of $FeSb_2$. Furthermore, additional high magnetic field studies of the quantised magneotransport signatures presented in the appendix are urgently called for, in order to elucidate potential mechanisms for this unusual effect.

"I have done it," she says. At first I do not understand.

– Madeline Miller, *The Song of Achilles*

Appendix A

Preliminary observations of quantised magnetoconductance features

A.1 High field study

To further explore the effects of high measurement currents on $FeSb_2$ at low temperatures presented in chapter 7, an investigation in high dc magnetic fields was performed at the High Field Magnet Lab, Nijmegen, The Netherlands.

Figure A.1 shows the resistance of an $FeSb_2$ single crystal up to magnetic field strengths of 35 T, for different applied measurement currents as indicated. The sample was placed within a ^{3}He cryostat within a resistive magnet. Current was supplied using a Keithley 6221 current source unit, and measured by a Stanford Research Systems phase sensitive detector.

For the low applied currents of 5 μA and 10 μA, in the positive differential regime of this sample, negligible hysteresis between up- and down-sweeps is observed. However, at successively higher currents, hysteresis loops are observed, which appear to be quantised in integer and half-integer units of e^2/h.

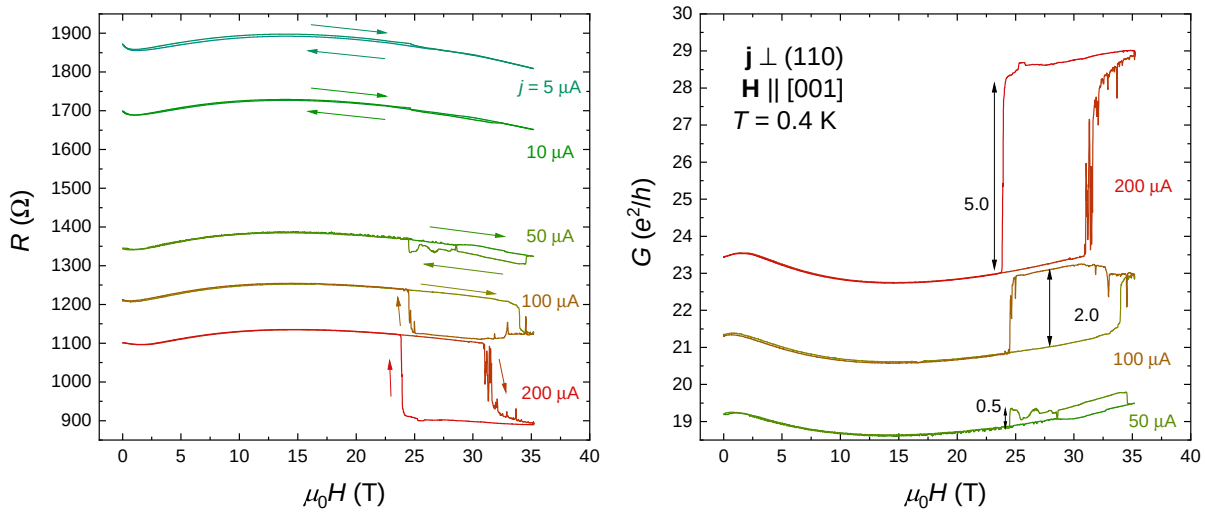

Fig. A.1. Quantised conduction at high fields and high currents. *Left:* Resistance, R, for several currents up to a magnetic field strength of 35 T. *Right:* The three highest currents in the left panel, plotted now as conductance, G. Remarkably, observed hysteresis loops at high fields appear to be quantised in integer and half-integer units of e^2/h.

Similar results have also been observed on other samples, and are currently the subject of ongoing investigation.

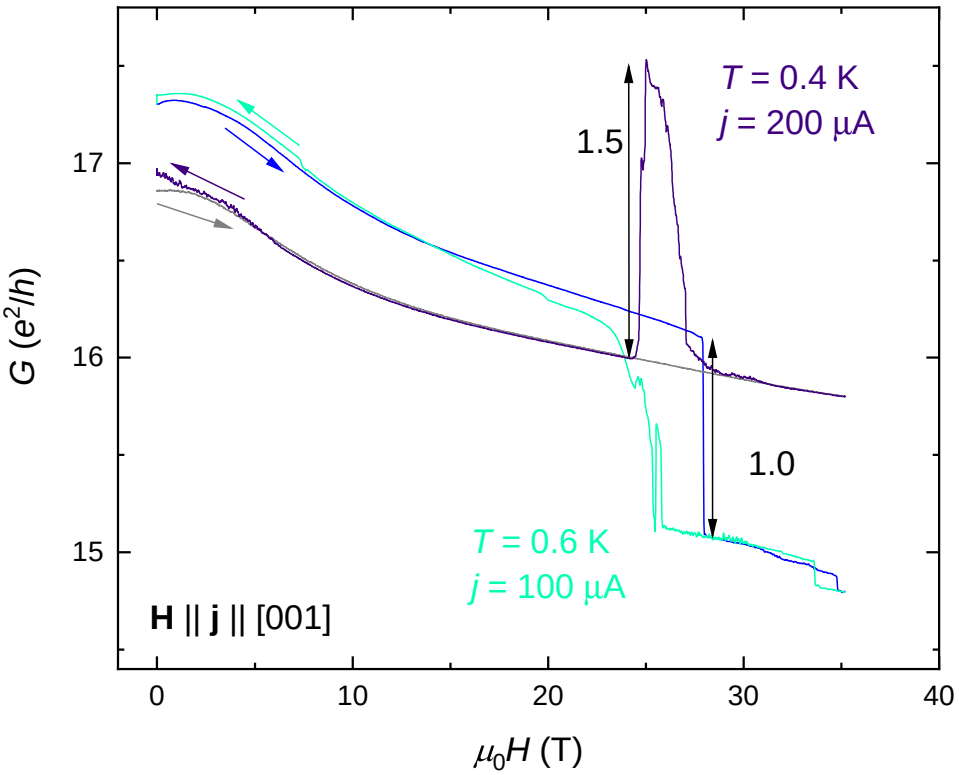

Fig. A.2. Quantised magnetoconductance data on a second sample. Similar results to those presented in Fig. A.1 obtained on a different sample, for current alignment in a different orientation. Jumps of e^2/h and $3e^2/2h$ are clearly resolved.

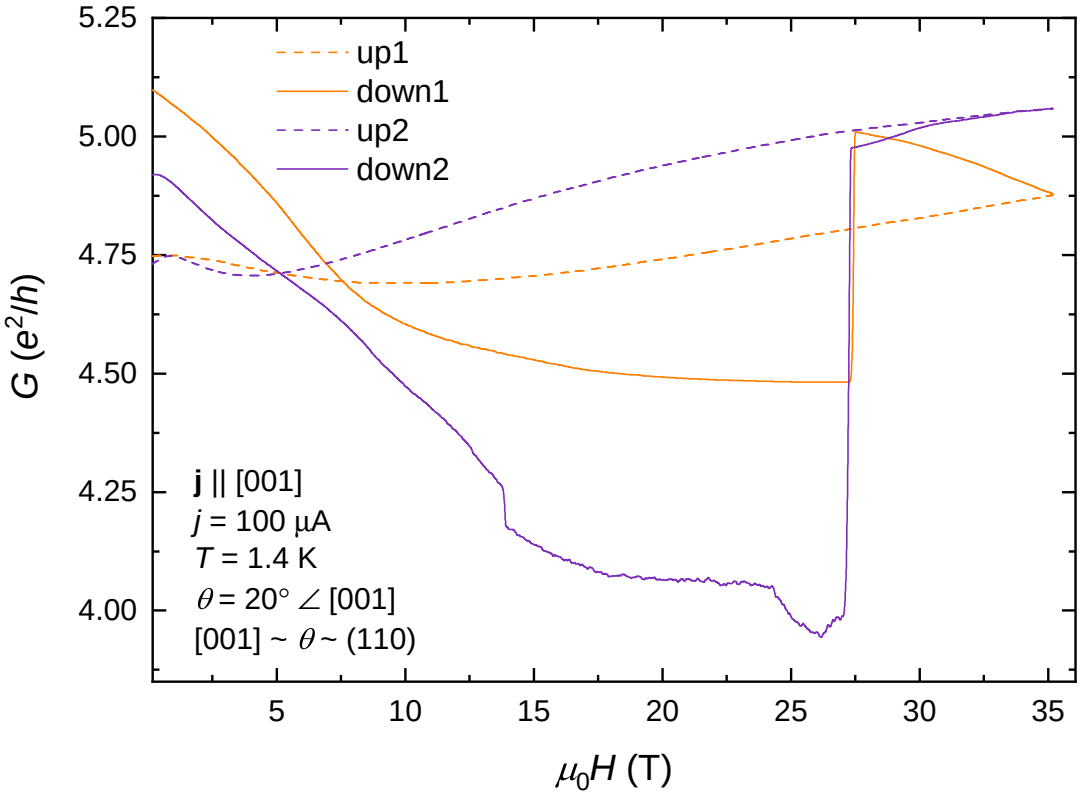

Fig. A.3. Quantised magnetoconductance data on a third sample. Successive field sweeps for rising (dashed) and falling (solid) magnetic field sweeps. The first (orange) sweep yielded a discontinuity of magnitude $e^2/2h$, while the second (purple) sweep yielded a discontinuity of magnitude e^2/h. This hints at complex hysteresis/magnetic switching effects that are yet to be fully explored.

A.2 Intermediate field study

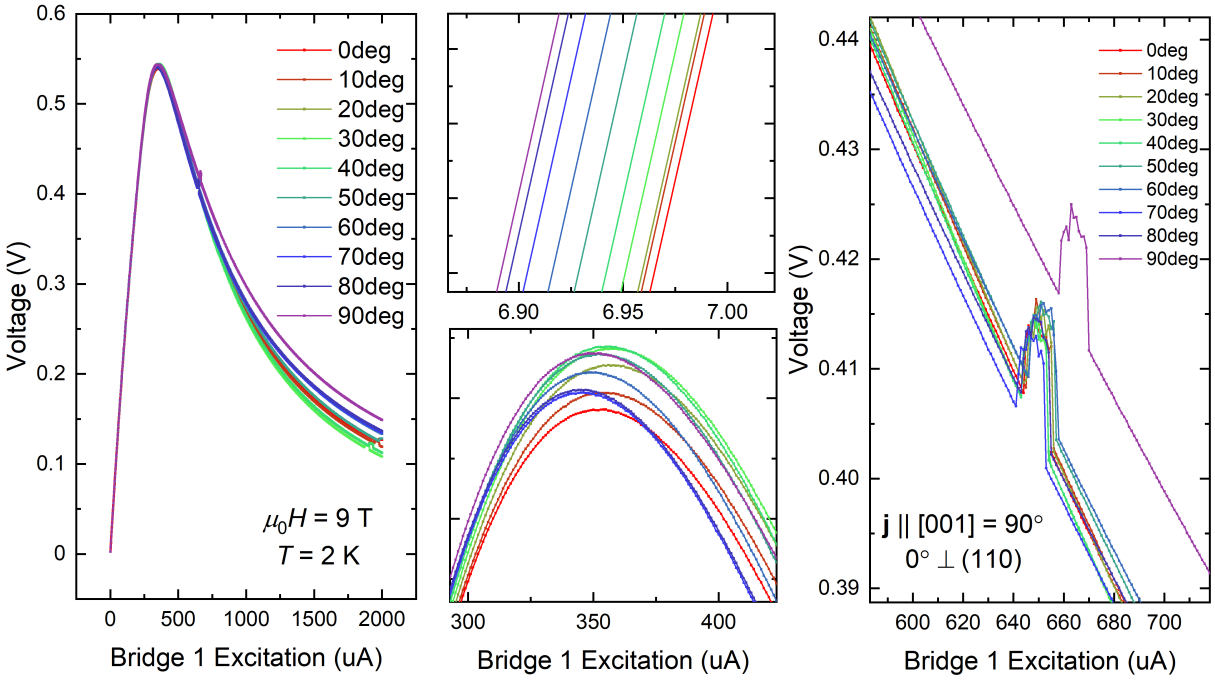

Fig. A.4. Anomaly in dc *I-V* curve. A more finely spaced dc *I-V* study than that presented in Fig. 7.9 reveals the presence of anomalies.

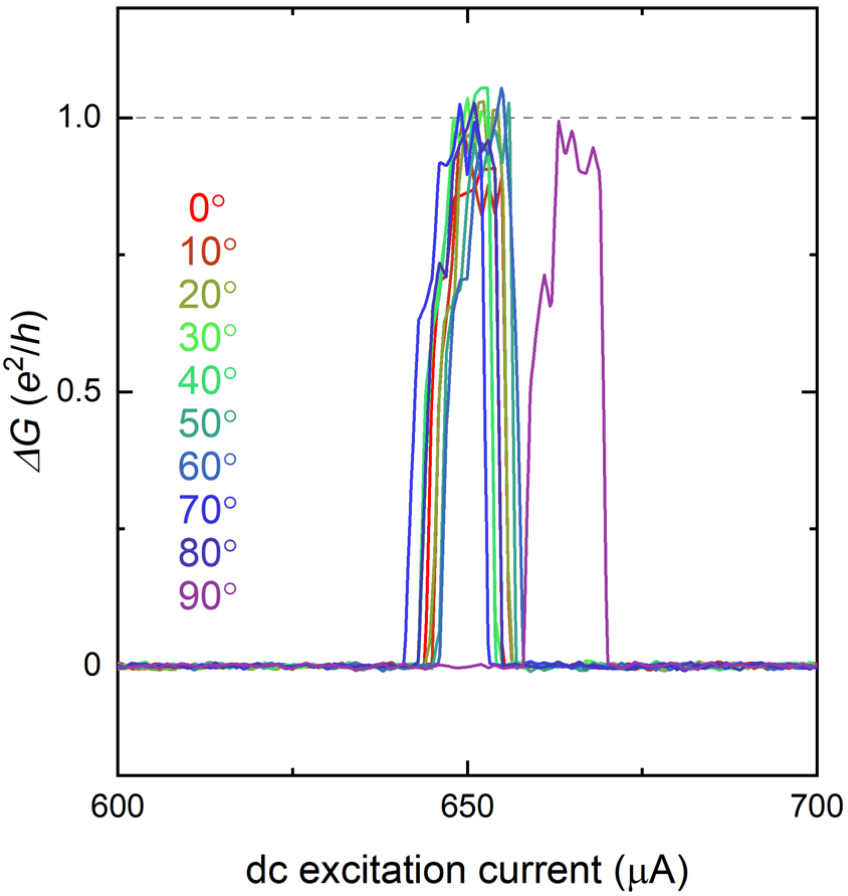

Fig. A.5. Quantised anomaly at $\mu_0 H$ = 9 T, T = 2 K. Subtracting the anomalous region from Fig. A.4 reveals it to possess a quantised magnitude of conductance.

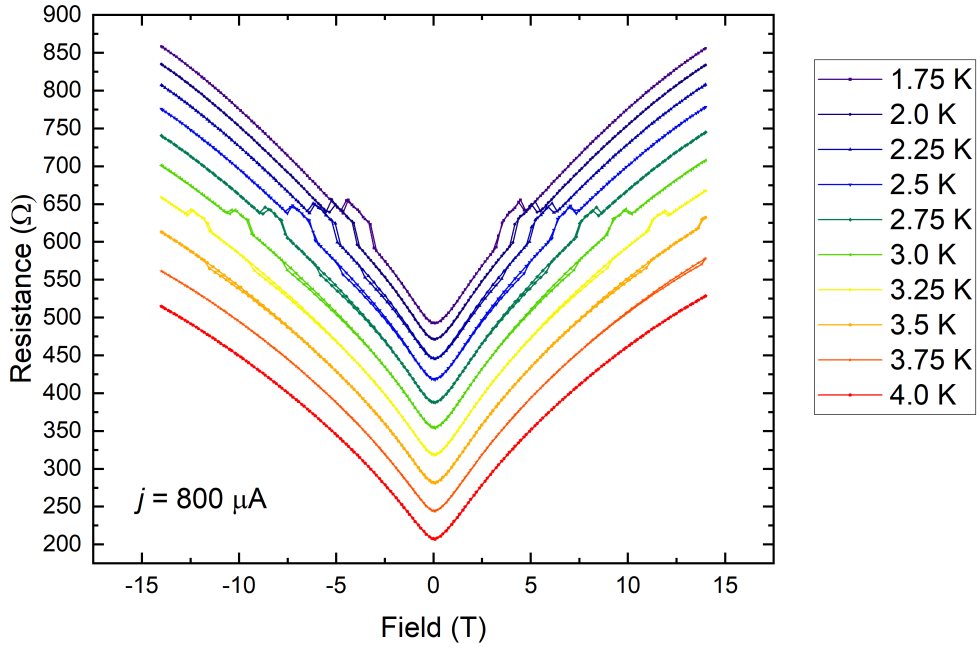

Fig. A.6. Anomalous resistance isotherms for a different sample. Interestingly, the anomalies appear to occur at the same resistance (and hence conductance) value for all temperatures.

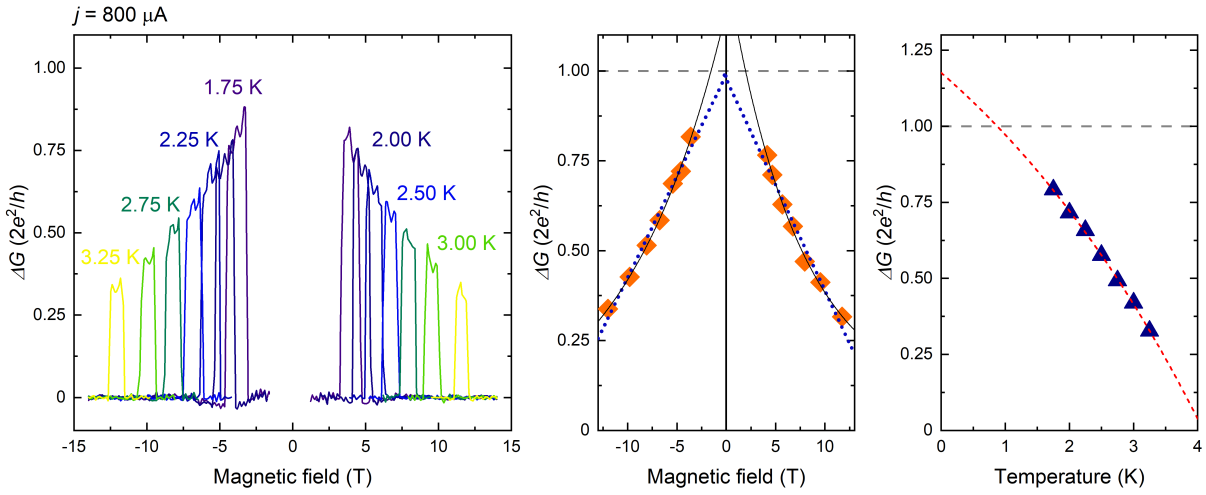

Fig. A.7. Anomaly size as a function of temperature. The magnitude of the anomaly appears to be tending towards $2e^2/h$ in the low temperature, high magnetic field limit.

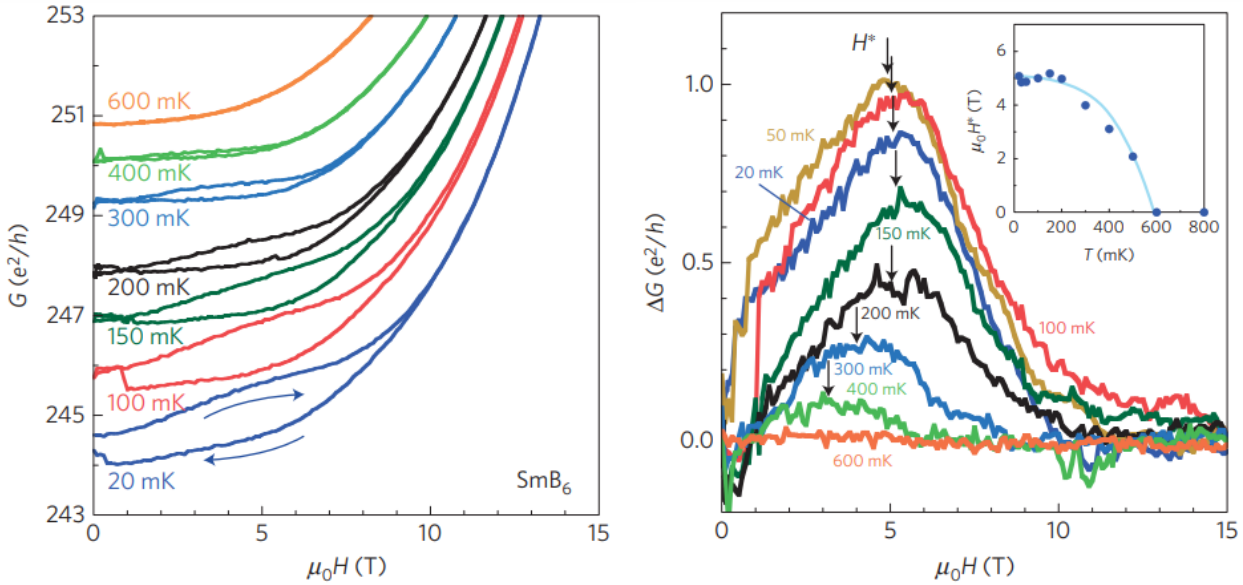

Fig. A.8. Quantised hysteretic magnetoconductance reported for SmB_6. Raw magnetoconductance (left panel) for an SmB_6 sample at temperatures indicated. Data have been vertically offset for clarity. A hysteresis between upward and downward magnetic field sweeps is observed, for which the difference between these sweeps appears to be close to the quantised value of e^2/h (right panel). Figure adapted from ref. [258] and reproduced with permission of Springer Nature.

Bibliography

[1] Fleming, A. On the Antibacterial Action of Cultures of a Penicillium, with Special Reference to Their Use in the Isolation of B. influenzae. *British Journal of Experimental Pathology* **10**, 226–236 (1929).

[2] Rutherford, E. The Scattering of α and β Particles by Matter and the Structure of the Atom. *Philos. Mag.* **6**, 21 (1911).

[3] Bednorz, J. G. & Müller, K. A. Possible high T_c superconductivity in the Ba-La-Cu-O system. *Zeitschrift für Physik B Condensed Matter* **64**, 189–193 (1986).

[4] Thouless, D. J., Kohmoto, M., Nightingale, M. P. & den Nijs, M. Quantized Hall Conductance in a Two-Dimensional Periodic Potential. *Phys. Rev. Lett.* **49**, 405–408 (1982).

[5] Haldane, F. D. M. Continuum dynamics of the 1-D Heisenberg antiferromagnet: Identification with the O(3) nonlinear sigma model. *Phys. Lett. A* **93**, 464–468 (1983).

[6] Berry, M. V. Quantal phase factors accompanying adiabatic changes. *Proc. R. Soc. Lond. A* **392**, 45–57 (1984).

[7] Moore, J. E. The birth of topological insulators. *Nature* **464**, 194–8 (2010).

[8] Hasan, M. Z. & Kane, C. L. Colloquium: Topological insulators. *Rev. Mod. Phys.* **82**, 3045–3067 (2010).

[9] Bloch, F. Über die Quantenmechanik der Elektronen in Kristallgittern. *Zeitschrift für Physik* **52**, 555–600 (1929).

[10] Anderson, P. W. Plasmons, Gauge Invariance, and Mass. *Phys. Rev.* **130**, 439–442 (1963).

[11] Higgs, P. W. Broken Symmetries and the Masses of Gauge Bosons. *Phys. Rev. Lett.* **13**, 508–509 (1964).

[12] The ATLAS Collaboration, *et al.* Observation of a new particle in the search for the Standard Model Higgs boson with the ATLAS detector at the LHC. *Phys. Lett. B* **716**, 1–29 (2012).

[13] Rochester, G. D. & Butler, C. C. Evidence for the Existence of New Unstable Elementary Particles. *Nature* **160**, 855–857 (1947).

[14] Dugdale, S. B. Life on the edge: a beginner's guide to the Fermi surface. *Phys. Scr.* **91**, 053009 (2016).

[15] Simon, S. H. *The Oxford Solid State Basics* (Oxford University Press, Oxford, UK, 2013).

[16] Mott, N. F. & Peierls, R. Discussion of the paper by de Boer and Verwey. *Proc. Phys. Soc.* **49**, 72–73 (1937).

[17] Mott, N. F. The Basis of the Electron Theory of Metals, with Special Reference to the Transition Metals. *Proc. Phys. Soc. A* **62**, 416–422 (1949).

[18] Shoenberg, D. *Magnetic Oscillations in Metals* (Cambridge University Press, Cambridge, UK, Cambridge, UK, 1984).

[19] Tan, B. S. *et al.* Unconventional Fermi surface in an insulating state. *Science.* **349**, 287–290 (2015).

[20] Hartstein, M. *et al.* Fermi surface in the absence of a Fermi liquid in the Kondo insulator SmB_6. *Nat. Phys.* **14**, 166 (2018).

[21] Li, G. *et al.* Two-dimensional Fermi surfaces in Kondo Insulator SmB6. *Science.* **346**, 1208 – 1212 (2014).

[22] Liu, H. *et al.* Fermi surfaces in Kondo insulators. *J. Phys. Condens. Matter* **30**, 16LT01 (2018).

[23] Xiang, Z. *et al.* Quantum oscillations of electrical resistivity in an insulator. *Science.* **69**, 65–69 (2018).

[24] Wang, P. *et al.* Landau Quantization and Highly Mobile Fermions in an Insulator. *Nature.* **589**, 225–9 (2021).

[25] Czajka, P. *et al.* Oscillations of the thermal conductivity observed in the spin-liquid state of α-$RuCl_3$. *Nat. Phys.* **17**, 915–919 (2021).

[26] Coleman, P. *Introduction to Many-Body Physics* (Cambridge University Press, Cambridge, UK, 2015).

[27] Kondo, J. Resistance Minimum in Dilute Magnetic Alloys. *Progress of Theoretical Physics* **32**, 37–49 (1964).

[28] Hewson, A. C. *The Kondo Problem to Heavy Fermions* (Cambridge University Press, Cambridge, 1997).

[29] Ruderman, M. A. & Kittel, C. Indirect Exchange Coupling of Nuclear Magnetic Moments by Conduction Electrons. *Phys. Rev.* **96**, 99–102 (1954).

[30] Kasuya, T. A Theory of Metallic Ferro- and Antiferromagnetism on Zener's Model. *Progress of Theoretical Physics* **16**, 45–57 (1956).

[31] Yosida, K. Magnetic Properties of Cu-Mn Alloys. *Phys. Rev.* **106**, 893–898 (1957).

[32] Dzero, M., Xia, J., Galitski, V. & Coleman, P. Topological Kondo Insulators. *Phys. Rev. Lett.* **104**, 106408 (2010).

[33] Dzero, M., Xia, J., Galitski, V. & Coleman, P. Topological Kondo Insulators. *Ann.*

Rev. Cond. Matt. Phys. **7**, 249–280 (2016).

[34] Li, L., Sun, K., Kurdak, C. & Allen, J. W. Emergent mystery in the Kondo insulator samarium hexaboride. *Nat. Rev. Phys.* **2**, 463–479 (2020).

[35] Menth, A., Buehler, E. & Geballe, T. H. Magnetic and semiconducting properties of SmB6. *Phys. Rev. Lett.* **22**, 295–297 (1969).

[36] Allen, J. W., Batlogg, B. & Wachter, P. Large low-temperature Hall effect and resistivity in mixed-valent SmB_6. *Phys. Rev. B* **20**, 4807–4813 (1979).

[37] Tomczak, J. M. Thermoelectricity in correlated narrow-gap semiconductors. *J. Phys. Condens. Matter* **30**, 183001 (2018).

[38] Sun, P. *et al. Magnetism and Spin States of $FeSb_2$* (Max Planck Institute for Chemical Physics of Solids Scientific Report, Dresden, 2011). URL `https://www.cpfs.mpg.de/en/publications/scientific_report`.

[39] Mizumaki, M., Tsutsui, S. & Iga, F. Temperature dependence of Sm valence in SmB_6 studied by X-ray absorption spectroscopy. *J. Phys.: Conf. Ser.* **176**, 012034 (2009).

[40] Martin, R. M. & Allen, J. W. Theory of mixed valence: Metals or small gap insulators (invited). *J. App. Phys.* **50**, 7561–7566 (1979).

[41] Nickerson, J. C. *et al.* Physical Properties of SmB_6. *Phys. Rev. B* **3**, 2030–2042 (1971).

[42] Kasuya, T., Takegahara, K., Fujita, T., Tanaka, T. & Bannai, E. Valence Fluctuating State in SmB_6. *J. Phys. Colloq.* **40**, 308–313 (1979).

[43] Eaton, A. G. *et al.* Electrical transport signatures of metallic surface state formation in the strongly-correlated insulator $FeSb_2$. *In preparation* (2022).

[44] Eaton, A. G. *et al.* Metamagnetic insulator–to–insulator transition underlying unconventional insulating behaviour in $FeSb_2$. *Unpublished* (2022).

[45] Bentien, A., Johnsen, S., Madsen, G. K., Iversen, B. B. & Steglich, F. Colossal Seebeck

coefficient in strongly correlated semiconductor FeSb 2. *EPL* **80**, 17008 (2007).

[46] Xu, K.-J. *et al.* Metallic surface states in a correlated d-electron topological Kondo insulator candidate $FeSb_2$. *Proc. Natl. Acad. Sci. U.S.A.* **117**, 15409–15413 (2020).

[47] Sun, P., Søndergaard, M., Iversen, B. & Steglich, F. Strong electron correlations in $FeSb_2$. *Ann. Phys.* **523**, 612–620 (2011).

[48] Sun, P., Oeschler, N., Johnsen, S., Iversen, B. B. & Steglich, F. $FeSb_2$: Prototype of huge electron-diffusion thermoelectricity. *Phys. Rev. B* **79**, 153308 (2009).

[49] Petrovic, C. *et al.* Kondo insulator description of spin state transition in $FeSb_2$. *Phys. Rev. B* **72**, 045103 (2005).

[50] Herzog, A. *et al.* Strong electron correlations in $FeSb_2$: An optical investigation and comparison with $RuSb_2$. *Phys. Rev. B* **82**, 245205 (2010).

[51] Sun, P., Oeschler, N., Johnsen, S., Iversen, B. B. & Steglich, F. Huge Thermoelectric Power Factor: $FeSb_2$ versus $FeAs_2$ and $RuSb_2$. *Appl. Phys. Express* **2**, 091102 (2009).

[52] Sun, P., Oeschler, N., Johnsen, S., Iversen, B. B. & Steglich, F. Narrow band gap and enhanced thermoelectricity in $FeSb_2$. *Dalton Trans.* **39**, 1012–1019 (2010).

[53] Figueira, M. S., Silva-Valencia, J. & Franco, R. Thermoelectric properties of the Kondo insulator $FeSb_2$. *Euro. Phys. J. B* **85**, 203 (2012).

[54] Hong, S., Ghaemi, P., Moore, J. E. & Phillips, P. W. Tuning thermoelectric power factor by crystal-field and spin-orbit couplings in Kondo-lattice materials. *Phys. Rev. B* **88**, 075118 (2013).

[55] Homes, C. C. *et al.* Unusual electronic and vibrational properties in the colossal thermopower material $FeSb_2$. *Scientific Reports* **8**, 1–9 (2018).

[56] Takahashi, H. *et al.* Colossal Seebeck effect enhanced by quasi-ballistic phonons dragging massive electrons in $FeSb_2$. *Nat. Commun.* **7**, 12732 (2016).

[57] Du, Q. & Petrovic, C. Optimal carrier concentration for $FeSb_2$ colossal thermopower. *Appl. Phys. Lett.* **118**, 233901 (2021).

[58] Takahashi, H., Yasui, Y., Terasaki, I. & Sato, M. Effects of ppm-level imperfection on the transport properties of $FeSb_2$ single crystals. *J. Phys. Soc. Jpn.* **80**, 054708 (2011).

[59] Sun, P. *et al.* Highly dispersive electron relaxation and colossal thermoelectricity in the correlated semiconductor $FeSb_2$. *Phys. Rev. B* **88**, 245203 (2013).

[60] Hu, R., Mitrović, V. F. & Petrovic, C. Giant carrier mobility in single crystals of $FeSb_2$. *App. Phys. Lett.* **92**, 182108 (2008).

[61] Hu, R. *et al.* Electronic Griffiths Phase in the Te-Doped Semiconductor $\mathrm{FeSb_2}$. *Phys. Rev. Lett.* **109**, 256401 (2012).

[62] Kassem, M. A., Tabata, Y., Waki, T. & Nakamura, H. Crystal growth and metallic ferromagnetism induced by electron doping in $FeSb_2$ (2020). arXiv:2011.10343.

[63] Bentien, A., Madsen, G. K. H., Johnsen, S. & Iversen, B. B. Experimental and theoretical investigations of strongly correlated $\mathrm{FeSb_{2-x}Sn_x}$. *Phys. Rev. B* **74**, 205105 (2006).

[64] DiTusa, J. F., Friemelt, K., Bucher, E., Aeppli, G. & Ramirez, A. P. Metal-Insulator Transitions in the Kondo Insulator FeSi and Classic Semiconductors Are Similar. *Phys. Rev. Lett.* **78**, 2831–2834 (1997).

[65] DiTusa, J. F., Friemelt, K., Bucher, E., Aeppli, G. & Ramirez, A. P. Heavy fermion metal–Kondo insulator transition in $\mathrm{FeSi_{1-x}Al_x}$. *Phys. Rev. B* **58**, 10288–10301 (1998).

[66] Manyala, N., DiTusa, J. F., Aeppli, G. & Ramirez, A. P. Doping a semiconductor to create an unconventional metal. *Nature* **454**, 976–980 (2008).

[67] Schlesinger, Z. *et al.* Unconventional charge gap formation in FeSi. *Phys. Rev. Lett.* **71**, 1748–1751 (1993).

[68] Mandrus, D., Sarrao, J. L., Migliori, A., Thompson, J. D. & Fisk, Z. Thermodynamics of FeSi. *Phys. Rev. B* **51**, 4763–4767 (1995).

[69] Fang, Y. *et al.* Evidence for a conducting surface ground state in high-quality single crystalline FeSi. *Proc. Natl. Acad. Sci. U.S.A.* **115**, 8558–8562 (2018).

[70] Wolgast, S. *et al.* Low-temperature surface conduction in the Kondo insulator SmB_6. *Phys. Rev. B* **88**, 180405(R) (2013).

[71] Kim, D. J. *et al.* Surface Hall Effect and Nonlocal Transport in SmB_6: Evidence for Surface Conduction. *Scientific Reports* **3**, 1–4 (2013).

[72] Messiah, A. *Quantum Mechanics*, vol. 1 (North-Holland Publishing Company, Amsterdam, The Netherlands, 1961).

[73] Murphy, K. J. *Quantum oscillation studies in the unconventional superconductor YFe_2Ge_2 and in the Dirac semimetal candidates NbXSb (X = Ge/Si)*. Ph.D. Thesis, University of Cambridge (2020).

[74] Onsager, L. Interpretation of the de Haas-van Alphen effect. *Philos. Mag.* **43**, 1006–1008 (1952).

[75] de Haas, W. J. & van Alphen, P. M. The dependence of the susceptibility of diamagnetic metals upon the field. *Proc. Roy. Acad. Sci. Netherlands* **130**, 1106–1118 (1930).

[76] Schubnikow, L. & de Haas, W. J. New phenomena in the change in resistance of bismuth crystals in a magnetic field at the temperature of liquid hydrogen (I). *Proc. Roy. Acad. Sci. Netherlands* **130**, 363–378 (1930).

[77] Ashcroft, N. W. & Mermin, D. N. *Solid State Physics* (Harcourt College Publishers, San Diego, CA, 1976).

[78] Lifshitz, I. M. & Kosevich, A. M. Theory of Magnetic Susceptibility in Metals at Low Temperatures. *Sov. Phys. JETP* **2**, 636–645 (1956).

[79] Carrington, A. Quantum oscillation studies of the Fermi surface of iron-pnictide superconductors. *Reports Prog. Phys.* **74**, 124507 (2011).

[80] Ramshaw, B. *Shubnikov-de Haas Measurements and the Spin Magnetic Moment of* $YBa_2Cu_3O_{6.59}$. Ph.D. Thesis, The University of British Columbia (2012).

[81] Riebesell, J. Graphics with TikZ in LaTeX. URL `https://github.com/janosh/tikz/blob/main/license`.

[82] Dingle, R. B. Some magnetic properties of metals II. The influence of collisions on the magnetic behaviour of large systems. *Proc. R. Soc. Lond. A* **211**, 517–525 (1952).

[83] Hartstein, M. *Fermi Surfaces and Where to Find Them: Quantum Oscillations in Kondo Insulators and High-Temperature Superconductors*. Ph.D. Thesis, University of Cambridge (2021).

[84] Hassinger, E. *Competition of ground states in* URu_2Si_2 *and UCoGe*. Ph.D. Thesis, Université de Grenoble (2010).

[85] Li, L. *et al.* Phase Transitions of Dirac Electrons in Bismuth. *Science* **321**, 547–550 (2008).

[86] Behnia, K., Balicas, L. & Kopelevich, Y. Signatures of Electron Fractionalization in Ultraquantum Bismuth. *Science* **317**, 1729–1731 (2007).

[87] Blount, E. I. Bloch Electrons in a Magnetic Field. *Phys. Rev.* **126**, 1636–1653 (1962).

[88] Harrison, N. *et al.* Numerical model of quantum oscillations in quasi-two-dimensional organic metals in high magnetic fields. *Phys. Rev. B* **54**, 9977–9987 (1996).

[89] Hartstein, M. *et al.* Hard antinodal gap revealed by quantum oscillations in the pseudogap regime of underdoped high-Tc superconductors. *Nat. Phys.* **16**, 841–847 (2020).

[90] Griessen, R. A capacitance torquemeter for de Haas-van Alphen measurements. *Cryogenics* **13**, 375–377 (1973).

[91] Hartstein, M. *et al.* Intrinsic Bulk Quantum Oscillations in a Bulk Unconventional Insulator SmB_6. *iScience* **23**, 101632 (2020).

[92] Boulanger, M.-E. *et al.* Field-dependent heat transport in the Kondo insulator $\mathrm{SmB_6}$: Phonons scattered by magnetic impurities. *Phys. Rev. B* **97**, 245141 (2018).

[93] Thomas, S. M. *et al.* Quantum Oscillations in Flux-Grown SmB_6 with Embedded Aluminum. *Phys. Rev. Lett.* **122**, 166401 (2019).

[94] Millichamp, T. E. *et al.* Direct measurement of a remnant Fermi surface in SmB_6 (2021). arXiv:2111.07727.

[95] LaBarre, P. G. *et al.* Magnetoquantum oscillations in the specific heat of a topological Kondo insulator. *J. Phys. Condens. Matter* **34**, 36LT01 (2022).

[96] Xiang, Z. *et al.* Hall Anomaly, Quantum Oscillations and Possible Lifshitz Transitions in Kondo Insulator $\mathrm{YbB_{12}}$: Evidence for Unconventional Charge Transport. *Phys. Rev. X* **12**, 021050 (2022).

[97] Liu, H. *et al.* f-electron hybridised Fermi surface in magnetic field-induced metallic YbB_{12}. *npj Quantum Materials* **7** (2022).

[98] Xiang, Z. *et al.* Unusual high-field metal in a Kondo insulator. *Nat. Phys.* **17**, 788–793 (2021).

[99] Sato, Y. *et al.* Unconventional thermal metallic state of charge-neutral fermions in an insulator. *Nat. Phys.* **15**, 954–959 (2019).

[100] Fei, Z. *et al.* Edge conduction in monolayer WTe_2. *Nat. Phys.* **13**, 677–682 (2017).

[101] Zhu, J., Li, T., Young, A. F., Shan, J. & Mak, K. F. Quantum Oscillations in Two-Dimensional Insulators Induced by Graphite Gates. *Phys. Rev. Lett.* **127**, 247702 (2021).

[102] Wang, P. Private communication, (2022).

[103] Kitaev, A. Anyons in an exactly solved model and beyond. *Ann. Phys.* **321**, 2–111 (2006).

[104] Banerjee, A. *et al.* Neutron scattering in the proximate quantum spin liquid αRuCl$_3$. *Science* **356**, 1055–1059 (2017).

[105] Bruin, J. A. N. *et al.* Origin of oscillatory structures in the magnetothermal conductivity of the putative Kitaev magnet α-RuCl$_3$ (2022). arXiv:2205.15839.

[106] Taillefer, L. Quantum Matter Seminar, Cavendish Laboratory, University of Cambridge, (2022).

[107] Anderson, P. W. Breaking the log-jam in many-body physics: Fermi surfaces without Fermi liquids. *Phys. Scr.* **T42**, 11–16 (1992).

[108] Coleman, P., Miranda, E. & Tsvelik, A. Are Kondo insulators gapless? *Phys. B Condens. Matter* **186-188**, 362–364 (1993).

[109] Paul, I., Pépin, C. & Norman, M. R. Kondo breakdown and hybridization fluctuations in the Kondo-Heisenberg lattice. *Phys. Rev. Lett.* **98**, 026402 (2007).

[110] Banerjee, S., Zhang, S. & Randeria, M. Theory of quantum oscillations in the vortex-liquid state of high-Tc superconductors. *Nat. Commun.* **4**, 1700 (2013).

[111] Kishigi, K. & Hasegawa, Y. Quantum oscillations of magnetization in tight-binding electrons on a honeycomb lattice. *Phys. Rev. B* **90**, 085427 (2014).

[112] Zaanen, J., Liu, Y., Sun, Y. & Schalm, K. *Holographic Duality in Condensed Matter Physics* (Cambridge University Press, Cambridge, UK, 2015).

[113] Baskaran, G. Majorana Fermi Sea in Insulating SmB$_6$: A proposal and a Theory of Quantum Oscillations in Kondo Insulators (2015). arXiv:1507.03477.

[114] Erten, O., Chang, P. Y., Coleman, P. & Tsvelik, A. M. Skyrme Insulators: Insulators

at the Brink of Superconductivity. *Phys. Rev. Lett.* **119**, 057603 (2017).

[115] Varma, C. M. Majoranas in mixed-valence insulators. *Phys. Rev. B* **102**, 155145 (2020).

[116] Coleman, P., Panigrahi, A. & Tsvelik, A. A solvable 3D Kondo lattice exhibiting odd-frequency pairing and order fractionalization (2022). arXiv:2203.04104.

[117] Knolle, J. & Cooper, N. R. Excitons in topological Kondo insulators: Theory of thermodynamic and transport anomalies in SmB_6. *Phys. Rev. Lett.* **118**, 096604 (2017).

[118] Chowdhury, D., Sodemann, I. & Senthil, T. Mixed-valence insulators with neutral Fermi surfaces. *Nat. Commun.* **9**, 1766 (2018).

[119] Sodemann, I., Chowdhury, D. & Senthil, T. Quantum oscillations in insulators with neutral Fermi surfaces. *Phys. Rev. B* **97**, 045152 (2018).

[120] Rao, P. & Sodemann, I. Cyclotron resonance inside the Mott gap: A fingerprint of emergent neutral fermions. *Phys. Rev. B* **100**, 155150 (2019).

[121] Lee, P. A. Quantum oscillations in the activated conductivity in excitonic insulators: Possible application to monolayer WTe_2. *Phys. Rev. B* **103**, L041101 (2021).

[122] He, W.-Y. & Lee, P. A. Quantum oscillation of thermally activated conductivity in a monolayer WTe_2-like excitonic insulator. *Phys. Rev. B* **104**, L041110 (2021).

[123] Thomson, A. & Sachdev, S. Fractionalized Fermi liquid on the surface of a topological Kondo insulator. *Phys. Rev. B* **93**, 125103 (2016).

[124] Wu, Q. & Sun, L. Puzzle maker in SmB_6: accompany-type valence fluctuation state. *Rep. Prog. Phys.* **80**, 112501 (2017).

[125] Skinner, B. Properties of the donor impurity band in mixed valence insulators. *Phys. Rev. Mater.* **3**, 104601 (2019).

[126] Shen, H. & Fu, L. Quantum Oscillation from In-Gap States and a Non-Hermitian

Landau Level Problem. *Phys. Rev. Lett.* **121**, 026403 (2018).

[127] Harrison, N. Highly Asymmetric Nodal Semimetal in Bulk SmB_6. *Phys. Rev. Lett.* **121**, 026602 (2018).

[128] Fuhrman, W. T. and Nikolić, P. Magnetic impurities in Kondo insulators: An application to samarium hexaboride. *Phys. Rev. B* **101**, 245118 (2020).

[129] Peters, R., Yoshida, T. & Kawakami, N. Quantum oscillations in strongly correlated topological Kondo insulators. *Phys. Rev. B* **100**, 085124 (2019).

[130] Devakul, T., Kwan, Y. H., Sondhi, S. L. & Parameswaran, S. A. Quantum Oscillations in the Zeroth Landau Level: Serpentine Landau Fan and the Chiral Anomaly. *Phys. Rev. Lett.* **127**, 116602 (2021).

[131] Liu, J. & Balents, L. Correlation effects and quantum oscillations in topological nodal-loop semimetals. *Phys. Rev. B* **95**, 075426 (2017).

[132] Valentine, M. E. *et al.* Breakdown of the Kondo insulating state in SmB_6 by introducing Sm vacancies. *Phys. Rev. B* **94**, 075102 (2016).

[133] Pal, H. K., Piéchon, F., Fuchs, J. N., Goerbig, M. & Montambaux, G. Chemical potential asymmetry and quantum oscillations in insulators. *Phys. Rev. B* **94**, 125140 (2016).

[134] Pal, H. K. Quantum oscillations from inside the Fermi sea. *Phys. Rev. B* **95**, 085111 (2017).

[135] Pal, H. K. Unusual frequency of quantum oscillations in strongly particle-hole asymmetric insulators. *Phys. Rev. B* **96**, 235121 (2017).

[136] Pal, H. K. Anomalies in a slightly doped insulator with strong particle-hole asymmetry and a narrow gap: The case of SmB_6. *Phys. Rev. B* **99**, 045149 (2019).

[137] Knolle, J. & Cooper, N. R. Quantum Oscillations without a Fermi Surface and the Anomalous de Haas-van Alphen Effect. *Phys. Rev. Lett.* **115**, 146401 (2015).

[138] Riseborough, P. S. & Fisk, Z. Critical examination of quantum oscillations in SmB_6. *Phys. Rev. B* **96**, 195122 (2017).

[139] Alisultanov, Z. Z. On quantum oscillations in a tunable graphene bilayer. *JETP Lett.* **104**, 188–192 (2016).

[140] Erten, O., Ghaemi, P. & Coleman, P. Kondo Breakdown and Quantum Oscillations in SmB_6. *Phys. Rev. Lett.* **116**, 046403 (2016).

[141] Zhang, L., Song, X. Y. & Wang, F. Quantum Oscillation in Narrow-Gap Topological Insulators. *Phys. Rev. Lett.* **116**, 046404 (2016).

[142] Grubinskas, S. & Fritz, L. Modification of the Lifshitz-Kosevich formula for anomalous de Haas-van Alphen oscillations in inverted insulators. *Phys. Rev. B* **97**, 115202 (2018).

[143] Tada, Y. Cyclotron resonance in Kondo insulator. *Phys. Rev. Research* **2**, 023194 (2020).

[144] Lu, Y.-W., Chou, P.-H., Chung, C.-H., Lee, T.-K. & Mou, C.-Y. Enhanced quantum oscillations in Kondo insulators. *Phys. Rev. B* **101**, 115102 (2020).

[145] Sakhya, A. P. & Maiti, K. Ground state anomalies in SmB_6. *Sci. Rep.* **10**, 1262 (2020).

[146] Pixley, J. H., Yu, R., Paschen, S. & Si, Q. Global phase diagram and momentum distribution of single-particle excitations in Kondo insulators. *Phys. Rev. B* **98**, 085110 (2018).

[147] Ram, P. & Kumar, B. Theory of quantum oscillations of magnetization in Kondo insulators. *Phys. Rev. B* **96**, 075115 (2017).

[148] Ram, P. & Kumar, B. Inversion and magnetic quantum oscillations in the symmetric periodic Anderson model. *Phys. Rev. B* **99**, 235130 (2019).

[149] Panday, S. R. & Dzero, M. Interacting fermions in narrow-gap semiconductors with band inversion. *J. Phys. Condens. Matter* **33**, 275601 (2021).

[150] Fabrizio, M. Emergent quasiparticles at Luttinger surfaces. *Nat. Commun.* **13**, 1561 (2022).

[151] Allocca, A. A. & Cooper, N. R. Quantum oscillations in interaction-driven insulators. *SciPost Phys.* **12**, 123 (2022).

[152] Panda, A., Banerjee, S. & Randeria, M. Quantum oscillations in the magnetisation and density of states of insulators. *Proc. Natl. Acad. Sci. USA* **119**, e2208373119 (2022).

[153] Zhang, R. *et al.* Critical role of magnetic moments in heavy-fermion materials: Revisiting $\mathrm{SmB_6}$. *Phys. Rev. B* **105**, 195134 (2022).

[154] Motrunich, O. I. Orbital magnetic field effects in spin liquid with spinon Fermi sea: Possible application to κ-$(\mathrm{ET})_2\mathrm{Cu}_2(\mathrm{CN})_3$. *Phys. Rev. B* **73**, 155115 (2006).

[155] Bulaevskii, L. N., Batista, C. D., Mostovoy, M. V. & Khomskii, D. I. Electronic orbital currents and polarization in Mott insulators. *Phys. Rev. B* **78**, 024402 (2008).

[156] Grover, T., Trivedi, N., Senthil, T. & Lee, P. A. Weak Mott insulators on the triangular lattice: Possibility of a gapless nematic quantum spin liquid. *Phys. Rev. B* **81**, 245121 (2010).

[157] Katsura, H., Nagaosa, N. & Lee, P. A. Theory of the Thermal Hall Effect in Quantum Magnets. *Phys. Rev. Lett.* **104**, 066403 (2010).

[158] Majorana, E. Teoria simmetrica dell'elettrone e del positrone. *Nuovo Cim.* **14**, 171–184 (1937).

[159] Chumak, I. V., Pavlyuk, V. V., Dmytriv, G. S. & Stepień-Damm, J. Phase equilibria and crystal structure of compounds in the Fe-Zn-Sb system at 570 K. *J. Alloys Compd.* **307**, 223–225 (2000).

[160] Mozharivskyj, Y., Pecharsky, A. O., Bud'ko, S. & Miller, G. J. A Promising Thermoelectric Material: $\mathrm{Zn_4Sb_3}$ or $\mathrm{Zn_{6-\delta}Sb_5}$. Its Composition, Structure, Stability, and Polymorphs. Structure and Stability of $\mathrm{Zn_{1-\delta}Sb}$. *Chem. Mater.* **16**, 1580–1589 (2004).

[161] Basinski, Z. S., Hume-Rothery, W. & Sutton, A. L. The lattice expansion of iron. *Proc. R. Soc. A* **229**, 459–467 (1954).

[162] SingleCrystal™. URL `www.crystalmaker.com`. CrystalMaker Software Ltd, Oxford, England.

[163] Momma, K. & Izumi, F. *VESTA3* for three-dimensional visualization of crystal, volumetric and morphology data. *Journal of Applied Crystallography* **44**, 1272–1276 (2011).

[164] $FeSb_2$ Crystal Structure Datasheet. URL `https://materials.springer.com/isp/crystallographic/docs/sd_1008518`. Springer-Verlag Berlin Heidelberg & Material Phases Data System (MPDS), Switzerland & National Institute for Materials Science (NIMS), Japan.

[165] Pristas, G., Gabani, S., Flachbart, K., Filipov, V. & Shitsevalova, N. Investigation of the Energy Gap in $Sm_{1-x}B_6$ and $Sm_{1-x}La_xB_6$ Kondo Insulators. *Proc. Int. Conf. Strongly Correl. Electron Syst.* **3**, 012021 (2014).

[166] Blundell, S. *Magnetism in Condensed Matter* (Oxford Univ. Press, Oxford, UK, 2001).

[167] Lazarević, N. *et al.* Lattice dynamics of $FeSb_2$. *J. Phys. Condens. Matter* **24**, 255402 (2012).

[168] Hatnean, M. C., Lees, M. R., Paul, D. M. & Balakrishnan, G. Large, high quality single-crystals of the new Topological Kondo Insulator, SmB_6. *Sci. Rep.* **3**, 3071 (2013).

[169] Hsu, Y.-. T. *Unconventional Fermi surface in insulating SmB_6 and superconducting $YBa_2Cu_3O_{6+x}$ probed by high magnetic fields*. Ph.D. Thesis, University of Cambridge (2018).

[170] Sebastian, S. E. *Bose-Einstein Condensation in Spin Dimer Compounds*. Ph.D. Thesis, Stanford University (2006).

[171] Liu, H. *High magnetic field quantum oscillation study of Fermi surfaces in bulk unconventional insulators*. Ph.D. Thesis, University of Cambridge (2021).

[172] Hook, J. R. & Hall, H. E. *Solid State Physics*, vol. 2 (John Wiley & Sons Inc., Oxford, UK, 1991).

[173] Kleinman, D. A. & Schawlow, A. L. Corbino Disk. *Journal of Applied Physics* **31**, 2176–2187 (1960).

[174] Eo, Y. S. and Sun, K. and Kurdak, Ç. and Kim, D.-J. and Fisk, Z. Inverted Resistance Measurements as a Method for Characterizing the Bulk and Surface Conductivities of Three-Dimensional Topological Insulators. *Phys. Rev. Applied* **9**, 044006 (2018).

[175] Eo, Y. S. *et al.* Comprehensive surface magnetotransport study of SmB_6. *Phys. Rev. B* **101**, 155109 (2020).

[176] Cleveland, W. S. & Devlin, S. J. Locally weighted regression: An approach to regression analysis by local fitting. *J. Am. Stat. Assoc.* **83**, 596–610 (1988).

[177] Ran, S. *et al.* Extreme magnetic field-boosted superconductivity. *Nat. Phys.* **15**, 1250–1254 (2019).

[178] Knafo, W. *et al.* Comparison of two superconducting phases induced by a magnetic field in UTe_2. *Commun. Phys.* **4**, 40 (2021).

[179] Sebastian, S. E. *et al.* Normal-state nodal electronic structure in underdoped high-Tc copper oxides. *Nature* **511**, 61–64 (2014).

[180] Koyama, T., Nakamura, H., Kohara, T. & Takahashi, Y. Magnetization Process of Narrow-Gap Semiconductor $FeSb_2$. *J. Phys. Soc. Jpn.* **79**, 093704 (2010).

[181] Petrovic, C. *et al.* Anisotropy and large magnetoresistance in the narrow-gap semiconductor (formula presented). *Phys. Rev. B* **67**, 155205 (2003).

[182] Gonçalves da Silva, C. E. T. Magnetc Susceptibility of $FeSb_2$: A Quasi-Magnetic Semiconductor. *Solid State Commun.* **33**, 63–68 (1980).

[183] Lukoyanov, A. V., Mazurenko, V. V., Anisimov, V. I., Sigrist, M. & Rice, T. M. The semiconductor-to-ferromagnetic-metal transition in $FeSb_2$. *Eur. Phys. J. B* **53**, 205–207 (2006).

[184] Grigera, S. A. *et al.* Disorder-Sensitive Phase Formation Linked to Metamagnetic Quantum Criticality. *Science* **306**, 1154 – 1157 (2004).

[185] Mazin, I. I., Koepernik, K., Johannes, M. D., González-Hernández, R. & Šmejkal, L. Prediction of unconventional magnetism in doped $FeSb_2$. *Proc. Natl. Acad. Sci. USA* **118**, e2108924118 (2021).

[186] Kincaid, J. & Cohen, E. Phase diagrams of liquid helium mixtures and metamagnets: Experiment and mean field theory. *Phys. Rep. C* **22**, 57–143 (1975).

[187] Julian, S. R., Teunissen, P. A. A. & Wiegers, S. A. J. Fermi surface of UPt_3 from 3 to 30 T: Field-induced quasiparticle band polarization and the metamagnetic transition. *Phys. Rev. B* **46**, 9821–9824 (1992).

[188] Mercure, J.-F. *et al.* Quantum Oscillations in the Anomalous Phase in $Sr_3Ru_2\mathbf{O}_7$. *Phys. Rev. Lett.* **103**, 176401 (2009).

[189] Mott, N. F. The Basis of the Electron Theory of Metals, with Special Reference to the Transition Metals. *Proc. Phys. Soc., London, Sect. A* **62**, 416–422 (1949).

[190] Anderson, P. W. Absence of Diffusion in Certain Random Lattices. *Phys. Rev.* **109**, 1492–1505 (1958).

[191] Fu, L., Kane, C. L. & Mele, E. J. Topological Insulators in Three Dimensions. *Phys. Rev. Lett.* **98**, 106803 (2007).

[192] Moore, J. E. & Balents, L. Topological invariants of time-reversal-invariant band structures. *Phys. Rev. B* **75**, 121306 (2007).

[193] Roy, R. Topological phases and the quantum spin hall effect in three dimensions. *Phys. Rev. B* **79**, 195322 (2009).

[194] Hsieh, D. *et al.* A topological Dirac insulator in a quantum spin Hall phase. *Nature* **452**, 970–974 (2008).

[195] Bansil, A., Lin, H. & Das, T. Colloquium: Topological band theory. *Rev. Mod. Phys.* **88**, 021004 (2016).

[196] Hlawenka, P. *et al.* Samarium hexaboride is a trivial surface conductor. *Nat. Comms.* **9**, 517 (2018).

[197] SmB_6 Crystal Structure Datasheet. URL `https://materials.springer.com/isp/crystallographic/docs/sd_0527720`. Springer-Verlag Berlin Heidelberg & Material Phases Data System (MPDS), Switzerland & National Institute for Materials Science (NIMS), Japan.

[198] Chikina, A. *et al.* Correlated electronic structure of colossal thermopower $FeSb_2$: An ARPES and ab initio study. *Phys. Rev. Research* **2**, 023190 (2020).

[199] Kim, D. J., Xia, J. & Fisk, Z. Topological surface state in the Kondo insulator samarium hexaboride. *Nature Mater.* **13**, 466–470 (2014).

[200] Ren, Z., Taskin, A. A., Sasaki, S., Segawa, K. & Ando, Y. Large bulk resistivity and surface quantum oscillations in the topological insulator Bi_2Te_2Se. *Phys. Rev. B* **82**, 241306 (2010).

[201] Kushwaha, S. K. *et al.* Sn-doped $Bi_{1.1}Sb_{0.9}Te_2S$ bulk crystal topological insulator with excellent properties. *Nat. Commun.* **7**, 11456 (2016).

[202] Chen, F. *et al.* Magnetoresistance evidence of a surface state and a field-dependent insulating state in the Kondo insulator SmB_6. *Phys. Rev. B* **91**, 205133 (2015).

[203] Ali, M. N. *et al.* Butterfly magnetoresistance, quasi-2D Dirac Fermi surface and topological phase transition in ZrSiS. *Sci. Adv.* **2**, 12 (2016).

[204] Yue, Z. *et al.* Crossover of Magnetoresistance from Fourfold to Twofold Symmetry in SmB_6 Single Crystal, a Topological Kondo Insulator. *J. Phys. Soc. Jpn.* **84**, 044717 (2015).

[205] Couderc, R., Amara, M. & Lemiti, M. Reassessment of the intrinsic carrier density temperature dependence in crystalline silicon. *Journal of Applied Physics* **115**, 093705 (2014).

[206] Hrostowski, H. J., Morin, F. J., Geballe, T. H. & Wheatley, G. H. Hall Effect and Conductivity of InSb. *Phys. Rev.* **100**, 1672–1676 (1955).

[207] Thim, H. Temperature effects in bulk GaAs amplifiers. *IEEE Transactions on Electron Devices* **14**, 59–62 (1967).

[208] Kasuya, T. *et al.* Mechanisms for anomalous properties in SmB_6. *Journal of Magnetism and Magnetic Materials* **31-34**, 447–450 (1983).

[209] Roman, J. *et al.* Transport and magnetic properties of mixed valent SmB_6. *Physica B: Condensed Matter* **230-232**, 715–717 (1997).

[210] Wolgast, S. *et al.* Magnetotransport measurements of the surface states of samarium hexaboride using Corbino structures. *Phys. Rev. B* **92**, 115110 (2015).

[211] Syers, P., Kim, D., Fuhrer, M. S. & Paglione, J. Tuning Bulk and Surface Conduction in the Proposed Topological Kondo Insulator SmB_6. *Phys. Rev. Lett.* **114**, 096601 (2015).

[212] Eo, Y. S. *et al.* Transport gap in SmB_6 protected against disorder. *Proc. Natl. Acad. Sci. USA* **116**, 12638–12641 (2019).

[213] Cooley, J. C., Aronson, M. C., Fisk, Z. & Canfield, P. C. SmB_6: Kondo Insulator or Exotic Metal? *Phys. Rev. Lett.* **74**, 1629–1632 (1995).

[214] Lee, S. *et al.* Observation of the Superconducting Proximity Effect in the Surface State of SmB_6 Thin Films. *Phys. Rev. X* **6**, 031031 (2016).

[215] Zhou, Y. *et al.* Hall-coefficient diagnostics of the surface state in pressurized $\mathrm{SmB_6}$. *Phys. Rev. B* **101**, 125116 (2020).

[216] Shirahama, K., Ito, S., Suto, H. & Kono, K. Surface study of liquid ^{3}He using surface state electrons. *Journal of Low Temperature Physics 1995 101:3* **101**, 439–444 (1995).

[217] Harrell, R. *et al.* Very high quality 2DEGS formed without dopant in GaAs/AlGaAs heterostructures. *Journal of Crystal Growth* **201-202**, 159–162 (1999).

[218] Umansky, V. *et al.* MBE growth of ultra-low disorder 2DEG with mobility exceeding 35×106 cm^2/Vs. *Journal of Crystal Growth* **311**, 1658–1661 (2009).

[219] Bolotin, K. *et al.* Ultrahigh electron mobility in suspended graphene. *Solid State Communications* **146**, 351–355 (2008).

[220] Lu, T. M., Pan, W., Tsui, D. C., Lee, C.-H. & Liu, C. W. Fractional quantum Hall effect of two-dimensional electrons in high-mobility Si/SiGe field-effect transistors. *Phys. Rev. B* **85**, 121307 (2012).

[221] Yamaguchi, E. Electron subbands and transport properties in inversion layers of InAs and InP. *Phys. Rev. B* **32**, 5280–5288 (1985).

[222] Manfra, M. J. *et al.* Electron mobility exceeding 160000cm^2/Vs in AlGaN/GaN heterostructures grown by molecular-beam epitaxy. *App. Phys. Lett.* **85**, 5394–5396 (2004).

[223] Schmult, S. *et al.* Quantum transport in high mobility AlGaN/GaN 2DEGs and nanostructures. *Physica Status Solidi (b)* **243**, 1706–1712.

[224] Moetakef, P. *et al.* Quantum oscillations from a two-dimensional electron gas at a Mott/band insulator interface. *App. Phys. Lett.* **101**, 151604 (2012).

[225] Lu, F., Zhao, J., Weng, H., Fang, Z. & Dai, X. Correlated topological insulators with mixed valence. *Phys. Rev. Lett.* **110**, 096401 (2013).

[226] Phelan, W. A. *et al.* On the Chemistry and Physical Properties of Flux and Floating Zone Grown SmB_6 Single Crystals. *Sci. Rep.* **6**, 20860 (2016).

[227] Fuhrman, W. T. *et al.* Screened moments and extrinsic in-gap states in samarium hexaboride. *Nat. Commun.* **9**, 1539 (2018).

[228] Ohtsubo, Y. *et al.* Non-trivial surface states of samarium hexaboride at the (111) surface. *Nat. Commun.* **10**, 2298 (2019).

[229] Eo, Y. S. *et al.* Bulk transport paths through defects in floating zone and Al flux grown $\mathrm{SmB_6}$. *Phys. Rev. Materials* **5**, 055001 (2021).

[230] Ohm, G. S. *"Die galvanische Kette, mathematisch bearbeitet* (T. H. Riemann (in German), Berlin, Germany, 1827).

[231] Hsu, Y.-T. *et al.* Unconventional quantum vortex matter state hosts quantum oscillations in the underdoped high-temperature cuprate superconductors. *Proc. Natl. Acad. Sci. USA* **118**, (7) e2021216118 (2021).

[232] Smith, R. A. *Semiconductors*, vol. 2 (Cambridge University Press, Cambridge, UK, 1978).

[233] Kim, D. J., Grant, T. & Fisk, Z. Limit Cycle and Anomalous Capacitance in the Kondo Insulator $\mathrm{SmB_6}$. *Phys. Rev. Lett.* **109**, 096601 (2012).

[234] Stern, A., Efimkin, D. K., Galitski, V., Fisk, Z. & Xia, J. Radio Frequency Tunable Oscillator Device Based on a $\mathrm{SmB_6}$ Microcrystal. *Phys. Rev. Lett.* **116**, 166603 (2016).

[235] Casas, B., Stern, A., Efimkin, D. K., Fisk, Z. & Xia, J. Direct observation of surface-state thermal oscillations in $\mathrm{SmB_6}$ oscillators. *Phys. Rev. B* **97**, 035121 (2018).

[236] Stankiewicz, J., Blasco, J., Schlottmann, P., Hatnean, M. C. & Balakrishnan, G. Impedance Spectroscopy of $\mathrm{SmB_6}$ single crystals (2021). arXiv:2109.05313.

[237] Rybin, Y. K. *Electronic Devices for Analog Signal Processing* (Springer Publishing, New York, New York, USA, 2011).

[238] Gilmour, A. S. *Klystrons, Traveling Wave Tubes, Magnetrons, Crossed-field Amplifiers, and Gyrotrons* (Artech House, Norwood, Massachusetts, USA, 2011).

[239] Wagh, A. A., Kumar, P. S. A., Bhat, H. L. & Elizabeth, S. Negative differential resistance in $Gd_{0.5}Sr_{0.5}MnO_3$: A consequence of Joule heating. *Journal of Applied Physics* **108**, 063703 (2010).

[240] Alexandrov, A. S. *et al.* Current-controlled negative differential resistance due to Joule heating in TiO_2. *App. Phys. Lett.* **99**, 202104 (2011).

[241] Hall, R. P., Sherwin, M. & Zettl, A. Negative Differential Resistance and Instability in $NbSe_3$. *Phys. Rev. Lett.* **52**, 2293–2296 (1984).

[242] M. Nishida *et al.* Negative differential resistance in CDW nonlinear transport of quasi-one dimensional conductor $Per_2M(mnt)_2$ [M = Au, Pt] . *J. Phys. IV France* **131**, 129–130 (2005).

[243] Luican-Mayer, A. *et al.* Negative differential resistance observed on the charge density wave of a transition metal dichalcogenide. *Nanoscale* **11**, 22351–22358 (2019).

[244] Kim, D. J. & Fisk, Z. A Kondo insulating memristor. *App. Phys. Lett.* **101**, 013505 (2012).

[245] Hundley, M., Canfield, P., Thompson, J., Fisk, Z. & Lawrence, J. Evidence for a 'coherence' gap in $Ce_3Bi_4Pt_3$. *Physica B: Condensed Matter* **171**, 254–257 (1991).

[246] Boebinger, G., Passner, A., Canfield, P. & Fisk, Z. Studies of the Kondo insulator $Ce_3Bi_4Pt_3$ in 61 T pulsed magnetic fields. *Physica B: Condensed Matter* **211**, 227–229 (1995).

[247] Chua, L. Memristor – The missing circuit element. *IEEE Transactions on Circuit Theory* **18**, 507–519 (1971).

[248] Strukov, D. B., Snider, G. S., Stewart, D. R. & Williams, R. S. The missing memristor found. *Nature* **453**, 80–83 (2008).

[249] Peierls, R. Zur Theorie der galvanomagnetischen Effekte. *Zeitschrift für Physik* **53**, 255–266 (1929).

[250] Jones, H. & Zener, C. The theory of the change in resistance in a magnetic field. *Proc. R. Soc. Lond. A* **145**, 268–277 (1934).

[251] Chambers, R. G. The Kinetic Formulation of Conduction Problems. *Proc. Phys. Soc. A* **65**, 458–459 (1952).

[252] Pippard, A. B. *Magnetoresistance in metals*, vol. 2 (Cambridge University Press, Cambridge, UK, 1989).

[253] Sanchez-Castro, C. Negative magnetoresistance of $\mathrm{Ce_3Bi_4Pt_3}$ at low temperatures. *Phys. Rev. B* **49**, 4421–4424 (1994).

[254] de Launay, J., Dolecek, R. & Webber, R. Magnetoresistance of copper. *Journal of Physics and Chemistry of Solids* **11**, 37–42 (1959).

[255] Abrikosov, A. A. Quantum linear magnetoresistance. *EPL* **49**, 789–793 (2000).

[256] Abrikosov, A. A. *Fundamentals of the Theory of Metals* (Dover Publications, New York, USA, 2017).

[257] Shur, M. *GaAs Devices and Circuits* (Plenum Press, New York, New York, USA, 1987).

[258] Nakajima, Y., Syers, P., Wang, X., Wang, R. & Paglione, J. One-dimensional edge state transport in a topological Kondo insulator. *Nat. Phys.* **12**, 213–217 (2016).